

**STUDY OF SILICON PHOTOMULTIPLIERS IN THE
APPLICATION FOR COSMIC RAYS DETECTION**

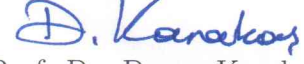
by

ALİ YILMAZ

THESIS SUBMITTED TO
THE GRADUATE SCHOOL OF NATURAL AND APPLIED SCIENCES
OF
THE ABANT İZZET BAYSAL UNIVERSITY
IN PARTIAL FULFILLMENT OF THE REQUIREMENTS FOR THE
DEGREE OF
DOCTOR OF PHILOSOPHY
IN
THE DEPARTMENT OF PHYSICS

JANUARY 2015

Approval of Doctor of Philosophy of Natural Sciences



Prof. Dr. Duran Karakaş

Director

I certify that this thesis satisfies all the requirements as a thesis for the degree of Doctor of Philosophy.



Prof. Dr. İbrahim Belenli

Head of Physics Department

This is to certify that we have read this thesis and that in our opinion it is fully adequate, in scope and quality as a thesis for the degree of Doctor of Philosophy.



Prof. Dr. Maurizio Iori

Co-Supervisor



Prof. Dr. Haluk Denizli

Supervisor

Examining Committee Members

1. Prof. Dr. Haluk DENİZLİ
2. Prof. Dr. İlhan TAPAN
3. Prof. Dr. Suat ÖZKORUCUKLU
4. Assoc. Prof. Dr. Cihan PARLAK
5. Assoc. Prof. Dr. Hakan YETİŞ



To My Family ...

ACKNOWLEDGEMENTS

This thesis would have not become possible without supports of many people. The first person I would like to thank is my advisor, Prof. Dr. Haluk Denizli. I have been working with him since the end of my bachelor. He has not only provided his knowledge and valuable guidance throughout all my scientific life, but also he becomes a brother for me.

I would like to express my gratitude to my co-supervisor, Prof. Dr. Maurizio Iori, for his endless guidance, expertise and wisdom in helping me to be a mature scientifically. I extend to my thanks and gratitude to my thesis defense referee committee, for their time and efforts in reviewing my thesis. I would also like to thank to Özlem Yelda Dilmen for proofreading of my thesis.

A special thanks is to Atılgan Altınkök for his friendship and helps. I would like to thank my friends, colleagues and teachers in physics department for their friendship and encouragement all trough my years at AIBU.

The PhD work is funded by the Scientific and Technical Research Council of Turkey (TUBITAK) in the framework of International Doctoral Research study, TUBITAK-BIDEB 2214 grant.

I would like to thank to INFN for developing read-out board, Trigger board. I am sincerely thankful to the Department of Physics, University of Rome "La Sapienza" for supporting the thesis.

I would also like to express my gratitude to the director of the International Foundation High Altitude Research Stations Jungfraujoeh and Gornergrat, Prof. Dr. Erwin Flückiger and Dr. Fabio Ferrarotto for his valuable help while developing the DAQ program.

Specially, I would like to thank Şeyma Atik for her understanding and supports provides me strength and willpower to finish my thesis.

ABSTRACT

STUDY OF SILICON PHOTOMULTIPLIERS IN THE APPLICATION FOR COSMIC RAYS DETECTION

Yılmaz, Ali

Doctor of Philosophy, Department of Physics

Supervisor: Prof. Dr. Haluk Denizli

Co-Supervisor: Prof. Dr. Maurizio Iori

January 2015, 118 pages

In this thesis, a study of prototypes based on a silicon photomultiplier (SiPM) coupled with scintillator detector in order to use on the applications of astroparticle physics is presented. One of the SiPM that is provided by SensL company is used at the terrace of Sphinx Observatory (Switzerland) for developing the prototype detector which will be used in TAU shower (TAUWER) array experiment. The other SiPM provided by FBK company is planned to use in camera system of Cherenkov Telescope Array (CTA). Theoretical and practical application of the detection method intended for using in the construction of a new high efficient TAUWER experiment in order to observe the *tau-neutrino* ν_τ is discussed in this thesis. An investigation of SiPM characterization was performed to determine the optimum conditions of a novel SiPM detector prototype. A series of measurement was established in a fast and reliable way with high precision in order to characterize SiPMs. Characterization tests such as gain, dark noise, optical crosstalk, afterpulsing measurements (dynamic) and forward IV measurement (static) are crucial for the operation of the SiPM. There is a big collaboration effort in INFN to improve the applications of SiPM produced by FBK. This SiPM

is used to develop a readout system for detecting the Cherenkov lights and will be assembled to the CTA camera system in the future. The prototype detector working at the terrace of Sphinx Observatory is also used to correlate the rate of the cosmic ray with solar weather parameters.

Keywords: cosmic rays, ground based detector, TAUWER, CTA, DRS4, silicon photomultipliers, astroparticle physics instrumentation

ÖZET

KOZMİK IŞINLARIN ALGILANMASININ UYGULAMASINDA SİLİKON FOTOÇOĞALTICILARIN ÇALIŞILMASI

Yılmaz, Ali

Doktora, Fizik Bölümü

Tez Danışmanı: Prof. Dr. Haluk Denizli

Ortak Tez Danışmanı: Prof. Dr. Maurizio Iori

Ocak 2015, 118 sayfa

Bu tezde, Astroparçacık fiziği uygulamalarında kullanılmak üzere, sintilasyon dedektörleri ile bir silikon fotoçoğaltıcı çiftine dayalı bir portatipin çalışması sunulmuştur. SenL şirketi tarafından sağlanan silikon fotoçoğaltıcılardan bir tanesi, *tau-shoWER* (TAUWER) deneyinde kullanılacak portatip dedektörü geliştirmek için Sphinx Gözlemevinin terasında kullanılmaktadır. FBK şirketinden sağlanan diğer silikon fotoçoğaltıcı *Cherenkov Telescope Array* CTA'nın kamera sisteminde kullanılması planlanmaktadır. Tau-nötrinosunu gözlemlemek için yeni bir yüksek verimli TAUWER deneyinin yapımında kullanılmak amacıyla, teorik ve pratik algılama yöntemi tasarlanmıştır ve bu tezde tartışılmıştır. Yeni bir SİFÇ'nin en uygun koşulların belirlenmesi için seri bir SİFÇ'in karakterizasyon araştırması gerçekleştirilmiştir. SİFÇ'in karakterizasyonları için hızlı ve güvenilir bir yolla yüksek hassasiyetli bir dizi ölçüm gerçekleştirilmiştir. Kazanç, karanlık gürültüsü, optiksel parazit, afterpulsing ölçümleri (dinamik) ve ileri I-V ölçümü (sitatik) gibi karakterizasyon testleri SİFÇ'lerin çalışması için çok önemlidir. Çerenkov ışıklarını tespit etme amacıyla bir okuma geliştirmede FBK şirketi tarafından sağlanan diğer bir SİFÇ kullanılmıştır ve bu ilerde CTA'nın

kamera sistemine monte edilebilir. Bu uygulama da yine Sphinx Gözlemevinin terasında yapılmış olup, solar mevsim parametrelerinin kozmik ışın oranlarıyla ilişkilendirmesinde kullanılmıştır.

Anahtar Kelimeler: kozmik ışınlar, karada konumlandırılmış dedektörler, TAUWER, CTA, DRS4, silikon fotoçoğaltıcılar, astroparçacık fizik aletleri

TABLE OF CONTENTS

ACKNOWLEDGEMENTS	iv
ABSTRACT	v
ÖZET	vii
1 INTRODUCTION TO SILICON PHOTOMULTIPLIERS (SIPMS)	1
1.1 Semiconductors	2
1.1.1 pin Photo-Diodes	4
1.1.2 Avalanche Photo-Diodes	6
1.1.3 Geiger-Mode Avalanche Photo-Diodes (G-APDs)	7
1.1.4 Silicon PhotoMultipliers	8
1.2 Properties of Silicon PhotoMultipliers	10
1.2.1 Gain	11
1.2.2 Dynamic Range	11
1.2.3 Thermal Noise	13
1.2.4 Dark Noise Rate	13
1.2.5 Afterpulsing	14
1.2.6 Optical Crosstalk	15
2 SIPM CHARACTERIZATION TESTS	17
2.1 The Amplifier Circuit	18
2.2 Forward I-V Measurement	22
2.3 Gain Measurement	24
2.4 Noise Measurements	24
2.4.1 PHE Separation	27

2.4.2	Crosstalk	28
2.4.3	Afterpulsing	32
2.5	Gain Dependence on Temperature	34
3	CHERENKOV LIGHT DETECTION FOR CTA PROTOTYPE CAM- ERA SYSTEM	39
3.1	Introduction	39
3.2	Theoretical Background	41
3.3	Description of Detector Setup	45
3.4	Estimation of the Number of Cherenkov Photons in Radiator . . .	53
4	COSMIC RAY DETECTION STUDIES AT SPHINX OBSERVATORY CENTER	57
4.1	Theoretical Background	57
4.2	Description of the Detector Prototype	58
4.3	Scintillators	59
4.3.1	Organic Scintillators	60
4.3.1.1	Energy Levels in Organic Scintillators	60
4.3.1.2	Scintillation Mechanism in Organic Scintillators	63
4.3.1.3	Plastic Scintillators	65
4.3.1.4	Inorganic Scintillators	66
4.4	Switched Capacitor Array Chip	67
4.4.1	The Domino Ring Sampler chip version 4	68
4.4.2	The Domino Wave Circuit	68
4.5	Verification Test of the Counter Box Heat Protection	70
4.6	DAQ & Event Selection Method	74
4.6.1	Least Square Method	79
4.7	Time of Flight (TOF) Method	82
4.8	Rise Time	84

4.8.1	Robustness of the Fit	85
4.9	Multiplicity of the Signal	86
4.10	phi Dependence Measurement	88
5	SOLAR ACTIVITY	92
5.1	Theoretical Background	92
5.2	Effect of Atmospheric Pressure	95
5.3	Correlation with Space Weather	101
6	SUMMARY AND CONCLUSION	105
A	CURRICULUM VITAE	116

LIST OF FIGURES

1.1	<i>Left</i> side of figure shows n-type semiconductor, in the <i>middle</i> , intrinsic semiconductors with intrinsic carrier density in the valance band is shown and at the <i>right</i> side, p-type semiconductors are shown. The doping process creates easily ionizable donors/acceptors near the conduction/valance band increasing the intrinsic conductivity [1].	4
1.2	Sketch of pin photodiode working in reverse bias and electric field, E distribution of the device.	5
1.3	Sketch of an electron avalanche in p-n junction photodiode. The electrons are shown in conduction band as black dots and the holes are shown as empty dots in the valance band. Due to electric field, the electrons get enough energy and they are accelerated that will cause to collide with the electrons in the valance band. This mechanism is also contribute to the avalanche. The created holes do not contribute to the reaction since they are more inert. This picture is redrawn from [2].	6
1.4	Basic layout of an SiPM. Many G-APDs and their quenching resistor R_q are connected in series and readout via a common load resistor R_c	9
1.5	Basic structure of an Geiger mode APD developed by Sadygov [8] (a) and (c) electric field distribution inside the junction [11]. . . .	10
1.6	The mean number of pixel fired and its variation as a function of mean number of photons per pixels [13].	12

1.7	Dark noise generation mechanisms in the device,. Left side is the thermally generation mechanism and right side is the self assisted generation of the free carriers where C_{band} represents the conduction band, V_{band} is the valance band, GR_{center} is the Geiger Region center and E_{gap} is the energy gap between the bands. This plot redrawn by [8].	14
1.8	Dark noise rate as a function of the threshold [8].	15
1.9	Sketch of optical crosstalk phenomenon. This plot is taken from [8].	16
2.1	SiPM readout circuits designed in Laboratory in the University of Rome by using LTSpice program. The electronic design scheme of PSA-5454+ amplifier chip is shown in (a), and The electronic design scheme of SiPM readout circuit is depicted in (b).	19
2.2	FBK SiPM readout circuits. Board 1 is on the left and Board 2 is on the right side of the figure.	20
2.3	Amplifications of the amplifiers installed on the readout boards. Yellow signal is input and purple is the output signals for both graphs.	20
2.4	Schematic view of the measurement setup.	22
2.5	Scheme of the $I-V$ measurement setup.	23
2.6	Forward I-V plot, shows the breakdown voltage is about 26.4 V shown in K1 parameter in the fit, measurement was done at 25 $^{\circ}C$ ambient temperature.	23
2.7	Estimated gain of the FBK-NUV 04 series of SiPM as a function of over voltage V_{ov} . The slope is the diode capacitance is around 17.7 pF.	24
2.8	A block diagram of the noise measurement setup.	26
2.9	Schematic view of the dark box and its picture.	26

2.10 (a) Typical scope trace of a SiPM: the signal corresponding to different number of cells, is well defined and self-triggered. The cell breakdown rate decreases from red to violet. The integration window is indicated between the arrow is around 12 ns, and green circle shows that the place where the afterpulses is expected. Figure (b) represents the integrated voltage for the p.e and figure c) shows that the integrated charge distribution for the p.e.	27
2.11 The distribution PHE of the first and second photoelectron for each temperature. D is defined as two photo peaks are in superposition.	28
2.12 Charge distribution of first and second phe, at fixed bias voltage (27.0 V) for -0.75 °C.	30
2.13 The response signal of the SiPM to a light burst, synchronized with the leading edge of the gate time(depicted between blue lines). Pulses in the dummy window (starting from the blue to pink line) may be since both random dark counts and afterpulses. The event shown here features as well an afterpulse occurring during the recovery time of the sensor.	30
2.14 Cross talk probability distribution as a function of operating voltage at different temperatures.	32
2.15 Dark noise rate of the FBK SiPM NUV04, working in dark condition at 22 °C room temperature, The integration time window of the led illuminated signal is around 20 ns.	33
2.16 The SiPM signal illuminated by led is integrated in the time window is shown at the left side and at the right side, the afterpulses are indicated.	33

2.17	Intrinsic gain calculation at $-14.6\text{ }^{\circ}\text{C}$. At the left side two Gaussian fits show the accumulation in the first two peaks in the photoelectron spectrum in terms of voltage (V). At the right side depicts that the accumulation in the first two peaks in the photoelectron spectrum in terms of integrated charge (Vs).	36
2.18	Intrinsic gain as function of temperature. At the left side the fit shows the distance in the first two peaks in a single photoelectron spectrum in terms of voltage (V). At the right side depicts that the distance in the first two peaks in a single photoelectron spectrum in terms of integrated charge (Vs).	37
2.19	Operating voltage as function of temperature. Its dependence on the temperature results from fit to be about $36\text{ mV}/^{\circ}\text{C}$	37
3.1	The telescope array (artist's impression), created by G.Pérez, IAC, SMM [21].	41
3.2	Sketch of air shower development is taken from Reference [22]. . .	42
3.3	Schematic representation of the Cherenkov light cone, produced by a primary γ ray from inside a cosmic ray source (e.g. a supernova remnant) that lightens an array of telescopes (a). Pictures of detected Cherenkov light on one camera (b), taken by [25].	43
3.4	Sketch of the charged particle releases a wavefront of Cherenkov light at an angle θ which is the angle of the Cherenkov cone. . . .	44
3.5	(a) The experimental Setup which includes 2 Kuraray scintillator boxes ($20 \times 20 \times 1.4\text{ cm}^3$ dimension) with readout by Hamamatsu 5783 PMTs, are separated by 96 cm apart each other and one plexiglass radiator box with an angle of 48° . (b) shows that its schematic view.	47

3.6	Simulation of the Cherenkov photons while a muon passing through the radiator medium.	47
3.7	(a) A close-up view of the radiator and the photon detector on their supports in the frame. The radiator has an angle around 48° with scintillator counter 1, (b) shows the simulation of the setup to produce Cherenkov photons inside the radiator.	48
3.8	The Cherenkov light produced by a muon (blue) going through the radiator, the red trace is representing muon passing through scintillator 1, and green for scintillator 2.	49
3.9	FBK SiPM thermal photoelectron separation distribution in the given integration time window.	50
3.10	Charge Distributions of the <i>muon signals</i> passing through scintillator 1 shown in (a) and scintillator 2 in (b). In the x axis, the peak, is around lower than 2000 pVs, corresponds to pedestal and noise signals in the region of interest window, the second peak, above 2000 pVs, corresponds to the signals.	50
3.11	The time of flight distribution of the muon signal passing through the scintillator 1 to scintillator 2.	51
3.12	Charge Distributions of the <i>Cherenkov signals</i> . In the x axis, every 26 pVs corresponds to 1 p.e. In Figure (a) the total charge integrated in full window (0-512 ns), which includes baseline plus signals coming out of the trigger window. The lower peak (in terms of absolute value) corresponds to the pedestal, the second peak corresponds to the signals. Figure (b) shows the total charge integrated in the gated window.	52
3.13	Charge Distributions of the <i>Cherenkov signals</i> the green peak shows that the charge integrated only the signals which are trigger region.	52

3.14 (a) Schematic view of FBK-NUV SiPM array setup, (b) Schematic view of the acceptance of FBK-NUV SiPM array setup.	55
4.1 Prototype detector installed at Sphinx (HFSJG) to test upward / downward particles separation, environmental effects.	58
4.2 Energy levels of organic molecules.	61
4.3 KURARAY organic scintillator $20 \times 20 \text{ cm}^2$ and 1.5 cm thick. . .	65
4.4 Emission spectrum of the KURARAY SCSN-61 scintillator [33]. .	65
4.5 Schematic drawing of DRS4 chip [35].	68
4.6 Simplified schematics of three out of 1024 double inverter blocks forming the domino wave circuit [28, 35].	69
4.7 Picture of the DRS4 Evaluation Board with different components.	70
4.8 Schematic view of the structure.	71
4.9 Produced power vs thickness of the shielding at different temperature differences.	72
4.10 Chill temperature variation in the summer period.	73
4.11 Internal variation of the temperature for each counter box in the summer period.	73
4.12 Data Acquisiton at Sphinx (HFSJG).	74
4.13 Temperature dependence as a function of time for Tile 1 (a) and Tile 2 (b) and adjusted operating voltage of the SiPMs in order to keep the gain constant for each board seen in (c) and (d), respectively.	75
4.14 Operating voltage dependence as a function of temperature for Tile 1 (a) and Tile 2 (b), respectively.	75
4.15 Determining the baseline of the SiPM signal.	77

4.16	Average baseline and their RMS distributions of the SiPM signals for phase 6 ₂ is shown in (a) is for Tile 1 and in (b) is for Tile 2, respectively. Figure (c), and (d) depicts that the RMS of the distribution of the baseline for Tile 1 and Tile 2. Average of the baseline versus its RMS value is seen in the Figure (c) and (d), their 2D plots are depicted in (e) and (f).	78
4.17	Peak distribution of the signals over sampling time window (a) is for Tile 1 and in (b) is for Tile 2, respectively.	79
4.18	Schematic view of a tower.	82
4.19	Time of flight (tof) calculation method used in this thesis. Tile separation is 160 cm. Magenta and blue lines indicate the fitted lines according to the method works forward direction from 20% until 70% of the amplitude.	83
4.20	Time of Flight distribution for phase6. Tile separation is 160 cm. The peak around +5 ns is due to the particle coming from atmosphere side (downward direction).	84
4.21	Signal shape of the rising time between the boundaries are 20% percent of the amplitude and 70% percent of the amplitude. . . .	85
4.22	Rising time distribution of the signal is between 20% and 70% percent of the amplitude. (a) is for Tile 1 and in (b) is for Tile 2, respectively.	85
4.23	Goodness of Fit distribution of the signal is between 20% and 70% percent of the amplitude. (a) is for Tile 1 and in (b) is for Tile 2, respectively.	86
4.24	Multiplicity of registered SiPM signal in a full sampling window. .	86

4.25	Integrated charge for all signal where the baseline was removed from each signal. (a) is for Tile 1 and in (b) is for Tile 2, respectively. The integrated charge for gated signals (c) is for Tile 1 and in (d) is for Tile 2, respectively.	87
4.26	Multiplicity events in terms of integrated charge for the full sampling window. (a) for Tile 1 and (b) for Tile 2, and (c) and (d) give the multiplicity in terms of the number of events.	88
4.27	Detector station located at Sphinx Observatory Center. The green arrow, is pointing to the valley, is about 14.5 <i>km</i> from the mountain.	89
4.28	Detector station is located at Sphinx Observatory Center. (a) The magenta arrow, is pointing to the Jungfrauoch mountain, is about 1.76 km from the detector. (b) Turquoise color arrow is pointing to the Monch mountain is about 0.76 km from the detector.	90
4.29	TOF distribution for phase 4 (a), and for phase 5 (b).	90
4.30	Rate distribution as a function of ϕ . (a) Red dagger represents the setup is pointing to the valley (14.5 km from the detector seen in Figure ??), blue dagger represents the setup is pointing to the Jungfrauoch-Monch direction (1.76 km from Jungfrauoch seen in Figure ??). The green gaussian fit shows that the TOF distribution exactly for vertical cosmic rays [39].	91
5.1	Bottom distribution is depicted for the relative Sunspot number. The middle distribution is for the annual average variation of the cosmic ray flux, and the top curve is cosmic ray flux from the neutron monitor in Climax [42].	93

5.2	(a) Percentage variation of cosmic ray flux (pink) in terms of hours where time gaps between two sequenced run, (b) variation of the pressure data (blue empty bars) taken by Meteoswiss weather station and variation of the cosmic ray flux (pink) in terms of each run period for measurements at Sphinx Observatory Center. . . .	97
5.3	Variation of solar parameters in the year of 2014. The highlighted regions are time periods selected for calculating barometric coefficient for the detector. Data was obtained from OMNI solar weather station [56], the data taking period in terms of hours is corresponding between 3763 to 4136 from the beginning of 2014. .	99
5.4	Dependence of rate on atmospheric pressure measured by the detector where the pressure data taken from Meteoswiss weather station [54].	100
5.5	Dependence of rate on atmospheric temperature measured by the detector.	101
5.6	Solar activities observed in the June of 2014. The percentage variation from the mean pressure corrected rate of cosmic ray (green) was measured by prototype detector working at Sphinx Observatory terrace. The variation of the mean of solar parameters such as interplanetary magnetic field (teal), solar proton density (red), solar plasma flow speed (blue) and plasma flow pressure (ocean) were taken from OMNI solar weather station [56], the data taking period in terms of hours is corresponding between 3763 to 4136 from the beginning of the year.	103
5.7	Typical Forbush decrease of the cosmic ray flux [61].	104

LIST OF TABLES

2.1	Amplifier specifications, used in the PCB board , taken by the data sheet [17].	18
2.2	Geometrical characteristics of SiPM.	21
4.1	Physical parameters of KURARAY SCSN-61 scintillator.	64

CHAPTER 1

INTRODUCTION TO SILICON PHOTOMULTIPLIERS (SIPMS)

This chapter describes Silicon PhotoMultipliers which are widely used in many fields; high energy physics, experimental particle physics, medical physics (Position emission tomography, computed tomography) as well as astroparticle physics, border protection and industry. In these fields, traditional Photomultiplier Tubes (PMTs) were most widely used as a photodetectors for a long time, but it is a common trend like in many field high technology replaces the old one with SiPM. Compared to the traditional one, SiPM is advantageous in that it has a higher quantum efficiency over a wide range of wavelength. It requires less energy to excite an electron from valance band to conduction band. On the other hand, traditional PMT generally requires more energy to eject an electron from cathode. The traditional PMTs require a magnetic shield to be operated properly while SiPMs are insensitive to the magnetic field. Since the SiPMs are very compact, they allow building miniaturized and high channel density detectors. These key features open more application fields to SiPMs where the traditional PMTs can not worked.

The thesis is organized in the following way;

- In chapter 1 an introduction to the silicon photomultipliers and information about semiconductor are given, then the properties of the Silicon photomultipliers are given briefly. Some potential noise sources of SiPMs are explained.
- Chapter 2 contains the characterization tests of the SiPM and gives a basic overview of how to analyze the collected data.

- In chapter 3 an application is developed for detection of Cherenkov light by a prototype SiPM system for implementing it to Cherenkov Telescope Array (CTA) camera system. The expected number of Cherenkov photons is also estimated.
- In chapter 4 the data acquisition system and time of flight method are described. Rise time measurement, multiplicity of the signal and phi dependence of the rate are given.
- In chapter 5 the solar activity studies and relation of the measured cosmic ray rate with solar weather parameters are presented.
- Chapter 6 includes the summary and conclusions of the detector prototype results and the future work.

1.1 Semiconductors

The best way to explain the semiconductors is the notion of energy bands for the possible state of the electrons in the semiconductors. The spacing between bands may not be occupied by the electrons which are creating a *forbidden zone*, while the energy bands themselves can be occupied. The highest energy band still filled completely at an absolute zero temperature is called the *valance band* and the band above is called as the *conductive band*. The energy difference between the lowest energy of the conductive band E_C and the highest energy of the valance and E_V is defined as the band gap E_g ; which defines the properties of the material with regards to conductivity [1]. The electrons bound in the valance band, may gain enough energy to cross over into the conduction band while the temperature increases. This does not generally happen in the materials with a large energy; $E_g > 3$ eV even at room temperature [2]. Hence the electrons in the valance band still bound to their individual nucleus, no free charge carriers are available

and this material is named as *insulator*. Contrary to the conduction band and the valance band overlap, means that conduction band is partially filled, many electrons are located in the conduction band. They are regarded as free charge carriers and the material is named as *conductor* [2]. A semiconductor lies in between these two cases such as silicon. An intrinsic conductivity is caused when a small fraction of electrons occupy the valance band and the band gap is smaller than for an insulator in contrast to conductors. Silicon has a band gap of 1.14 eV at room temperature. To excite an electron from valance band to conduction band, extra energy is required [1]. When an electron is excited to the conduction band a hole is left in the valance band which is called the negatively charged electron in the conduction band. A very important aspect of semiconductors is that can be doped and this process increases their intrinsic conductivity. In a pure crystalline silicon each atom of silicon shares 4 valance electrons with its neighbors in 4 covalent bands [2]. A new energy state can be created by replacing some of silicon atoms with phosphorus atoms, with 5 valance electrons one of which is nearly free. Figure 1.1 shows that the most of the electrons from donor placed at conduction band and leaving behind ionized donors at room temperature. This type of doping process is called as *n-type* semiconductor. *P-type* doping process in semiconductors that will have an extra energy state close to the valance band is created by replacing the silicon atoms with 3 valance electrons, then the acceptor levels capture an electron from conduction band and leaves a hole behind. These band diagrams; p-type, n-type and intrinsic are shown in Figure 1.1.

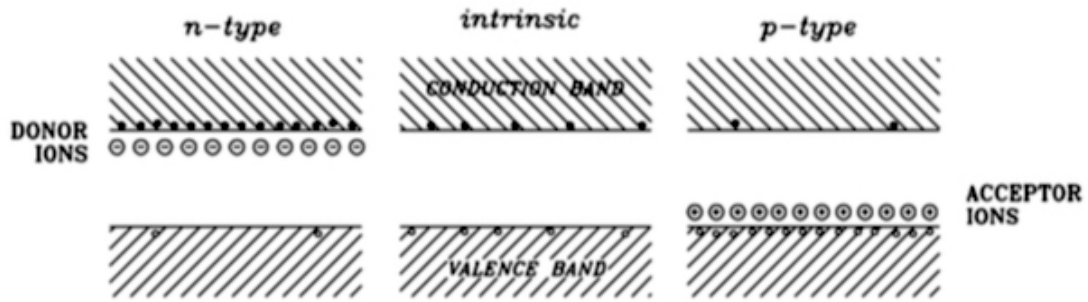


Figure 1.1: *Left* side of figure shows n-type semiconductor, in the *middle*, intrinsic semiconductors with intrinsic carrier density in the valence band is shown and at the *right* side, p-type semiconductors are shown. The doping process creates easily ionizable donors/acceptors near the conduction/valence band increasing the intrinsic conductivity [1].

1.1.1 *pin Photo-Diodes*

A p-n junction is made by contact between p- and n-doped regions in a semiconductor. The p-doped region contains more holes than electrons, and the n-doped region contains more electrons. This creates an electric field across the junction. When an external bias voltage is applied, the depletion region widens. An incident photon with energy greater than 1.2 eV can generate electron-hole (eh) pairs. These pairs are separated by the electric field: electrons drift toward the n⁺ region and holes toward the p⁺ region, creating a current. The current is proportional to the number of eh-pairs generated by the photon flux. The device in Figure 1.2 has high sensitivity because the intrinsic layer thickness can be designed from a few micrometers to several hundred micrometers, and the dark current is low due to the large potential barrier between the p and n sides. The device is efficient because charge carriers produced in the intrinsic layer have a long lifetime. The electric field in the device can rapidly remove the photons produced by charge carriers, and the separation of p-type and n-type layers by the intrinsic layer significantly reduces

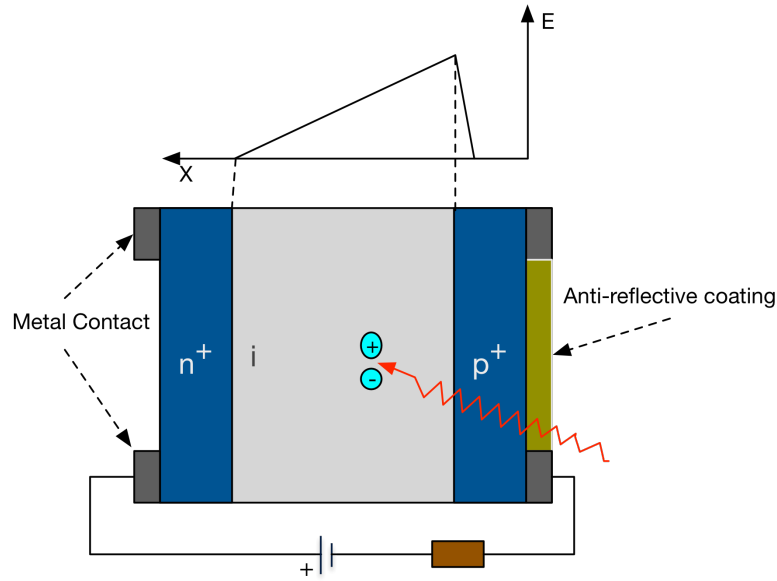


Figure 1.2: Sketch of pin photodiode working in reverse bias and electric field, E distribution of the device.

the capacitance of the device so that also decreases the RC time constant of the output signal which leads to the device has a very fast time response to a signal is generally in nanoseconds or sub-nanosecond range. The gain of this device is one since the pin photodiode does not have intrinsic signal amplification. For the reason that it is insensitive to detect a single photons. A pin photodiode, is affected by the essentially produced current in the highly doped regions that current is changing from few hundreds pico-ampere to one nano-ampere. Consequently the signal generated by the incoming photon flux should be greater than the intrinsic noise level of the device. As a result the pin photodiodes are not responsive enough to detect single photons. Besides the current signal produced by charged particles in the silicon cannot be distinguished from the photocurrent. Thus this device is not acceptable to used for reading-out a scintillators which is generally used to detect low intensity photon flux as in the experiments like Pierre Auger Observatory [3], The Cherenkov Telescope Array (CTA) [4].

1.1.2 Avalanche Photo-Diodes

The APD, "a photodiodes which has p-n junction, is operated above the breakdown voltage V_{break} and working at reverse bias voltage V_{bias} which extends the depletion layer. The working principle of APD is similar to the pin photodiode, incoming photon produces eh-pair by photoelectric effect. The created electron and the holes are then splitter by the electric field. Because of the high electric field in the APD, the electron and the hole gain sufficient energy to create new free electrons or holes from another bound electrons via the impact ionization process. In this way a single photon can trigger an avalanche that may be developed and produces an amplified current signal. Hence this internal signal amplification mechanism APD is suitable for using it to detect low intensity photon flux. Figure 1.3 is depicted that the avalanche process. When the electric

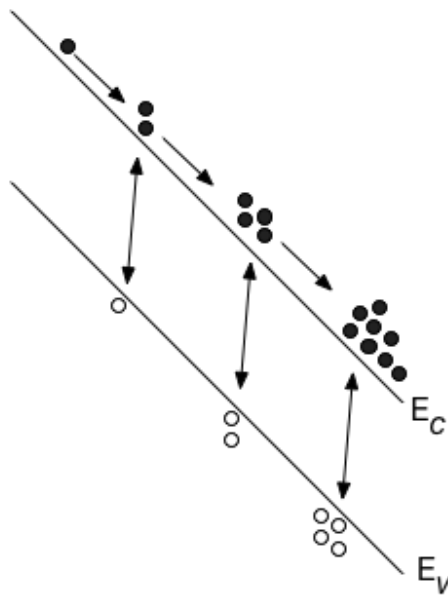


Figure 1.3: Sketch of an electron avalanche in p-n junction photodiode. The electrons are shown in conduction band as black dots and the holes are shown as empty dots in the valence band. Due to electric field, the electrons get enough energy and they are accelerated that will cause to collide with the electrons in the valence band. This mechanism is also contribute to the avalanche. The created holes do not contribute to the reaction since they are more inert. This picture is redrawn from [2].

field is increased in the APD, that will create secondary eh-pairs and the charge produced by the avalanche process will be proportional to the primary produced particle, is electron for silicon. At the end of that process, the signal produced by the APD is linearly dependent on the number of detected photons. The gain of an APD is generally less than 300 and fluctuates with the applied bias voltage and temperature. When the reverse bias voltage is applied at low level, no secondary eh-pairs is created, the device acts as a simple diode. The ionization rate for the electrons in silicon rise quickly while the holes stays negligible. The signal produced by the device is proportional to the detected light intensity. This phenomena is known as the linear mode of the APD which operates as a linear device similar to traditional PMT. The holes also create an eh-pair and start additional avalanche under the high voltage condition. So this results with the output signal is non-linear with regards to the detected light intensity. When the reverse bias voltage of an APD is increased the gain is also increased but the noise gets worse condition. The gain is strongly dependent on temperature and the operating voltage so that the operational condition needs to be carefully controlled and monitored. Operation mode of the APD alter from linear to Geiger-mode by increasing the applied bias voltage. The avalanche process of the device has to be quenched by a high-ohmic resistor which provides the signal with consistent amplitude. It is possible to detect a single photon since a single incoming photon can produce a signal of several millivolts on a 50Ω load. The gain G , of the G-APD is proportional to the amplitude of the signal, A , the capacitance C , the differences between the applied bias voltage and the breakdown voltage V_{break} , that can be summarized as $G \sim A \sim C \cdot (V_{bias} - V_{break})$.

1.1.3 Geiger-Mode Avalanche Photo-Diodes (G-APDs)

The Geiger-mode operation, is characterized by a bias voltage above the breakdown voltage of the APD. If the electric field in the device is strong enough that

charge carriers have impact ionization faster than to extract the charge carriers, the number of charge carrier increases exponentially with time because of the fact that the avalanche can be continued itself. G-APD gain is theoretically infinite, but in reality, the gain of G-APD persists a finite number, even though its gain is remarkably greater than a linear mode APD since the signal quenching. Without quenching the device will destroy due to the current generated in an avalanche. The current can be quenched by placing a resistor on one side of the G-APD. When the holes also contribute to the avalanche it is not easy to quench the current. Therefore the p-doped side of the device is formed to restrict the holes contribution to the avalanche. The time required to collect the charge in a pixel is about 30 ns [5] which makes the detector is sufficient to use it at high frequency operations. However, the drawbacks is that needs some time to recover the depletion region so that takes some time to process the information which may be longer than expected.

1.1.4 Silicon PhotoMultipliers

Silicon PhotoMultipliers (SiPMs) is a pixel detector that are formed an array of quadratic G-APD with their individual quenching resistors on parallel on a single wafer. They are biased above the breakdown voltage and working in Geiger mode. The analog information can be gathered considering the number of fired pixels while each pixel operates in digital mode. Figure 1.4 shows the basic layout of an SiPM. Studies on single photon detectors started and the first single photon detector was developed at the beginning of 1960 on the laboratories like Radio Corporation of America and Shockley [6, 7]. The single photon was observed even if it had very poor detection performance because of the limitation of silicon which did not have enough volume to keep depleted above the breakdown voltage for a long time to the diodes to be sensitive. Most of the prototype devices, the large internal majority of current in the depleted region

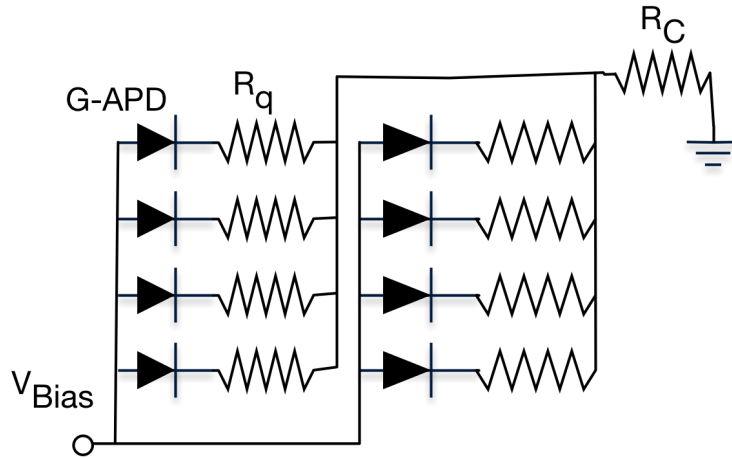


Figure 1.4: Basic layout of an SiPM. Many G-APDs and their quenching resistor R_q are connected in series and readout via a common load resistor R_C .

triggered an instant breakdown when the diode bias voltage came up just above the breakdown voltage [8]. Until 1990 no more significant development was seen on SiPM technology, but in 2000 the first Metal-Resistor-Semiconductor (MRS) APDs were discovered by a Russian team [9]. These devices were formed as a very thin metal layer and a layer of SiC (or Si_xO_y with high resistivity) restricts the Geiger breakdown because of a local reduction of electric field. This process leads to higher the multiplication value (of the order of 10^6) which can be achieved without controlling the breakdown, only increasing the bias voltage [10]. The next attempt was to divide MRS structure into many pixels and connect them all in parallel through an individual quenching resistor. In this way the first SiPM was created [11]. Figure 1.5 depicts that the basic SiPM structures and its typical electric field profile. In order to optimize the SiPM performance, different structures have been developed. The pixel dimensions are generally between 20 to $100 \mu\text{m}$ and includes around 500 - 4000 pixels/ mm^2 . The discharge is controlled with a polysilicon resistor are sunk into the silicon wafer so this leads to restrict the current flowing each pixel. The most important advantages of SiPMs

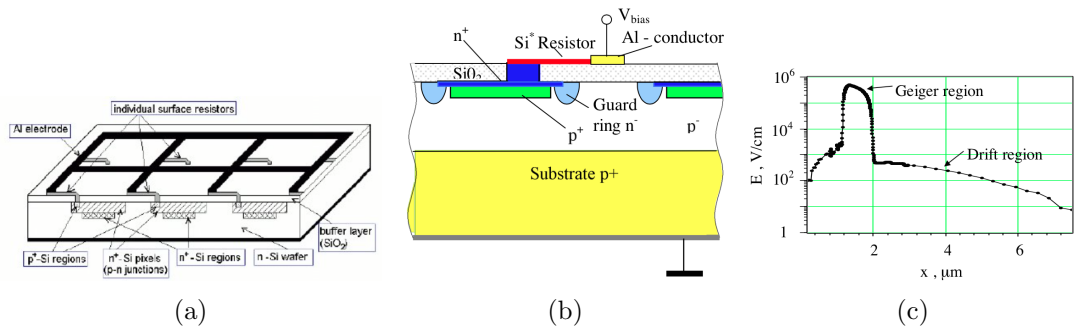


Figure 1.5: Basic structure of an Geiger mode APD developed by Sadygov [8] (a) and (c) electric field distribution inside the junction [11].

are summarized as follows:

- comparing with PMTs, the gain of SiPM is high enough, order of 10^6 , so that the amplification of the output signal may not require an amplification circuit or needs a very simple amplification circuit,
- they are insensitive to the magnetic field thus they do not need any magnetic shielding on the operations,
- require allow bias voltage to operate is around $\sim 30 - 70$ V,
- they have very small excess noise factor because of no fluctuations in the avalanche process, and
- they are sensitive to detect a single photoelectron.

The disadvantages of the devices are mainly a large (due to temperature dependence) dark current and a low radiation hardness.

1.2 Properties of Silicon PhotoMultipliers

In this section an overview of a typical SiPM properties are given.

1.2.1 Gain

SiPMs are characterized by the gain of the order of 10^6 , which can be produced when a photon detection in each pixels of the device are connected in parallel and they give the same amount of charges when it fires. When many pixels are fired at the same time, the output charge is called the gain G for a photon detection, which is equal to the sum of the single pulses. However:

$$G = \frac{Q_{out}}{e} = \frac{C_{pixel} \times (V_{bias} - V_{break})}{e} \cong \frac{C_{pixel} \times V_{ov}}{e} \quad (1.1)$$

where Q_{out} is the charge output of the pixel, e is the electron charge, C_{pixel} is the capacitance of the each pixel.

1.2.2 Dynamic Range

SiPMs are linear over a wide range of light fluxes. The device linearity is limited thanks to the the photons impinging on one pixel simultaneously. However the response of the SiPM is not linear anymore to the incoming photon flux which is generally related by an exponential function [11, 12];

$$\bar{N}_{firedpixel} = N_{tot} \cdot [1 - e^{-\lambda}] \quad \text{where} \quad \lambda = \frac{-N_{photon} \cdot PDE}{N_{tot}} \quad (1.2)$$

$$\sigma_{\bar{N}}^2 = N_{tot} \cdot e^{-\lambda} \cdot [1 - e^{-\lambda}] \quad (1.3)$$

where $\bar{N}_{firedpixel}$ is the number of fired pixel and $\sigma_{\bar{N}}^2$ is the variance of it, the total number of avalanche pixels in the device is given as N_{tot} , N_{photon} is the number of impinging photons, and PDE is the photon detection efficiency of the SiPM. The average number of detected photons can be represented by λ in the formula 1.2. This equation is valid under the assumption that the incom-

ing photons are homogeneously scattered over the SiPM surface and they have very short pulse time much shorter than the pixel recovery time. The detector noise which involves optical crosstalk and afterpulse effects are low enough to be neglected. Yet the optical crosstalk can be taken into account in the PDE measurements for a device with higher detector noise is shown in equation below;

$$PDE = \frac{PDE'}{1 - \kappa} \quad (1.4)$$

where κ is the crosstalk probability and equation 1.2 is rewritten as follows;

$$\bar{N}_{firedpixel} = N_{tot} \cdot [1 - e^{-\lambda}] + N_{photon} \cdot \frac{PDE'}{(1 - \kappa)} \cdot P_{afterpulse} \quad (1.5)$$

where $\lambda = N_{photon} \cdot \frac{PDE'}{N_{tot} \cdot (1 - \kappa)}$, and $P_{afterpulse}$ is the after pulse probability. Figure 1.6 depicts a SiPM response curve with photon resolving capability measured by Reference [11].

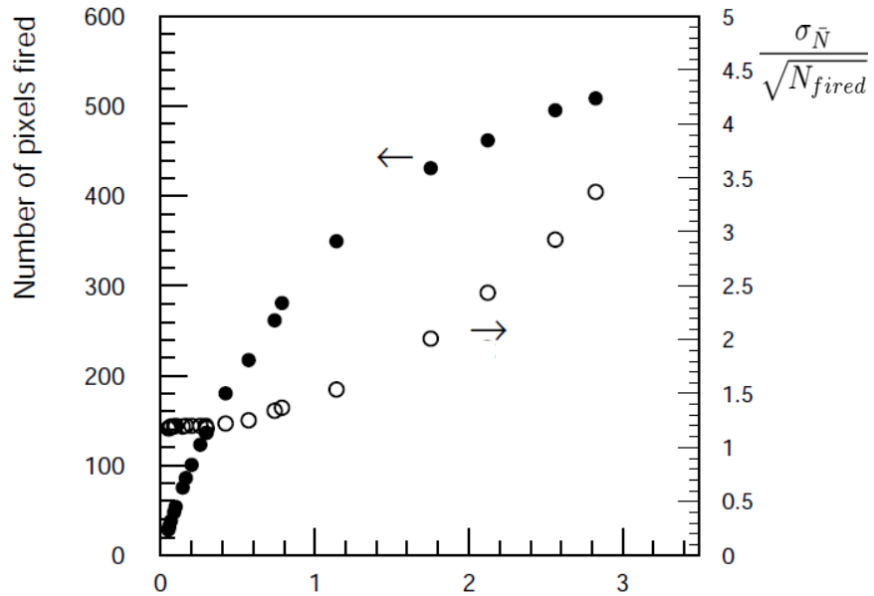


Figure 1.6: The mean number of pixel fired and its variation as a function of mean number of photons per pixels [13].

Hence the PDE' and $P_{afterpulse}$ depend on the bias voltage, the number of available pixels for the detection is effected by the change on the bias voltage. This influences the dynamic range of the device [11].

1.2.3 Thermal Noise

Electron-hole pairs are not only created by impinging a photon but also by thermal excitation. The signals are generated by photon impinging the avalanche can not be discriminated by one generated via thermally excited one, that process is called *thermal excitation*. In order to be more sensitive for the measurement of PDE, this effect should be taken into account and should be removed. For the reason that the dark measurements have to be done since the thermal noise is expected to be fluctuate with the temperature, all the measurements have to be done at the same temperature and same operating condition for the PDE measurements. At room temperature, a common noise rate of each pixels of a SiPM is around a few kHz. While a temperature fall about 8 °C, the noise rate is reduced to the number of pixels, the rate for a SiPM goes easily beyond a few MHz [8].

1.2.4 Dark Noise Rate

The dark noise, is one of the most important disadvantages of SiPMs, and restricts the sensitivity of the device to very low photon flux, refers to the unplanned Geiger-discharge of a SiPM without any photon impact even in operation in dark condition. There are two main processes controlling the dark noise in a SiPM which are also shown in Figure 1.7;

the first one is the eh-pairs generation in thermally as explained in the section 1.2.3 and the last one is the larger electric field inside the depletion region because of being a high electric field inside the depletion region, the free charge

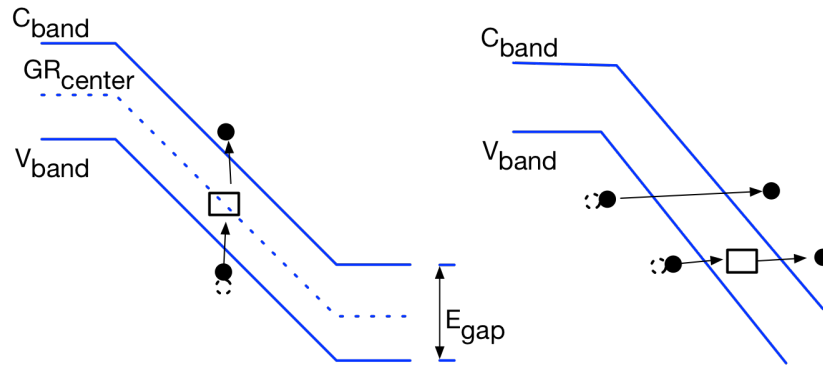


Figure 1.7: Dark noise generation mechanisms in the device,. Left side is the thermally generation mechanism and right side is the self assisted generation of the free carriers where C_{band} represents the conduction band, V_{band} is the valance band, GR_{center} is the Geiger Region center and E_{gap} is the energy gap between the bands. This plot redrawn by [8].

carriers have probabilities to penetrate trough the band gap and move from the valance band to the conduction band which process is also known as *tunneling effect* and it is dominant noise source when electric field is higher [2]. This process can be lowered by the electric field via reducing the bias voltage. The dark noise is also reduced via increasing the threshold voltage of the readout circuit that should be greater than the amplitude of the single photon signal. Figure 1.8 shows the effect of increasing the threshold values on the dark noise rate. While the threshold is equal to 4-photoelectrons, the dark noise is reduced around a few kHz which is operable condition for the measurements.

1.2.5 Afterpulsing

Another noise source is the *afterpulsing* of the pixel discharging. Because of being the impurities in the semiconductor creates an energy level that exist in the band gap. The free charge carriers can be captured by this energy level while avalanche occurring and released later in a certain time constant. If this time constant is longer than the avalanche time which will initiate an another avalanche. The

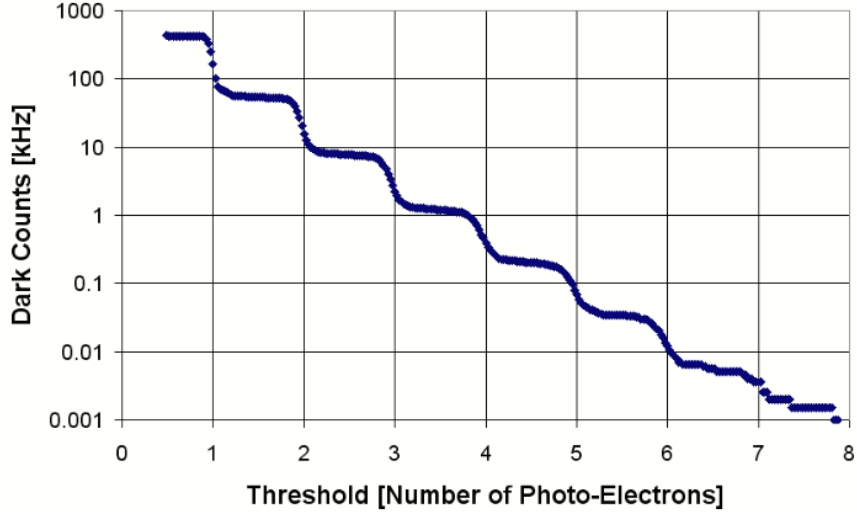


Figure 1.8: Dark noise rate as a function of the threshold [8].

amount of the additional charge caused by the secondary avalanche depends on the state of the diode when the after pulse is triggered. Afterpulse probability, P_{ap} as a function of time can be expressed as in the equation 1.6:

$$P_{ap}(t) = P_t \cdot \frac{e^{(-t/\tau_t)}}{\tau_t} \cdot P_{tr} \quad (1.6)$$

where P_t is the trap capture probability, τ_t is the trap lifetime and P_{tr} is the avalanche triggering probability. As a result, the afterpulsing probability can be increased with the square of the applied bias voltage because of the avalanche triggering probability and the trap capturing probability have been increased linearly with applied bias voltage [14].

1.2.6 Optical Crosstalk

Optical crosstalk is the other noise source correlated to the original pixel firing that occurs when a photon is released during the avalanche process. This process is indistinguishable from the original one. In order to reduce the optical

crosstalk probability is, manufacturing the pixels apart from each other, inserting reflective material trenches, and reducing the bias voltage that lower the triggering probability so that results with lowering the crosstalk effects. This crosstalk effect is sketchy shown in Figure 1.9. The optical crosstalk probability,

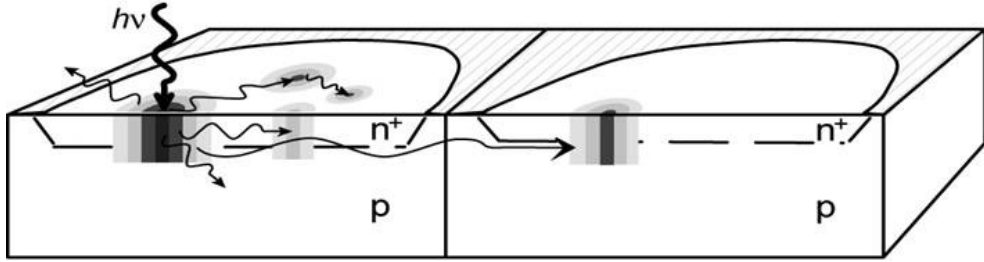


Figure 1.9: Sketch of optical crosstalk phenomenon. This plot is taken from [8].

X_{talk} is defined as the ratio of dark count rate of the first level of photoelectron ($DCR_{1.5}$) to the zeroth level photoelectron ($DCR_{0.5}$). This rates, are measured by thermally generated photons are not triggered by any light source. Hence the crosstalk is insensitive to the temperature at constant overvoltage (V_{ov}), is defined as the differences between bias voltage and breakdown voltage, reducing the temperature of the SiPM does not effect on the crosstalk probability.

CHAPTER 2

SIPM CHARACTERIZATION TESTS

The aim of this chapter is to give an introduction to the SiPM characterization measurements and to give a basic overview about collected data that how to be analyzed. The characterization test results of the SiPM give a direction or the selection option to the SiPMs are acceptable for a project. The correct measurement of the gain gives a reliable interpretation of the SiPM signal. In order to specify the best operational condition for a specific applications, it is important to understand the SiPM noise phenomena. Moreover, the current-voltage (IV) characteristic of a typical diode can be obtained. This chapter is going to deeply investigate the measuring techniques used in SiPM characterization. The SiPM produced by FBK-irst company [15] with the type number NUV-04-05 is used as an example for all characterization tests and Cherenkov light detection test is described in chapter 3. In addition, another SiPM is used in this thesis which is produced by SensL company [16] with the type number MicroFM-30035.

In all characterization tests, the SiPM is located inside a cooling box, which is completely in dark, allowing to take measurements over a some period of time under a stable and adjustable temperature. There are two main instruments which are used to collect the data from the SiPM. The first one is LeCroy WaveRunner oscilloscope with type number HRO 64Zi which digitizes and integrates the charge, originated by firing of one or more SiPM pixels and it also collects the traces of SiPM signal. The second instrument is Domino Ring Sampler board version 4 (DRS4), described in section 4.4.1, is also digitize the signal and record them to the PC for further analyze. The DAQ program for DRS4 was written by the author of this thesis and Fabio Ferraratto from University of Rome. Since the fast output of the SiPM is used, the width of the output pulse is expected to

be narrow and the amplitude of the signal is around 10 mV. This means that an amplification of the signal is needed, at least for low photon number events like in dark noise measurements which corresponds to the level of one photoelectron (p.e.). The information about the number of detected photons is contained in the integral of the signal. Hence, the readout of a SiPM includes a typical electronic readout with amplifier circuit, and it is triggered by a gate generator is generally a pulser with led driver for the measurements of dark noise rate measurement. The whole measurements are housed in a dark box to shield the setup from ambient light sources. Since the carried out SiPM signals are thermal that resulting with correlated noise. In the following section the characterization measurements start with determination of the amplification factor of the amplifier circuit for this thesis.

2.1 The Amplifier Circuit

The amplifier PCB board used in the SiPM readout electronics, was designed by L. Recchia, G Chiodi and M. Iori in University of Rome seen in Figure 2.1 and produced board depicted in Figure 2.2, is based on a commercial chip produced by MiniCircuits company [17] and the specifications are shown in Table 2.1.

Table 2.1: Amplifier specifications, used in the PCB board , taken by the data sheet [17].

Parameter	Condition (GHz)	Value
Frequency Range		(0.05 - 4.0) GHz
Operating Voltage		+5 V
DC current		(12 - 40) mV
Gain	2 GHz	13.6 dB
Noise Figure	2 GHz	1.1 dB

The readout board and amplifier circuit were designed based on the data sheets by using the LTSpice simulation program shown in 2.1. The board uses the

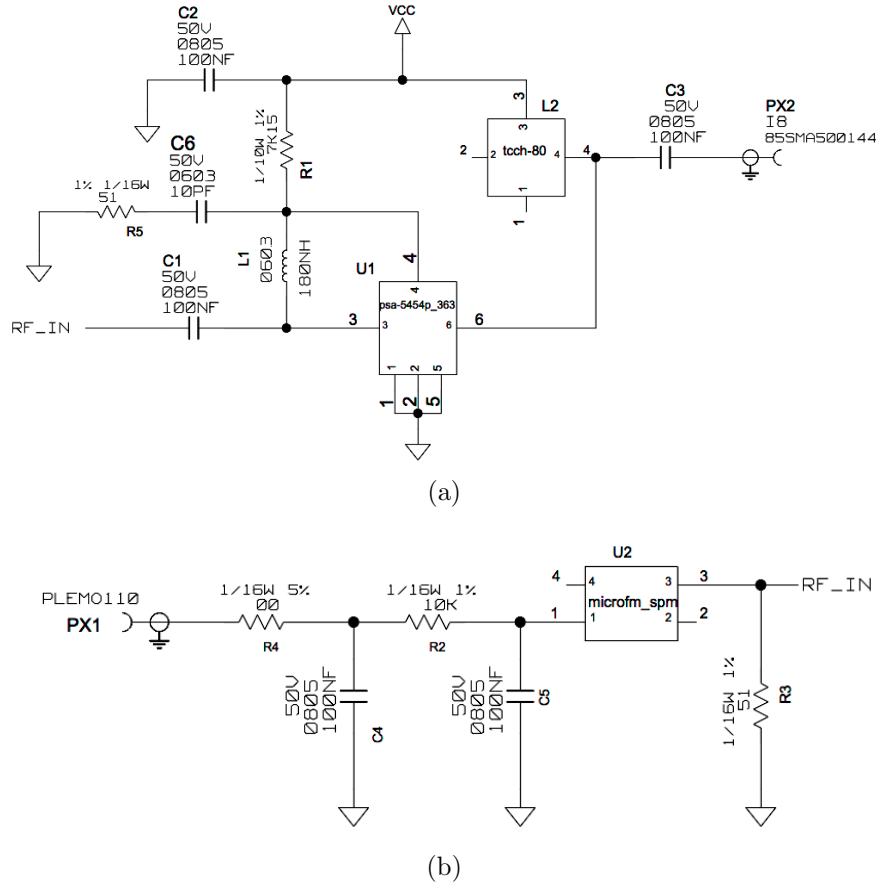


Figure 2.1: SiPM readout circuits designed in Laboratory in the University of Rome by using LTSpice program. The electronic design scheme of PSA-5454+ amplifier chip is shown in (a), and The electronic design scheme of SiPM readout circuit is depicted in (b).

PSA-5454+ chip model which needs +5 V power supply and it has a high dynamic range, advanced wide band support, and very noise level. The board is also directly adopted to 50Ω input and output impedance. The linearity of the boards was tested by sending pulses with known amplitude and plotting both input and output amplitudes for one of two PCB amplifier boards which are shown in Figure 2.2. The amplification factor which is also called gain is the extent to strength of the amplifier. The gain of the amplifiers was measured for each board using the signals shown in Figure 2.3. The input and output signal values of the board 1 are 31.2 mV and 190.3 mV, respectively. So the amplification factor is about 6.1. For the second board, these inputs and output values are 30.4 mV

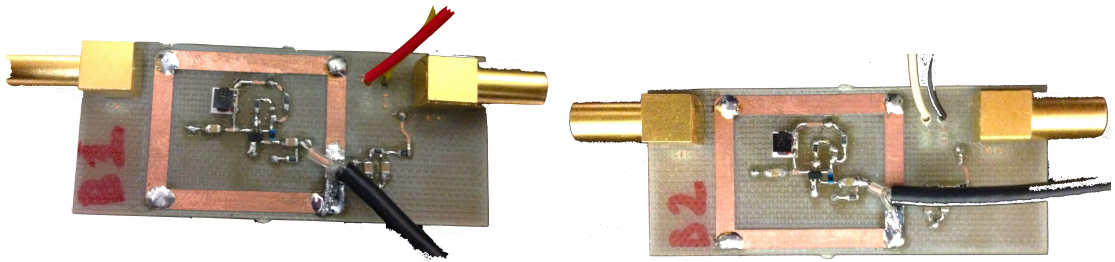


Figure 2.2: FBK SiPM readout circuits. Board 1 is on the left and Board 2 is on the right side of the figure.

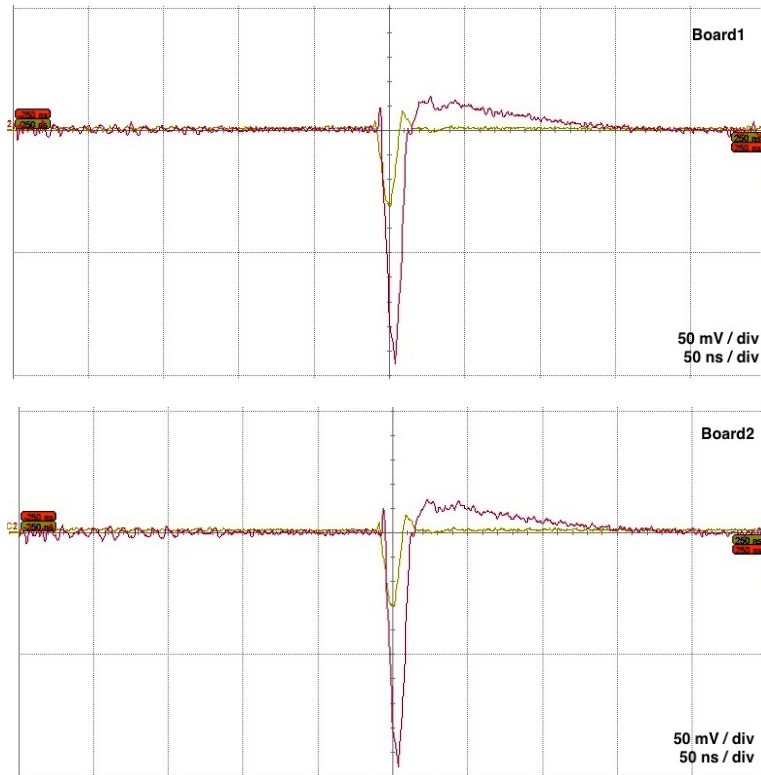


Figure 2.3: Amplifications of the amplifiers installed on the readout boards. Yellow signal is input and purple is the output signals for both graphs.

and 191.9 mV, respectively. The amplification factor is 6.3. The decibel (dB), which is a logarithmic unit, is commonly used to quantify the gain of an amplifier. These gain can be calculated in terms of decibel by using the equation 2.1.

$$\begin{aligned}
Gain &= 20 \times \log_{10} \left\{ \frac{V_{OUT}}{V_{IN}} \right\} \\
&= dB
\end{aligned}
\tag{2.1}$$

By using the equation 2.1 and the values given above, one can estimate the gain of the amplifiers on the board 1 and board 2, which are about 15.7 dB and 16.0 dB, respectively. In this section, FBK-NUV-04-05 SiPM are studied in terms of its operating principle and the characteristics that result from it. Since the data sheet has not been provided yet from the company, the geometrical characteristics of the FBK SiPM is only given in the Table 2.2. To perform this tests the SiPM device is installed on a board with a readout circuit and and ultra low noise 0.05 to 4 GHz Amplifier is shown in the Figure 2.2.

Table 2.2: Geometrical characteristics of SiPM.

Producer	Product ID	SiPM size (mm ²)
FBK	NUV-04-05	3×3

Before using the SiPMs in an application, one should know all characteristics like photon height equivalent (phe) separation, cross talk, afterpulsing, gain dependence on bias voltage which is actually a function of the temperature. In order to perform these characterization tests, dedicated experimental setup was developed. The setup includes a SiPM with amplifier board (shown in Figure 2.4), temperature sensor inside the cooler box, voltage regulator which is controlled by Arduino via 1-Wire and SPI communication on the computer. LeCroy HRO 64Zi oscilloscope has been used to perform the signal characterization and digitization.

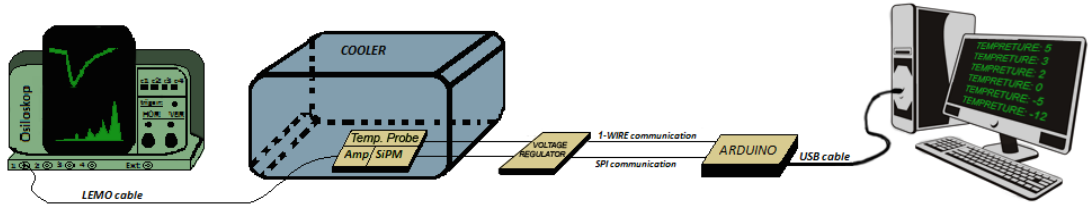


Figure 2.4: Schematic view of the measurement setup.

2.2 Forward I-V Measurement

The value of the breakdown voltage is crucial for the correlation of the noise rate between different temperatures. The typical concept behind the method is determination from the forward current-voltage ($I-V_{op}$) curve. In the p-n junction diode there is a small depletion region is formed even the absence of the bias voltage. This region behaves like a potential barrier that causes a voltage drop over the diode when it is biased in forward direction. While the biased voltage is greater than the voltage drop over the diode, which is acting as a conductive with a small resistance from the pixel, R_{pix} . This resistance is smaller than the quenching resistance, R_q . This quenching resistor can be determined by using the forward current which is assumed that is flowing through all the pixel connected in parallel in the SiPM. The forward $I-V$ curve can be report as

$$V_{op} - V_d = I \cdot R_s \quad (2.2)$$

where V_{op} is the operating voltage, V_d is the voltage drop over the diode, I is the measured current, and R_s is the series resistance connected to the diode. So the quenching resistance R_q can be written as

$$R_q = R_s \cdot N_{pixel} \quad (2.3)$$

where N_{pixel} is the total number of pixels in the SiPM.

The IV characterization measurements have been done in absolute darkness.

Figure 2.5 shows the dedicated electronic scheme setup to perform this characterization.

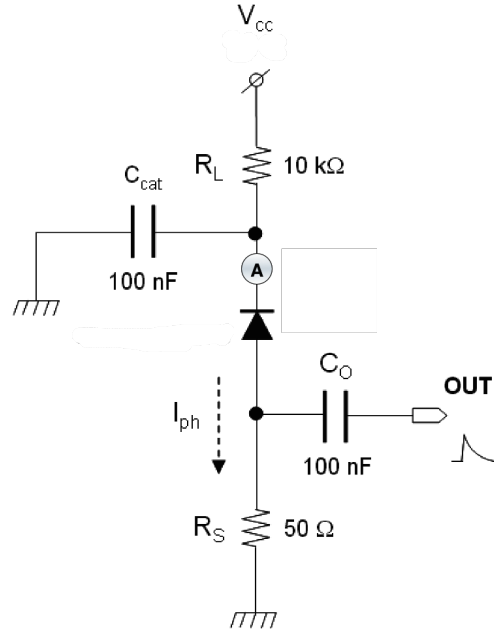


Figure 2.5: Scheme of the I - V measurement setup.

Forward I - V curve for the SiPM device is shown in the Figure 2.6. This figure clearly has two different behaviors. For the bias voltage below the 26.4 V is indicating the current that is equivalent to the diode resistance and growing exponentially over the breakdown voltage.

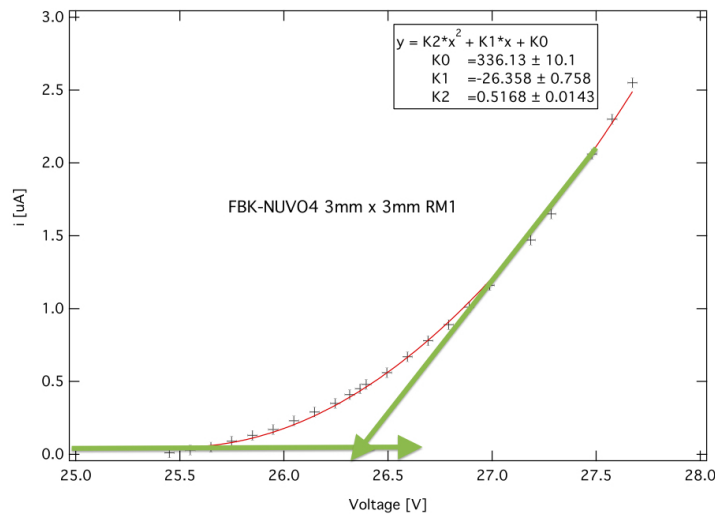


Figure 2.6: Forward I - V plot, shows the breakdown voltage is about 26.4 V shown in K1 parameter in the fit, measurement was done at 25 °C ambient temperature.

2.3 Gain Measurement

Gain is generally insensitive to temperature fluctuations because of the diode capacitance does not vary much with temperature (within a reasonable range of temperatures). Any gain shift with temperature has to be described to the breakdown voltage shift with temperature at a given bias voltage.

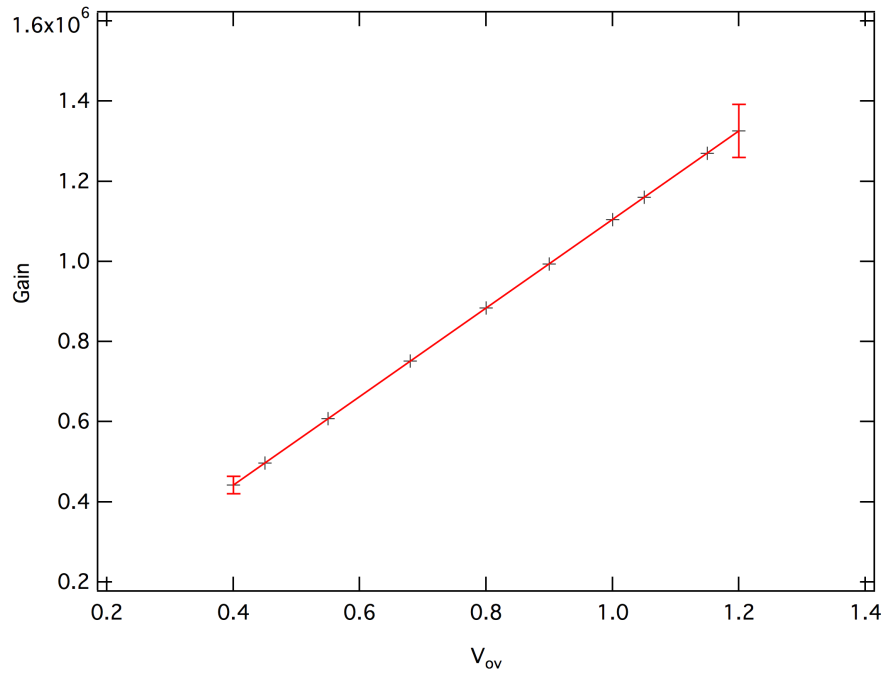


Figure 2.7: Estimated gain of the FBK-NUV 04 series of SiPM as a function of over voltage V_{ov} . The slope is the diode capacitance is around 17.7 pF.

Figure 2.7 depicts the estimated gain of the FBK-NUV 04 series of SiPM as a function of over voltage V_{ov} . The slope is the diode capacitance is around 17.7 pF.

2.4 Noise Measurements

Sometimes an electron is escaped from its atomic shell via thermal excitation. When this occurs in the charge carrier free zone, the electron may have possibility to create an avalanche that will make a signal, though there is no photon has passed through (shown in Figure 1.7). This phenomena is known as the noise of

the SiPM or generally dark noise and it is strongly depends on the applied bias voltage and temperature of device. The analysis of the noise phenomena is required no light trigger to the SiPM. The measurements are performed with FBK SiPM completely in darkness with the measured SiPM signals since thermally generated and resulting the noise. Figure 2.2 depicts that the SiPM is soldered to the readout circuit with amplifier circuit on a PCB board, and a DS18B20 temperature sensor is mounted near the setup to control the temperature profile, are located in the cooling box (or dark box) is seen Figure 2.9. The readout board PCB board connected to +5 V power source which delivers the operating voltage for the amplifier and another power source connected to the PCB to provide the bias voltage for the SiPM. The setup described above is common for all measurements. The fast output of the SiPM is connected to the LeCroy digital oscilloscope which digitizes and integrates the charge of the SiPM signal within the given time span is generally called integration gate represented with two black arrows in Figure 2.10 (a), and (b) show that its corresponding integrated charge histograms are recorded to the computer for further offline analysis. In order to measure the dark noise rate and afterpulsing probability, a pulse produced by the pulse generator is split into two branch, one is connected to the led driver (CAEN 5601), the other branch is connected to the DRS4 external trigger input, and the amplified signal output is attached to the one of the DRS4 input channel to digitize and record the raw data for the offline analysis. The block diagram of the measurement setup is shown in the Figure 2.8.

Controlling the temperature of the cooling box is manually done whereas the reading the temperature, controlling the constant bias voltage and recording the raw data for all type of measurements are controlled by a self-written appropriate programs. Both of these noise (dark rate and afterpulsing) measurements done in the section 2.5. Because of being it is crucial to keep the SiPM with a stable gain for changing temperature and bias voltage to stabilize the noise on a con-

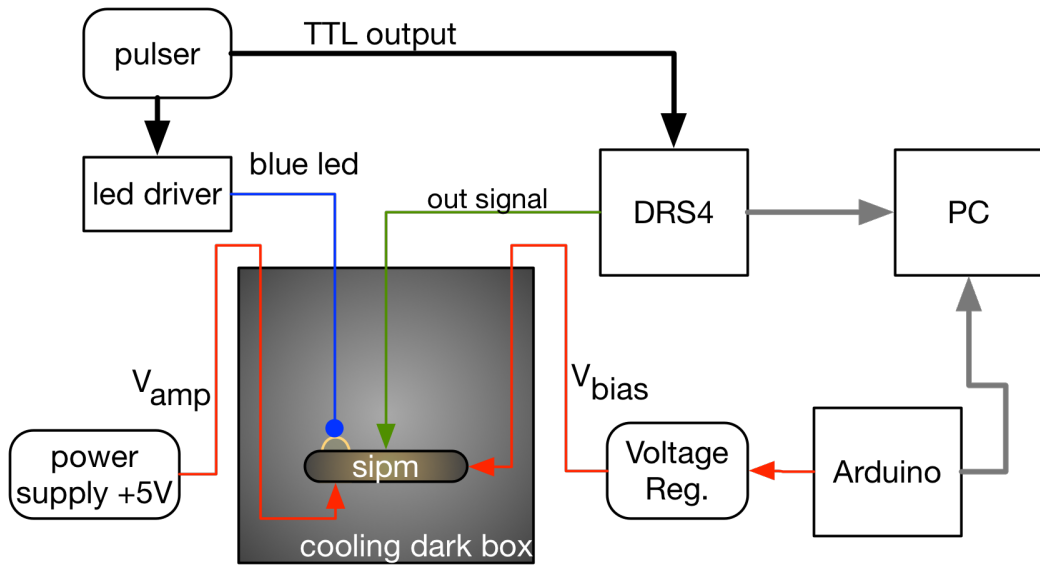


Figure 2.8: A block diagram of the noise measurement setup.

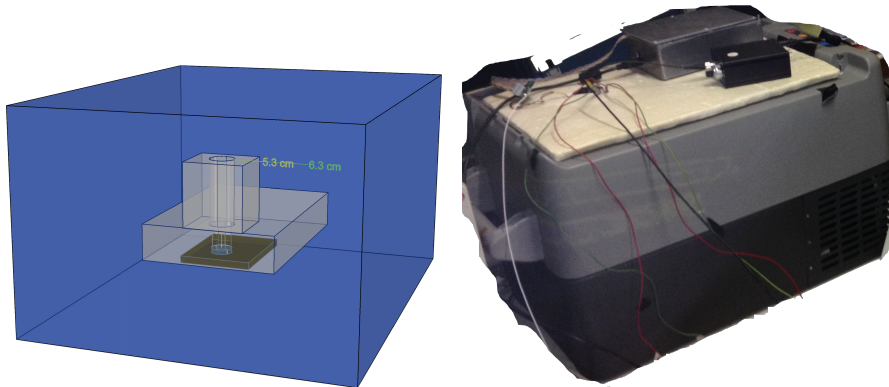
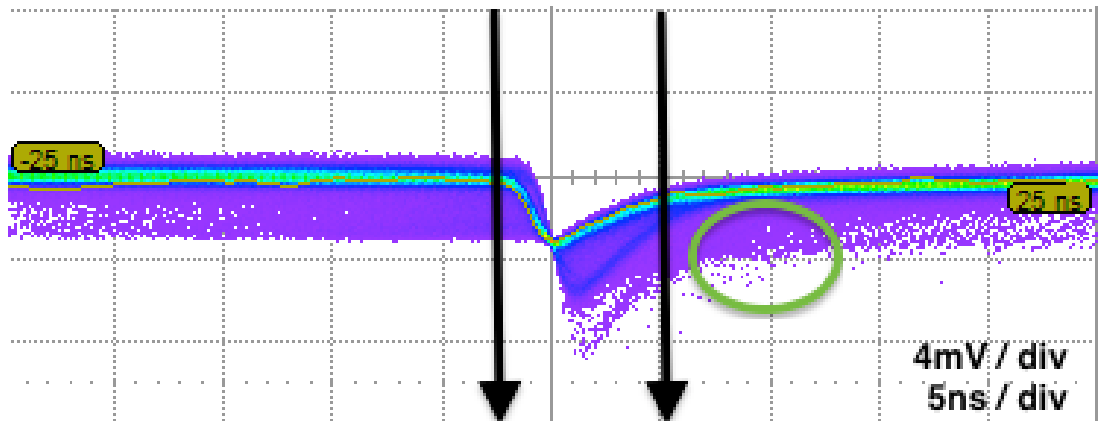


Figure 2.9: Schematic view of the dark box and its picture.

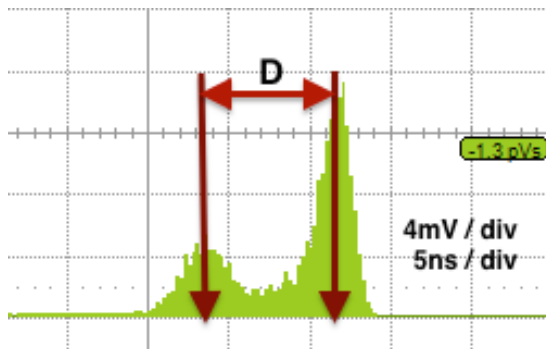
stant level. The precisely separation of the photons are affected by the optical crosstalk. In section 2.4.1, the measurement shows the phe separation capability of the system. The photon detection efficiency and the nonlinearity, which are also the characteristics of the SiPM, are not included in the scope of the thesis. This is mainly due to the lack of equipment to precisely measure the photon intensity of a light source, which is essential requirement of these measurements.

2.4.1 PHE Separation

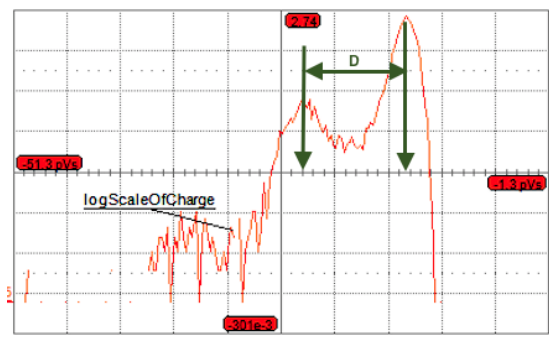
The pulse height separation is important to be able to discriminate the two photoelectron peak since the dark noise or gamma height equivalent signals have same amplitude. This will cause overlap of the two photoelectrons which results with poor resolution on the discrimination. Figure 2.10 (a) shows that the typical trace of the thermal photoelectrons. The first two photoelectrons are obviously seen and they are disturbed by dark noise (crosstalks and afterpulses) is seen as in violet color between the first two p.e in the time window is depicted with two black arrows.



(a)



(b)



(c)

Figure 2.10: (a) Typical scope trace of a SiPM: the signal corresponding to different number of cells, is well defined and self-triggered. The cell breakdown rate decreases from red to violet. The integration window is indicated between the arrow is around 12 ns, and green circle shows that the place where the afterpulses is expected. Figure (b) represents the integrated voltage for the p.e and figure c) shows that the integrated charge distribution for the p.e.

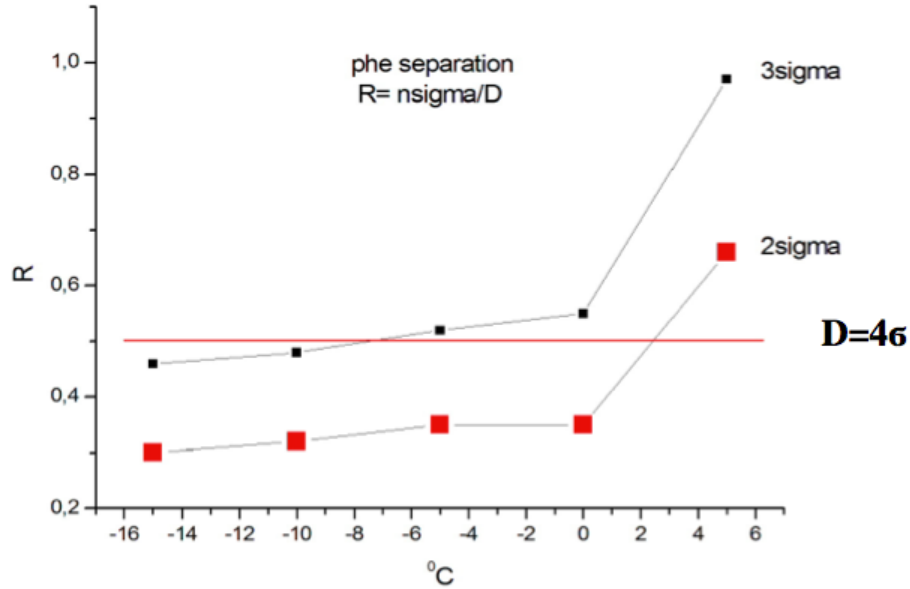


Figure 2.11: The distribution PHE of the first and second photoelectron for each temperature. D is defined as two photo peaks are in superposition.

As shown in Figure 2.11 the separation of photoelectrons is fairly good while working at a temperature below from the $0\text{ }^{\circ}\text{C}$ or close to $0\text{ }^{\circ}\text{C}$. That is important for experiment are dealing with the small number of photons like in Cherenkov experiments but it not so important for scintillating applications.

2.4.2 Crosstalk

A charge carrier in the depletion region of the SiPM will trigger an avalanche. This avalanche is mostly dependent on bias voltage. At higher bias voltage increase the electric field and accelerate the charge carriers so that increase the probability of the impact ionization. These process schematically shown in the Figure 1.5. While the avalanche process occurring in the SiPM, the recombination of the electron hole pairs around the depletion region that has a probability to produce a photon. These photon can travel and reach the neighbor cell diode so trigger a second avalanche. This quantity is named as optical crosstalk or X_{talk} which is shown schematically in Figure 1.9. One of the simplest method is to measure the dark noise (crosstalk, afterpulsing) is based on the measurements

done on the histograms. This can be done in the following;

- differences in the number of entry at the first and second photoelectron from total entry which gives the excess number of photons in the detection, shown in Figure 2.12.
- the total number of counts above the threshold divided by the total gate time means that the product of the number of counts and integration window width.

The schematic diagram of the experimental setup is shown in Figure 2.8. The pulser clock is synchronizing the light pulser illuminating the SiPM and the data acquisition, the signal pulse integration in a fixed time gate delayed with respect to the light pulse. The results given here were obtained with the following specific system:

- The coherent laser output with a poissonian statistics is an ultra-fast LED source (SP5601 - CAEN), is emitting ~ 5 ns long light pulses at 405 nm, with intensities in the 1-2000 photon range at room temperature ~ 22 °C and the light to be measured was delivered to the sensor by a white optical fiber.
- The signal digitization was synchronized to the laser pulse and integration gate generated with an AGILENT 33250A Waveform Generator, externally triggered by the laser,
- The signal was integrated by a LeCroy WaveRunner 64Zi oscilloscope (or DRS4 board that depends on the measurement); the signal was typically integrated over a 12 ns (or 20 ns for DRS4) long time window.

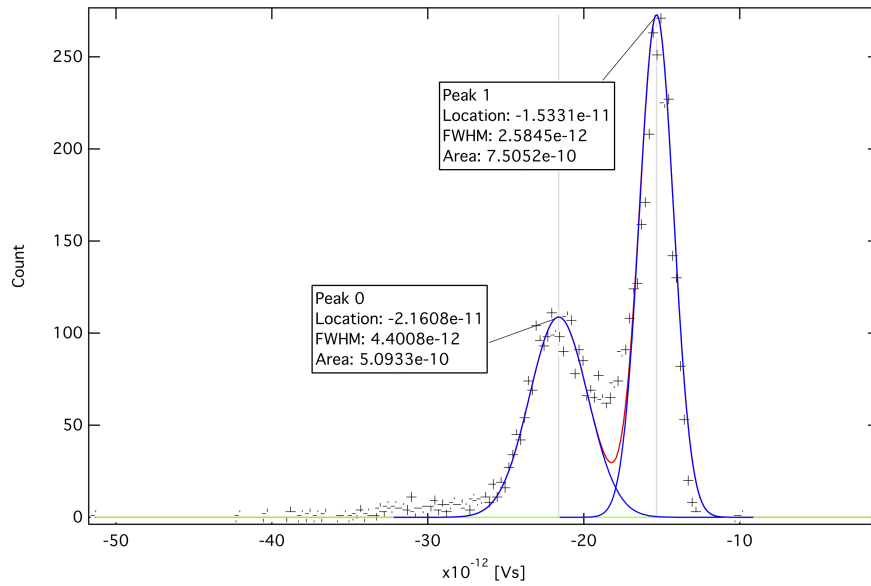


Figure 2.12: Charge distribution of first and second phe, at fixed bias voltage (27.0 V) for -0.75 °C.

Figure 2.13 depicts the response signal of the SiPM to a light burst, synchronized with the leading edge of the gate time. Pulses in the dummy window may be since both random dark counts and afterpulses. The event shown here features as well an afterpulse occurring during the recovery time of the sensor.

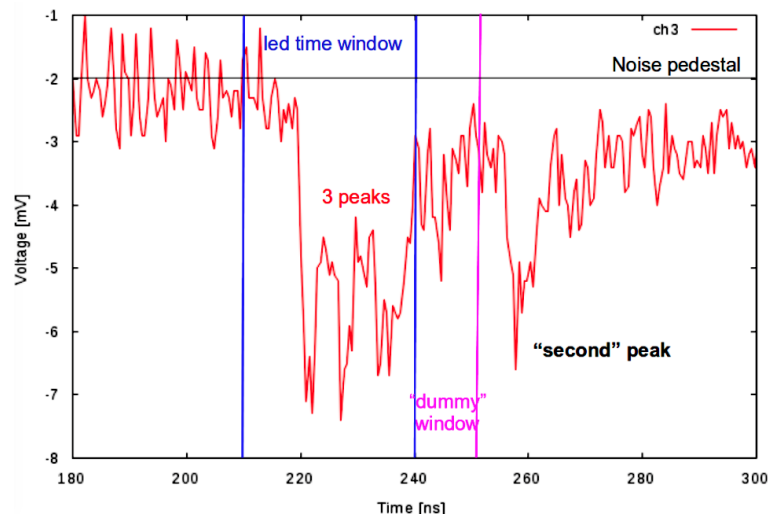


Figure 2.13: The response signal of the SiPM to a light burst, synchronized with the leading edge of the gate time(depicted between blue lines). Pulses in the dummy window (starting from the blue to pink line) may be since both random dark counts and afterpulses. The event shown here features as well an afterpulse occurring during the recovery time of the sensor.

All the data reported in this section come from the series of measurements:

- The measurements were performed for 3 temperatures from -6.7 to -0.75 °C and bias voltage distributed in the range of approximately 27 to 27.5 V (about 4 values). Increasing the number of measurements allowed to eliminate random errors to a great extent.
- The measurements were performed for a FBK-NUV04 model SiPM, usually at one temperature (22 °C) and one supply voltage (determined by the nominal value of V_{op} around 27 V). Some measurements were done at several voltages and several temperatures. The advantage of this series is that the dark count rate was measured using these two methods.

Figure 2.14 reports the dependence of the crosstalk probability (dark noise) on operating voltage for several temperatures. It is easy to observe that the dependence can be described by a linear function for reasonable values of voltage range. The deformation of the characteristics can be seen at higher voltages along with the operating voltage increase, more pulses in the integration time window begin to appear, which are not actual dark noise counts, but the afterpulses coming from the dark pulses which appeared earlier. The changes of dark noise rate with temperature are directly related to changes in the rate of thermal generation of carriers in the depletion layer. So that the crosstalk is heavily dependent to the operating voltage than the temperature change.

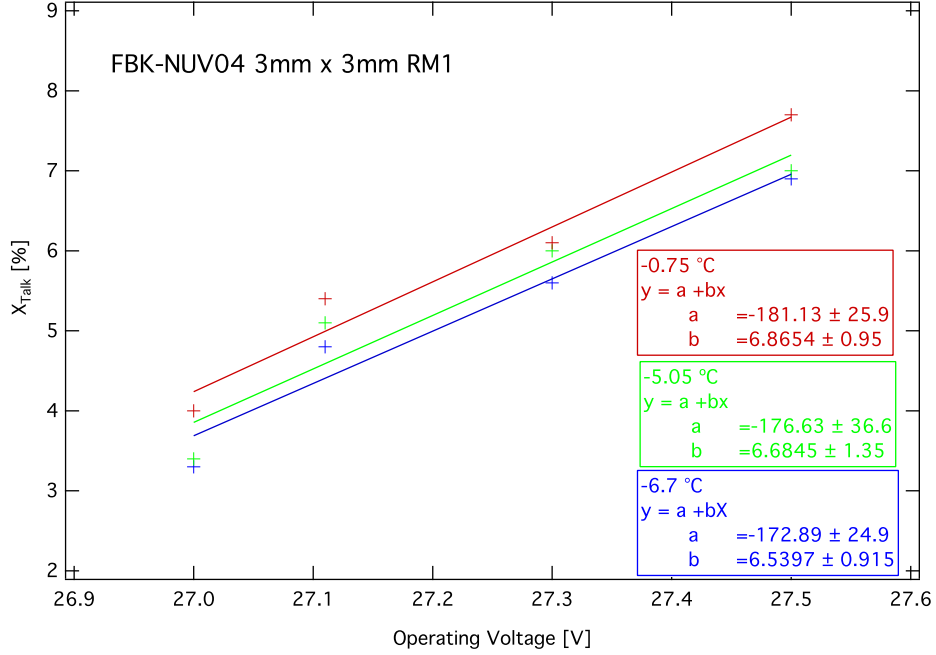


Figure 2.14: Cross talk probability distribution as a function of operating voltage at different temperatures.

This method described above, is based on the assumption that the probability that two uncorrelated avalanches are triggered within the same rise time is negligible, so that all the second photon events are due to crosstalk. The dark noise rate (includes both crosstalk and afterpulsing rates) is gathered by the fit on the time differences between the two photoelectron peak. This rate, is depicted in Figure 2.15, is around ~ 6 MHz.

2.4.3 Afterpulsing

Charge carriers around the avalanche region inside the SiPM can be trapped for a few nanoseconds, after their release may have probability to induce a cell breakdown and seen a delayed signal. Afterpulses can be seen as an excess of fired cells in a time window following the signal due to a light pulse (described in Figure 2.13), where the excess is computed. A statistical analysis of the excess, varying the gate length, is expected to lead to a measurement of the afterpulsing probability. Figure 2.15 shows the dark noise rate of the FBK SiPM

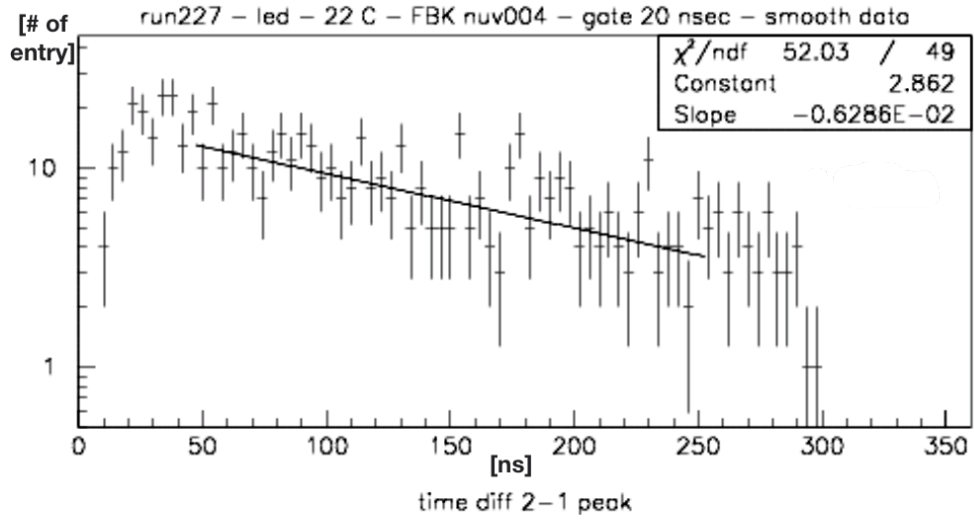


Figure 2.15: Dark noise rate of the FBK SiPM NUV04, working in dark condition at 22 °C room temperature, The integration time window of the led illuminated signal is around 20 ns.

NUV04, working in dark condition at 22 °C room temperature, the integration time window of the led illuminated signal is around 20 ns.

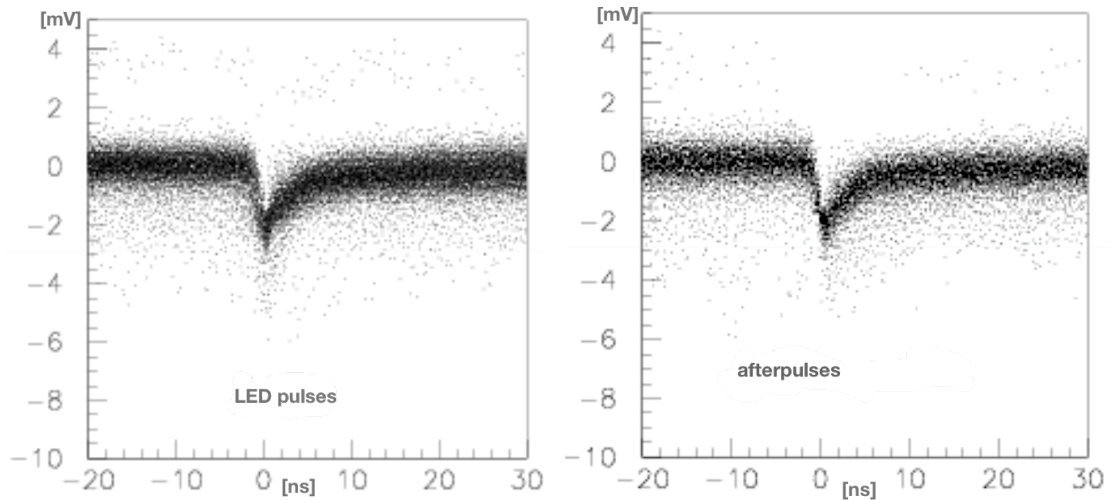


Figure 2.16: The SiPM signal illuminated by led is integrated in the time window is shown at the left side and at the right side, the afterpulses are indicated.

The SiPM signal illuminated by led is integrated in the time window is shown at the left side and at the right side, the afterpulses are indicated in Figure 2.16.

2.5 Gain Dependence on Temperature

It is important to understand how to operate the SiPMs in a steady way for particular applications. The challenge arising here is that the breakdown voltage V_{break} of the SiPM is determined by the temperature and is supposed to increase with the temperature [18]. Since the overvoltage V_{ov} is given by $(V_{bias} - V_{break})$, the overvoltage changes with the temperature as well, while the bias voltage V_{bias} is not adopted correspondingly. Because of the overvoltage is usually in the range of a few volts for the studied types and as many SiPM characteristics, e.g. the thermal noise rate, the gain, have a powerful dependence on the overvoltage, even small absolute differences in the overvoltage can lead to large comparable differences in SiPM performance and thus the overvoltage has to be retained stable in many applications. This can be achieved by keeping the temperature of the SiPM constant, but this may not be more suitable in many applications. For the reason that it is necessary to re-adjust the biasing voltage for compensating the differences in the breakdown voltage when the temperature is not stable for the operation of the SiPM. The aim of this section is to measure how the breakdown voltage changes with temperature and to test a method of self-adjusting of the bias voltage to keep the referenced gain constant. The breakdown voltage is supposed to be linearly dependent on the temperature [19] and can be written as

$$V_{break} = V_{T_0} \cdot [1 + \xi \cdot (T - T_0)] \quad (2.4)$$

where V_{T_0} is the breakdown voltage at a reference temperature $T_0 = 0 \text{ }^\circ\text{C}$ and ξ is the linear growth constant, the equation 2.5 can be rewritten as

$$V_{break} = V_{T_0} + \xi \cdot T \quad (2.5)$$

V_{T_0} is the breakdown voltage at 0 °C and ξ now exactly indicates the differences in the overvoltage with the temperature. The Celsius scale is selected for convenience reasons. The breakdown voltage of the SiPM can be measured over a wide temperature range by using the cooling box, and the progression factor ξ can then be determined from the data. Using a charge histogram of the LeCroy digital oscilloscope, the breakdown voltage of a desired temperature can be found by measuring the gain of the SiPM for a number of different bias voltages. Since the gain is proportional to the overvoltage (seen in equation (1.1)) the breakdown voltage can be determined by extrapolating the gain, as a function of the bias voltage, down to zero. The first attempt in the analysis is to determine the deposited charge per fired pixel $\Delta Q/pixel$ for a given overvoltage from the measured charge spectra. A general example of such a spectrum can be seen in figure 2.10. Offline plotting of the histogram and the fit have been done with the data analysis framework 'Igor Pro' [20] which is used throughout this thesis. Because of the charge measurement triggered with the internal threshold set to 0.5 p.e. signal level, the first peak in the spectrum corresponds to the amplified charge deposited in the histogram by one firing pixel plus an offset since the non-zero baseline of the SiPM signal and the internal pedestal current of the circuit. The second peak corresponds to two pixels firing during the gate and so on. The mean distance between two adjacent peaks Q_{i+1} and Q_i correlated with the deposited charge per fired pixel and the first two peaks are used to calculate this charge with the equation 2.6.

$$\frac{\Delta Q}{pixel} = Q_2 - Q_1 \quad (2.6)$$

where the individual peak position was determined by the fit of a Gaussian to the peaks.

The SiPMs used in this test are FBK NUV-04-05 series, 3×3 mm². The model

have been used to provide a fast output and a conventional output with longer rising time. In laboratory we have tested the gain versus the temperature as shown in Figure 2.18. The operating voltage versus the temperature function was evaluated changing the temperature and requiring the distance of first two peaks in the single photoelectron spectrum, shown in Figure 2.17, referring to the measurement made at 0 °C by adjusting the voltage. It results that, as shown in Figure 2.19, the data have a linear dependence with a slope of about 36 mV/°C including the amplifier gain.

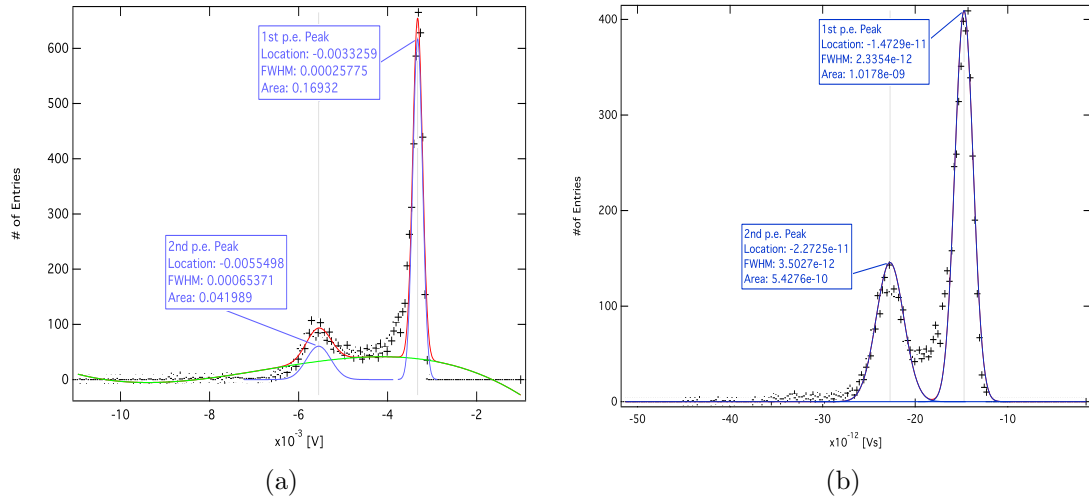


Figure 2.17: Intrinsic gain calculation at -14.6 °C. At the left side two Gaussian fits show the accumulation in the first two peaks in the photoelectron spectrum in terms of voltage (V). At the right side depicts that the accumulation in the first two peaks in the photoelectron spectrum in terms of integrated charge (Vs).

Figure 2.18 shows the intrinsic gain as a function of the temperature for FBK-NUV04 SiPM. A linear behavior over the all temperature range is observed and a fit with equation 2.5 results with the progression factor 36 mV/°C.

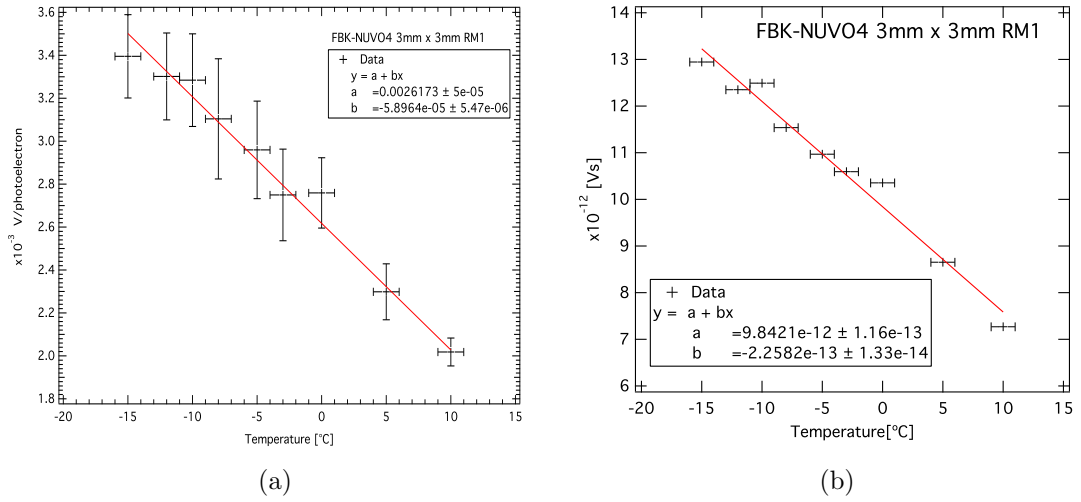


Figure 2.18: Intrinsic gain as function of temperature. At the left side the fit shows the distance in the first two peaks in a single photoelectron spectrum in terms of voltage (V). At the right side depicts that the distance in the first two peaks in a single photoelectron spectrum in terms of integrated charge (Vs).

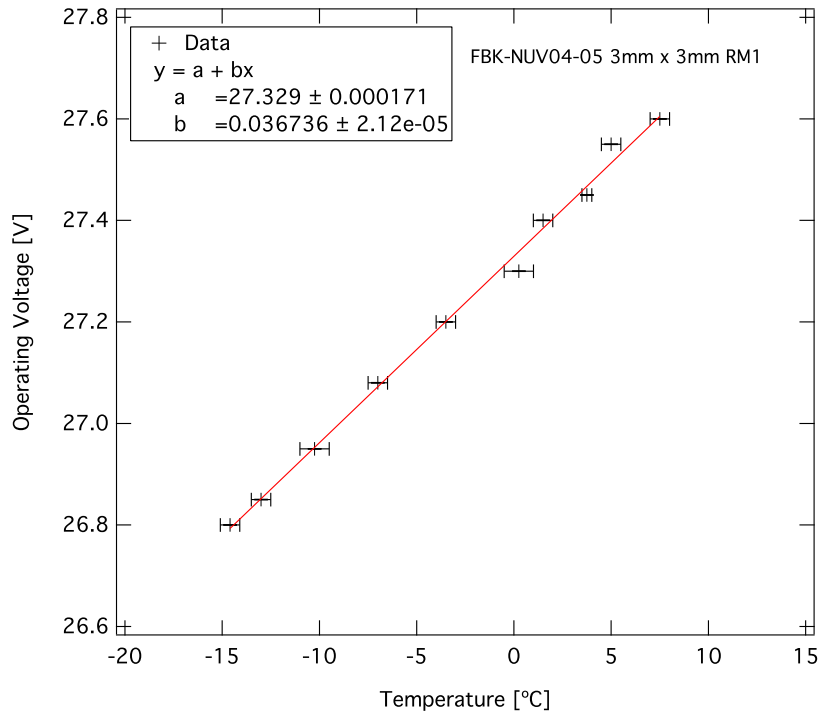


Figure 2.19: Operating voltage as function of temperature. Its dependence on the temperature results from fit to be about $36 \text{ mV}/^{\circ}\text{C}$.

All of the measurements about gain stabilization tests of this thesis are always calculated as shown in Figure 2.19.

It is obviously seen from the Figure 2.19, that a relatively small change in the

temperature of about 5 °C leads to a change of about 180 mV in the operating voltage. This would directly causes a change of the gain. Hence, many applications will need to keep the overvoltage stable during operation. This can be achieved by keeping the temperature stable as in this section, but for practical applications this might not be done easily. Another way to do it is to adjust the bias voltage to explain the temperature changes, with equation 2.5. This has been done by using the Arduino controller with voltage regulator chip (see chapter 4 and Figure 4.12). The Arduino micro-controller can monitor the temperature, with the temperature sensor (DS18B20) on the board and adjust the bias voltage accordingly. A test of this setup is described in the chapter 4.

CHAPTER 3

CHERENKOV LIGHT DETECTION FOR CTA PROTOTYPE CAMERA SYSTEM

In this section the detector setup to detect Cherenkov photons are introduced and their performance is summarized. The IACT technique is covered in more detail in section 3.2.

3.1 Introduction

Gamma ray astronomy is one of the most powerful tool for understanding the origin of cosmic rays. As a matter of fact, production of the gamma ray is connected to a complete collection of highly energetic celestial sources and events like as Active Galactic Nucleus (AGNs), SuperNovae Remnants (SNRs), Quasars and Gamma Ray Bursts (GRBs). The fundamental ground rules underlying their nature of these sources are not yet completely comprehended. Gamma ray astronomy has not only a huge potential in high energy astrophysics but also in particle physics, for the reason that the basic interactions associated to electromagnetic radiation such as bremsstrahlung, pair production, radioactive decay,...etc, for such high energy sources are observed even with high redshift. Hence getting a comprehension of our universes it is important to understand these different gamma ray sources and processes connected to them. By using the spatial telescope, the first gamma rays absorbed by atmosphere, were detected and verified by various experiments for years.

The recent discoveries and techniques permitted to the ground based experiments to contribute this research field. For instance, Imaging Atmospheric Cherenkov Telescopes (IACT) which were a greatest improvement in gamma ray astronomy

which were opened an access to energies beyond a few tens of GeV.

Cherenkov Telescope Array (CTA) is the next generation ground-based γ -ray instrument expanding the energy from a few tens of GeV to more than a hundred TeV with sensitivity by a factor of ten compared to current installations. It will also enhance angular and energy resolutions. These targets require the use of at least three different sizes of telescopes. In order to detect the low energy range (10 GeV - 100 GeV) there will be a few (3 - 6) Large Sized Telescopes (LST) in the center of the array, which will have a diameter of about 24 m. To observe the medium energy range (100 GeV - 1 TeV) there will be a number of Medium Sized Telescopes (MST). There will be a large number of Small Sized Telescopes (SST) for the very high energy range (more than 10 TeV). The telescope array is shown schematically in Figure 4.1. The final design of the array and the telescopes have not decided yet because the project is still in the preparatory phase [4]. This experiment is an international collaboration with more than 1000 members over 27 countries. The target of this collaboration is to construct an array of Imaging Air Cherenkov Telescopes (IACT) to observe the universe at very high energy. It is planned to build an array on the southern hemisphere consisting of up to 100 single telescopes in order to accomplish this target. It is also planned to build a smaller array of telescopes on the northern hemisphere to observe the full sky [21].

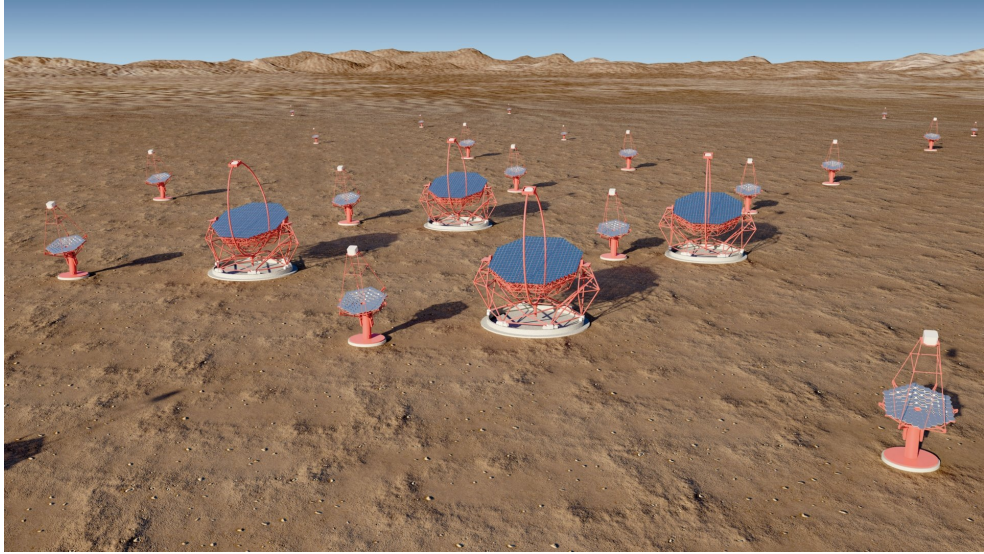


Figure 3.1: The telescope array (artist's impression), created by G.Pérez, IAC, SMM [21].

3.2 Theoretical Background

Imaging Air Cherenkov Telescopes (IACT)

The CTA collaboration constructs an array to detect the γ -radiation of the universe in the very high energy range. In order to achieve that there are two alternatives; first one is to watch the sky directly above the atmosphere since the atmosphere of the Earth is not transparent for these γ -rays and it is not possible to catch them directly with a ground-based telescope. This type of observation has some disadvantage because the satellite is restricted in size and the observation area is quite small. The second alternative is to observe γ -rays indirectly via so called Cherenkov light where the Earth atmosphere is used as a calorimeter. When high energetic γ -rays hit the atmosphere, they initiate a so called air shower. These secondary particles in the air shower give off Cherenkov light which is produced when the speed of particle is larger than the speed of light in the medium in which the particle is moving. The Cherenkov light is released in a wavelength range between 300 nm and 600 nm with a maximum at 400 nm and can be detected by an IACT. A typical electromagnetic shower can

be seen in Figure 3.2. Electrons and positrons are produced by pair production, while photons are produced by Brehmstrahlung.

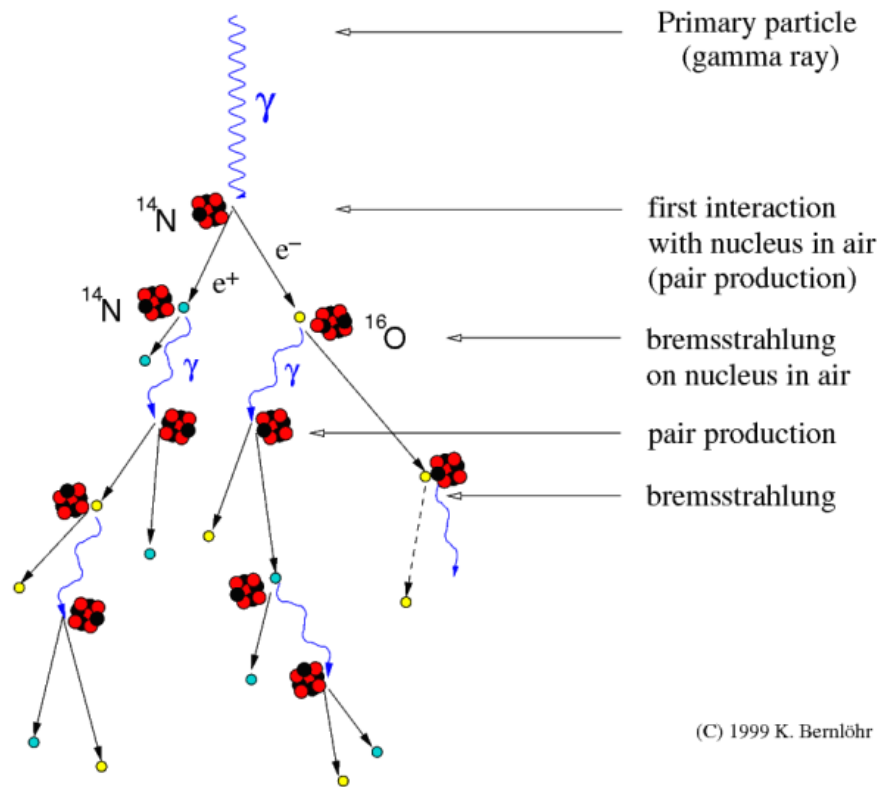


Figure 3.2: Sketch of air shower development is taken from Reference [22].

The released Cherenkov light forms a cone in the atmosphere and lightens the ground (see Figure 3.3). This Cherenkov light then is focused by a mirror plate into a camera consisting of photomultipliers. If the released Cherenkov light is detected by one single telescope (see Figure 3.3) the light will create a picture on the camera like in Figure 3.3. On the ground, the light area will lighten several kilometer-square. Therefore, a telescope will have a comparable effective collection area (it is enough for the telescope to be in the light pool). The large telescope arrays will be constructed to observe the showers more effectively, and also with better angular and energy resolutions. Well known examples of such existing arrays are MAGIC [23] and HESS [24]. CTA (Cherenkov telescope array), a new generation project of array, plans to improve the detection methods

used in the current telescope arrays in order to obtain a better flux sensitivity.

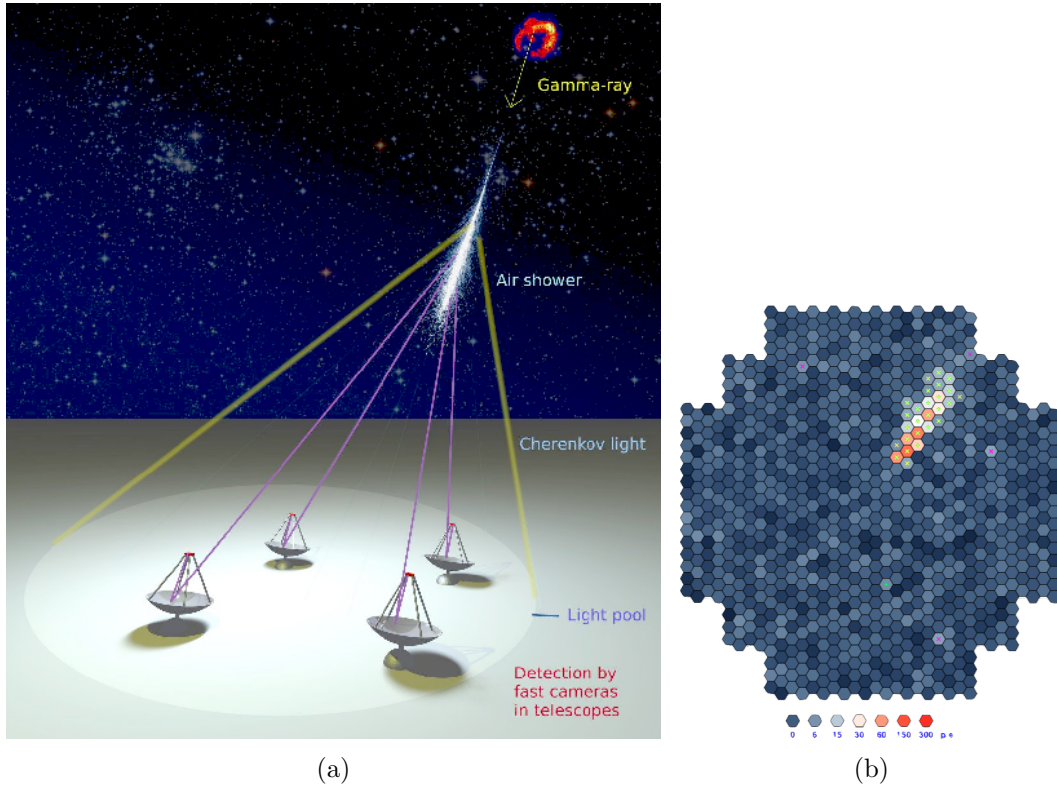


Figure 3.3: Schematic representation of the Cherenkov light cone, produced by a primary γ ray from inside a cosmic ray source (e.g. a supernova remnant) that lightens an array of telescopes (a). Pictures of detected Cherenkov light on one camera (b), taken by [25].

Cherenkov radiation:

Cherenkov radiation is produced when a charged particle travels faster than the speed of light in the traversed dielectric medium ($v > c/n$). The charged particle polarizes the molecules of the medium, which turn then back to their ground state and release light by doing so. In normal circumstances, the produced photons destructively interfere with each other and no radiation is detected. However, when a disruption which travels faster than light is propagating through the medium, the photons constructively interfere and intensify the observed radiation. The particle creates this way some kind of *photonic shock wave* which is detected as the Cherenkov cone of light (see Figure 3.4). The opening angle of

the Cherenkov cone is defined as

$$\cos(\theta) = \frac{1}{n \cdot \beta} \quad \text{where} \quad \beta = \frac{v}{c}. \quad (3.1)$$

The frequency spectrum of Cherenkov light is given by Frank-Tamm formula, which gives (in the following form), the number of photons released per track length d_x and for a wavelength λ :

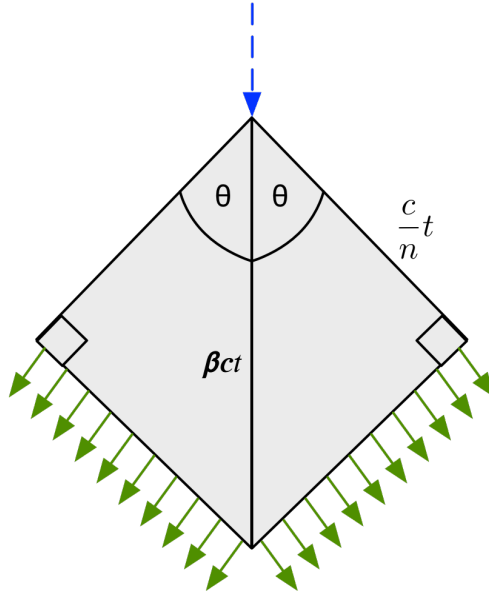


Figure 3.4: Sketch of the charged particle releases a wavefront of Cherenkov light at an angle θ which is the angle of the Cherenkov cone.

$$\begin{aligned} \frac{dN}{dx} &= \int_{\lambda_1}^{\lambda_2} \frac{1}{\lambda^2} d\lambda \cdot 2\pi \cdot \alpha \cdot z^2 \cdot \sin^2 \theta_C \\ \frac{dN}{dx} &= 2\pi \cdot \alpha \cdot z^2 \cdot \sin^2 \theta_C \cdot \left\{ \frac{1}{\lambda_1} - \frac{1}{\lambda_2} \right\} \end{aligned} \quad (3.2)$$

with the low wavelength end of the radiator transmission λ_1 , the high wavelength end of the photocathode quantum efficiency λ_2 , the fine structure constant α the charge of the incident particle z in units of the electron charge, and the Cherenkov angle θ_C .

3.3 Description of Detector Setup

The ultimate purpose of the camera is to catch Cherenkov light released in the higher levels of the atmosphere. However, to check the essential features of the camera module, a simple test using cosmic muons which are available at the ground level will be carried out. When a cosmic ray (mostly protons) hits the atmosphere, it interacts with the nucleons of the medium and generates a shower of electromagnetic and hadronic particles. In the specific situation of the proton cosmic ray smashing an atomic nuclei in the higher atmosphere, charged pions are produced and quickly decayed into muons and neutrinos. This is the main sources of muons at ground level and their features, make them a best candidate for simple detection. In the ultimate experiment, they will create Cherenkov light by traversing through a medium, and this Cherenkov light will be detected with the camera system. Muons have the greatest number energetic charged particles at sea level. This is because of the fact that they interact a few with matter besides by the ionization, their decay being mediated by weak interaction. The average muon flux at sea level is about 1 muon per minute per square centimeter. In order to test the new constructed camera system, a dedicated test procedure should be designed by using the only source of the Cherenkov photons which are cosmic muons in the laboratory. When a muon passes through the radiator, it may release Cherenkov photons. In order to collect these photons, the direction of the camera system should be adjusted in the direction of the produced Cherenkov photons. The output of the camera (1 SiPM) are digitized by an oscilloscope or Domino Ring Sampler Board v4 (DRS4, details in section 4.4.1). To perform this measurement, scintillator detectors have to be triggered by the muon expected within the acceptance angle and the direction of the radiator. The radiator, plexiglass material, has an advantages for the transmission of short wavelength photons. For this reason, it was selected to use in the setup. Finally, the whole

setup was covered by a dark cloth in order to isolate it from daylight. The first issue was the adjustment of the position and dimensions of the elements of the experiment (camera module, radiator, scintillators) and solved. The elements of the experiment are placed and aligned to the downward muons with the same axis (see Figure 3.7 (b)). The drawback of the setup is the large Cherenkov angle in the plexiglass. This leads to the produced photons to be reflected from the plexiglass-air interface. The phenomena is seen in the GEANT4 simulation [26] of the photons created by a muon traversing through the radiator medium in Figure 3.6. The reflections caused by the air interface between the radiator and the camera module would be discarded by stacking them in conjunction.

Silicon photomultipliers (SiPMs) are novel semiconductor photosensitive devices composed of an avalanche photodiode (APD) matrix on a common silicon substrate, and work in the limited Geiger mode [11, 12, 27]. They are proved to be competitive to traditional detectors of photons. However, the relatively large dark noise rate represents a difficulty for measurements of weak light signals. Especially, single photons are required in Cherenkov light detection. If one measures only signals in a sufficiently narrow time window, dark counts might be reduced while the detected Cherenkov photons are preserved. It is a challenge to attempt to use SiPMs for detection of Cherenkov lights.

The experimental set-up for measurement of Cherenkov photons is shown in Figure 3.5. After generating a trigger signal in the scintillator counters, the cosmic ray particle (generally muons at this level) and Cherenkov photons are registered by Domino Ring Sampler Board (DRS4). A 2.5 cm thick plexiglass radiator ($n = 1.497$) and SiPM detector with readout circuit are mounted on appropriate support (Figure 3.7). The test system consists of two scintillator counter boxes read by traditional PMT (Hamamatsu 5783) and a SiPM (FBK - NUV 04-05) which is $3 \times 3 \text{ mm}^2$. The PMTs have been studied well by our group, and their characteristics are well known. So they serve as a reference to check the signal

of the SiPM. GEANT4 simulation of the Cherenkov photon produced while a

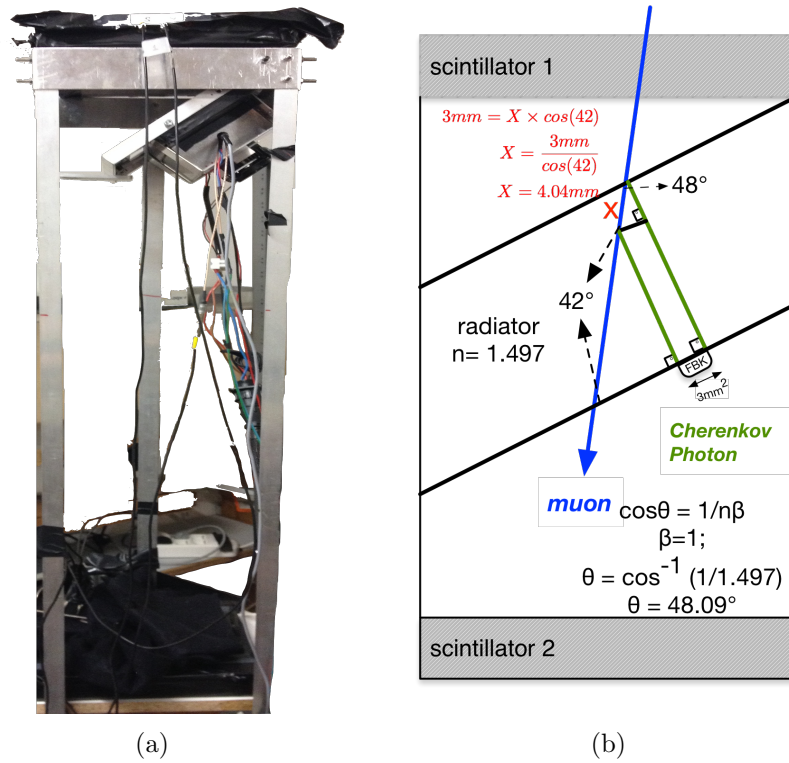


Figure 3.5: (a) The experimental Setup which includes 2 Kuraray scintillator boxes ($20 \times 20 \times 1.4 \text{ cm}^3$ dimension) with readout by Hamamatsu 5783 PMTs, are separated by 96 cm apart each other and one plexiglass radiator box with an angle of 48° . (b) shows that its schematic view.

muon passing through the radiator medium with incoming angle about 48° and 300 MeV energy and the produced Cherenkov photons internally are shown in Figure 3.6.

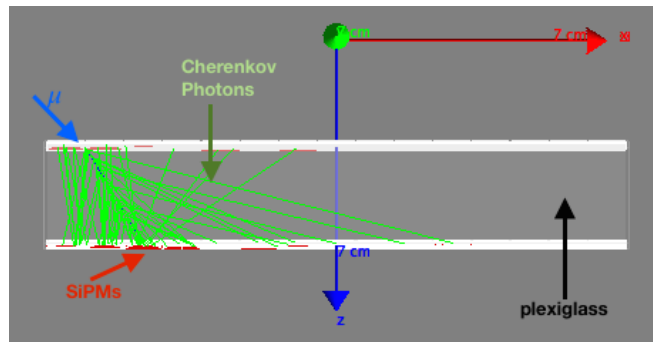


Figure 3.6: Simulation of the Cherenkov photons while a muon passing through the radiator medium.

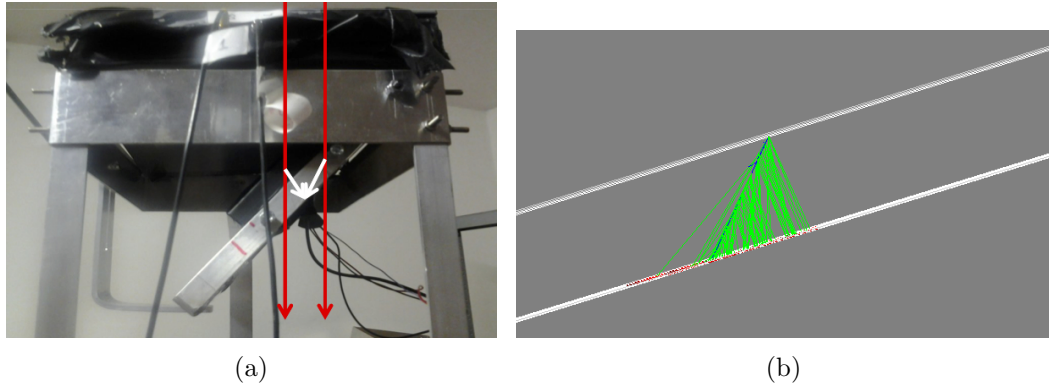


Figure 3.7: (a) A close-up view of the radiator and the photon detector on their supports in the frame. The radiator has an angle around 48° with scintillator counter 1, (b) shows the simulation of the setup to produce Cherenkov photons inside the radiator.

We use two scintillators to trigger on the events that have the desired angle and direction. We plug these two scintillators into external Trigger board described in the thesis [28], that includes a coincidence logic circuit to report when both scintillators detect a signal. We then analyze these coincidence signal recorded by the DRS4 board to estimate the counting rate of the muons. The observed coincidences rate of our scintillators, described in Figure 4.1, was at the order of mHz. At first, we have to do some measurements to characterize the camera module and the signals received from the setup. An oscilloscope was used to have a first idea of the signals which have been received. The signals from two scintillator detectors were recorded and the peaks were observed in the same gated time window. These are called the expected muons in the setup (see an example of a muon trace on Figure 3.8). The SiPM signal was also recorded on the scope for estimation of the photoelectron peak separation. In the estimation of the photoelectron peak separations, each photoelectron peak was integrated in terms of charge distribution of the SiPM signal in a given time window, ~ 8 ns, (seen in Figure 3.9). During the measurements, the scintillators were triggered with a rate around 3.9 mHz. Since this detection rate is quite low, the measurements was done for every 24 hours period. Analyzing the each trace was

done by using a Fortran code working on Physical Analysis Workstation (PAW). We consider a voltage peak with regard to an arbitrary threshold voltage in the gated window.

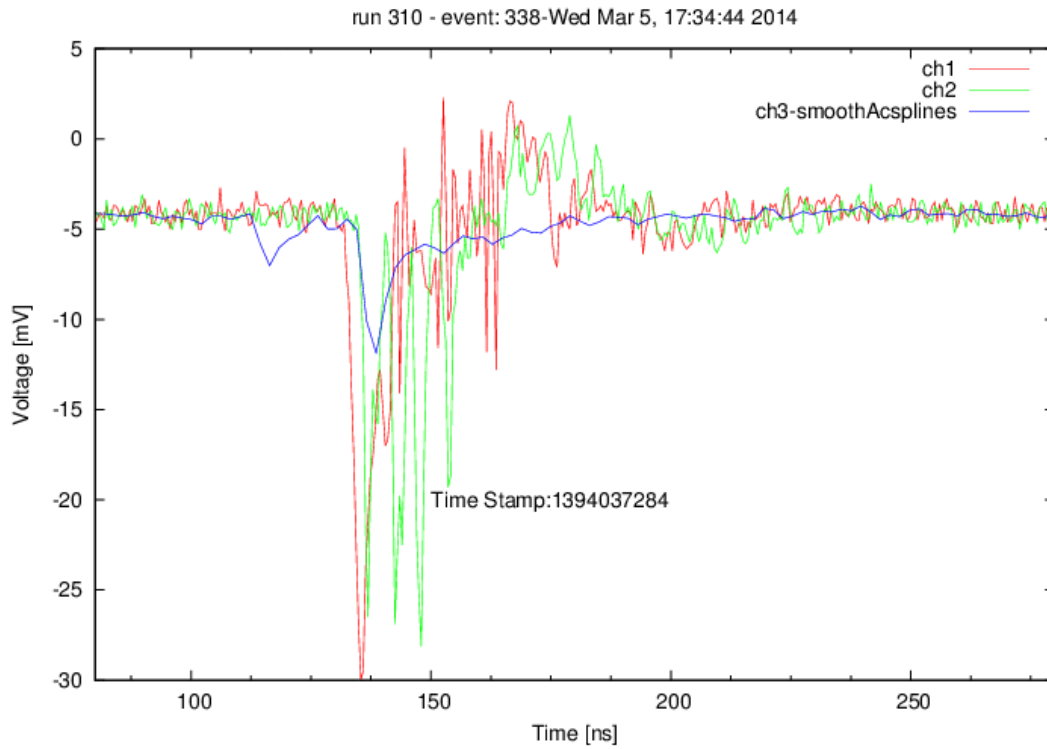


Figure 3.8: The Cherenkov light produced by a muon (blue) going through the radiator, the red trace is representing muon passing through scintillator 1, and green for scintillator 2.

As seen from the Figure 3.9 photoelectrons are clearly separated. The color spectrum goes through reddish to violet. The reddish one represents the first p.e and bluish one is the second p.e and etc.

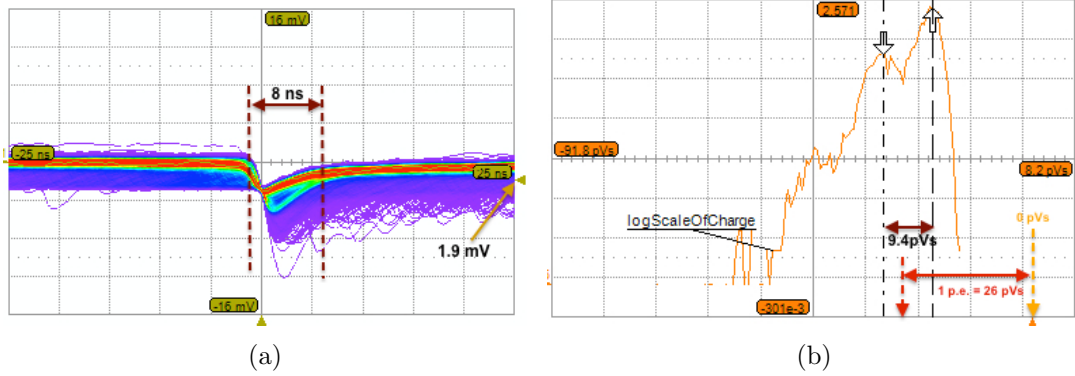


Figure 3.9: FBK SiPM thermal photoelectron separation distribution in the given integration time window.

The total charge distribution histogram of the registered SiPM signals from run 305 to 311 covering 7 days data are shown in Figure 3.10 & 3.12 and the events considered as muons have a peak greater than 2000 pVs as shown in Figure 3.10 (a) and in (b).

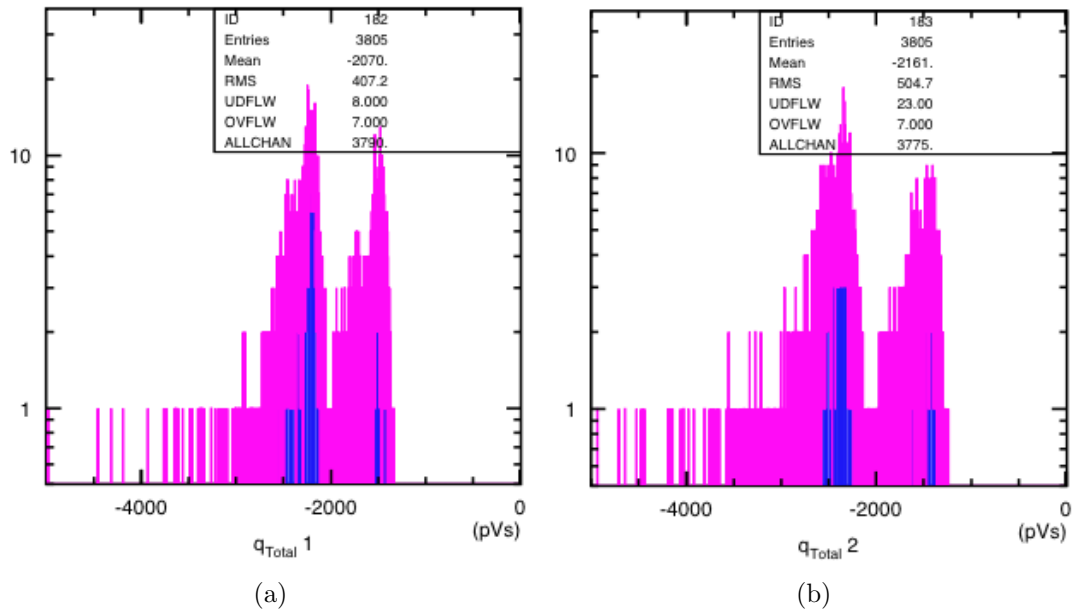


Figure 3.10: Charge Distributions of the *muon signals* passing through scintillator 1 shown in (a) and scintillator 2 in (b). In the x axis, the peak, is around lower than 2000 pVs, corresponds to pedestal and noise signals in the region of interest window, the second peak, above 2000 pVs, corresponds to the signals.

Figure 3.11 depicts that the Time Of Flight (TOF) distribution of the muon events which are passing through from scintillator 1 to scintillator 2. The muons which have a TOF distribution around 3.104 ± 0.029 ns are used as a trigger for the DAQ.

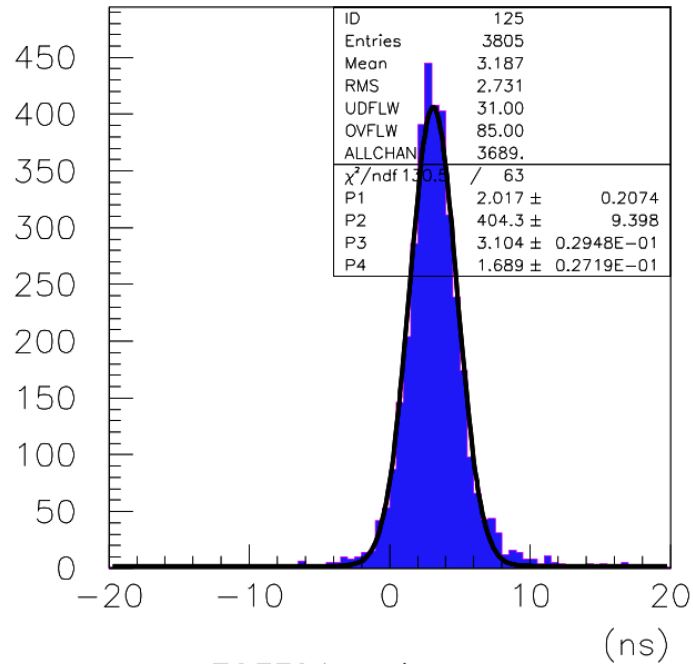


Figure 3.11: The time of flight distribution of the muon signal passing through the scintillator 1 to scintillator 2.

In the figure 3.12 the total charge distribution integrated in full window (0-512 ns) includes baseline (or pedestal) plus Cherenkov photon signal and the signals which are coming randomly. The lower peak (in terms of absolute value), is less than 2000 pVs, corresponds to the pedestal, where the second peak corresponds to the signals coming anywhere in the full integration window, (b) depicts that the charge integrated in the Cherenkov signals.

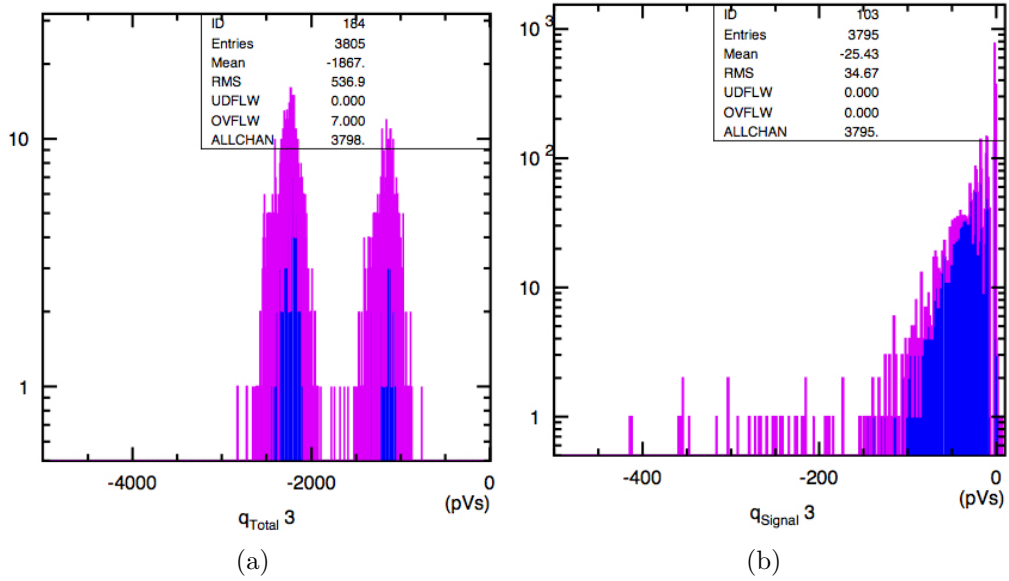


Figure 3.12: Charge Distributions of the *Cherenkov signals*. In the x axis, every 26 pVs corresponds to 1 p.e. In Figure (a) the total charge integrated in full window (0-512 ns), which includes baseline plus signals coming out of the trigger window. The lower peak (in terms of absolute value) corresponds to the pedestal, the second peak corresponds to the signals. Figure (b) shows the total charge integrated in the gated window.

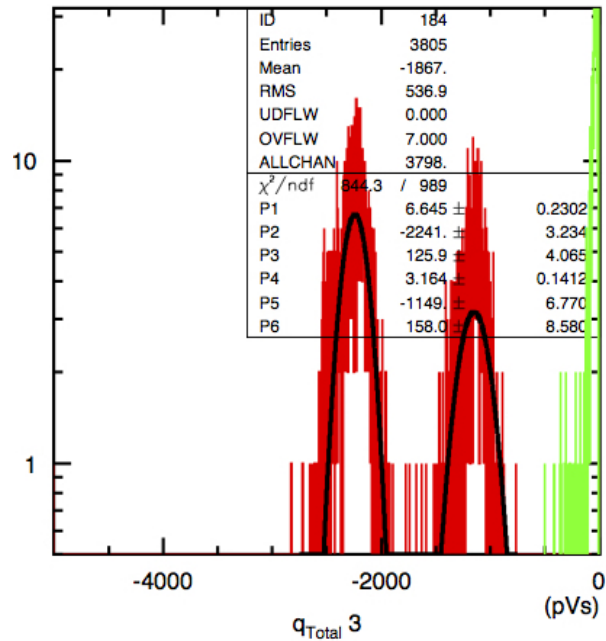


Figure 3.13: Charge Distributions of the *Cherenkov signals* the green peak shows that the charge integrated only the signals which are trigger region.

Figure 3.13 shows all plots in superimposed mode and two gaussian fits; one for pedestal and one for all signals coming in the full window.

3.4 Estimation of the Number of Cherenkov Photons in Radiator

To determine the number of photons released by a muon passing through our radiator, modified version of the Frank-Tamm formula 3.2 is applied. We integrate on the part of the Cherenkov spectrum where the sensitivity range of the FBK SiPM is from 300 nm (λ_1) to 600 nm (λ_2). Assuming that quantum efficiency is 100% and we evaluate the Cherenkov angle shown in Figure 4.1, $\sim 48.09^\circ$. We find that a muon passing through a layer of radiator at a speed $\beta \sim 1$ produces 423 Cherenkov photons per cm in the integrated wavelength range. These photons are released in all the directions of the Cherenkov cone. In order to figure out how many of these photons reach the surface of the SiPM module (i.e. the window), the location of the the SiPM with respect to the muon trajectory should be determined. In our setup, the SiPM module is touched to the radiator, and its area is about 9 cm² shown in equation 3.4. The area of the produced Cherenkov cone can be estimated in equation 3.5 for the muon travelled inside the radiator is about 51.07 mm². The expected number of Cherenkov photons, reaching the SiPM travelled distance 4.04 mm in the acceptance of the SiPM, is 22.2 photons.

The produced Cherenkov photons, inside a medium, can be estimated by using the formula given in the equation 3.2. Limiting factors are the finite transmittance of the radiators 80% above 390 nm for Plexiglass, and the geometrical acceptance of the photodetector. The sensitivity range of the FBK SiPM is from λ_1 , 300 nm to λ_2 , 600 nm, and if we assume that it is quantum efficiency is 100%. So the produced photons is

$$\begin{aligned} \frac{dN}{dx} &= 2\pi \cdot \frac{1}{137} \cdot \left\{ \frac{1}{3} - \frac{1}{6} \right\} \cdot \frac{10^5}{cm} \cdot \sin^2(48.09) \\ \frac{dN}{dx} &= 423 \cdot \frac{\text{photons}}{cm} \end{aligned} \quad (3.3)$$

and the area of the SiPM is defined as

$$\begin{aligned} A_{SiPM} &= a^2 \\ &= (3 \text{ mm})^2 = 9 \text{ mm}^2 \end{aligned} \quad (3.4)$$

and the area of the Cherenkov cone, A_{cone} , is defined as

$$\begin{aligned} A_{cone} &= \pi \cdot R^2 \\ &= \pi \cdot (4.03 \text{ mm})^2 = 51.07 \text{ mm}^2 \end{aligned} \quad (3.5)$$

the ratio of the area for two geometry is

$$\begin{aligned} A_{Ratio} &= \frac{A_{SiPM}}{A_{cone}} \\ A_{Ratio} &= \frac{9 \text{ mm}^2}{51.23 \text{ mm}^2} = 0.176 \end{aligned} \quad (3.6)$$

total produced photons in the radiator is

$$\begin{aligned} dN &= 423 \frac{\text{photons}}{\text{cm}} \cdot 0.404 \text{ cm} \\ N_{max} &= 170.5 \cdot \text{photons} \end{aligned} \quad (3.7)$$

and the total expected photons in the SiPM area where the SiPM is placed on the center of the Cherenkov cone is given as

$$\begin{aligned} N_{tot} &= N_{max} \cdot A_{Ratio} = 170 \cdot 0.176 \\ N_{tot} &= 30.0 \text{ photons} \end{aligned} \quad (3.8)$$

In the geometrical acceptance of the $3 \times 3 \text{ mm}^2$ where the $\phi = 0.74$ maximum expected number of photons on the side of the Cherenkov cone, so the expected

number N is

$$N_{expected} = 22.2 \text{ photons} \quad (3.9)$$

The produced Cherenkov cone diameter will be enlarged to the 3.22 cm when we install a new FBK - NUV SiPM array, have a surface area around $1.2 \times 1.2 \text{ cm}^2$ (shown in Figure 3.14).

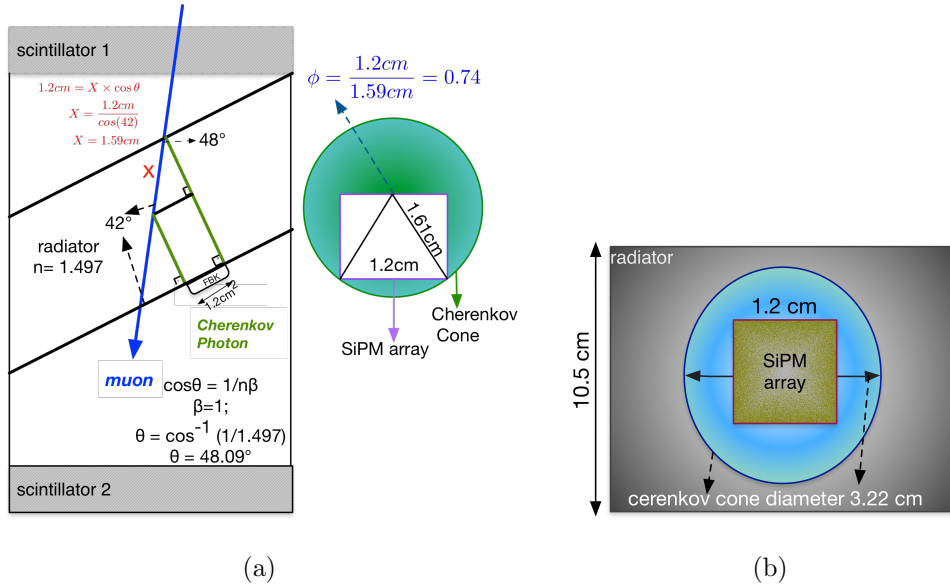


Figure 3.14: (a) Schematic view of FBK-NUV SiPM array setup, (b) Schematic view of the acceptance of FBK-NUV SiPM array setup.

At these circumstance the expected number of Cherenkov photons can be estimated by using above formula; the area of the SiPM is defined as

$$\begin{aligned} A_{SiPM} &= a^2 \\ &= (1.2 \text{ cm})^2 = 1.44 \text{ cm}^2 \end{aligned} \quad (3.10)$$

and the area of the Cherenkov cone, A_{cone} , is defined as

$$\begin{aligned} A_{cone} &= \pi \cdot R^2 \\ &= \pi \cdot (1.59 \text{ cm})^2 = 6.43 \text{ cm}^2 \end{aligned} \quad (3.11)$$

the area ratio of two geometry is

$$\begin{aligned} A_{Ratio} &= \frac{A_{SiPM}}{A_{cone}} \\ &= \frac{1.44 \text{ cm}^2}{6.43 \text{ cm}^2} = 0.22 \end{aligned} \quad (3.12)$$

total produced photons in the radiator is

$$\begin{aligned} dN &= 423 \frac{\text{photons}}{\text{cm}} \cdot 1.59 \text{ cm} \\ N_{max} &= 672.6 \text{ photons} \end{aligned} \quad (3.13)$$

$$(3.14)$$

and the total expected photons in the SiPM area where the SiPM is placed on the center of the Cherenkov cone is given as

$$\begin{aligned} N_{tot} &= N_{max} \cdot A_{Ratio} \\ N_{tot} &= 672.6 \cdot 0.22 \\ N_{tot} &= 147.97 \text{ photons} \end{aligned} \quad (3.15)$$

In the geometrical acceptance of SiPM array $1.2 \times 1.2 \text{ cm}^2$ where the $\phi = 0.74$ maximum expected number of photons N is

$$N_{expected} = 109.5 \text{ photons} \quad (3.16)$$

CHAPTER 4

COSMIC RAY DETECTION STUDIES AT SPHINX OBSERVATORY CENTER

4.1 Theoretical Background

The Cosmic Rays (CRs) are mainly high energy protons and heavier nuclei accelerated by astrophysical Galactic and extra-Galactic objects. Although they come directly from the astrophysical objects of interest, it is impossible to point back to their source position in the sky because they are deflected from the galactic and extragalactic magnetic fields. Also neutral cosmic messengers have some limitations: neutrons decay after they travel relatively long distances, while γ -ray photons have a limited travel due to their interactions with the electromagnetic background light. In this scenario, neutrinos seem to be very interesting particles to study astrophysical phenomena: they do not suffer deflection from magnetic fields because they are neutral, they are stable particles and they interact only weakly. The scintillation detector prototype is composed of 4 scintillation tiles. The detection principle is based on the reconstruction of the muonic neutrino (ν_μ) track direction using the light emitted by charged-particles, created by neutrino interaction. Muon showers produced by charge-current interactions are important because of they are the charged leptons with longest range in the atmosphere. In addition muon showers retain almost the same direction of their parent neutrinos. The aim of this section is the detection of the cosmic ray coming from at large zenith angle with SiPM readout board. This detector prototype will be part of a large area (several square kilometers) surface array designed to measure Ultra High Energy (UHE) (0.01-100 PeV) neutrinos by using the Earth Skimming strategy [29].

4.2 Description of the Detector Prototype

The hardware of the detector prototype consists of two identical scintillator counters, named *tower*, separated by 160 cm apart as seen in Figure 4.1.



Figure 4.1: Prototype detector installed at Sphinx (HFSJG) to test upward / downward particles separation, environmental effects.

Each counter consisting of a Kuraray organic scintillator panel ($20 \times 20 \text{ cm}^2$, 1.4 cm thick). The solid angle of a single tower is about $4.0 \times 10^{-2} \text{ sr}$ and its zenith angle covers $\pm 7.5^\circ$ around the axis. The geometrical acceptance is $255.0 \text{ cm}^2\text{sr}$. The scintillator has excellent features, in the view of obtaining the precise timing information, such as producing the light in blue region of the spectrum, the emission peak is around 430 nm . Each scintillator panel wrapped in Tyvek paper for diffusing the reflection, and one SensL silicon photomultiplier ($3 \times 3 \text{ mm}^2$) contacted to read the produced signal. This SiPM has short output pulse of $< 2 \text{ ns}$ at FWHM. The bias voltage of this device is about 27.5 V and the

dynamic range over the breakdown voltage is ~ 2 V. Hence the filling factor of the device is 64%, the gain is 2.3×10^6 . The produced signal is digitized by Domino Ring Sampler Board (DRS4), developed by Stefan Ritt [30]. The DAQ is based on waveform sampling at 2 GS/s, covering a $2.5 \mu\text{s}$ window. The aim of this detector is select horizontal tracks to detect tau shower produced by the neutrino interacting in Earth crust. So this can be achieved with a time of flight (TOF) resolution of 0.5 ns without using any shielding material. In the following, we will describe the detector components such as scintillator, Domino Ring Sampler (DRS4) board.

4.3 Scintillators

Scintillator detectors are extensively utilized in nuclear and particle physics for particle and γ -ray observation, through the releasing of light due to incoming particles making interaction with the detector. The released light is afterward gathered and amplified in a SiPM, where the scintillation is turned into electrical pulses. These pulses are further analyzed, each pulse gives us a a lot of information such as sensitivity of energy, fast time response and pulse-shape discrimination with respect to the interaction of the incoming particle within the scintillator.

A. Sensitivity to Energy: Because of most scintillators have almost same linearity in the deposition of the energy means that the light output of the scintillator is directly proportional to the exciting energy. So the amplitude of the final collected signal is also proportional to the this energy.

B. Fast Response Time: Because of having fast response and recovery time of scintillation detectors they can provide high precision timing information between two events so that leads to higher count rates.

C. Pulse-Shape Discrimination: The technique is known as *pulse-shape discrim-*

ination is to distinguish between types of particles by analyzing the shape of the collected signal pulses. At present, there are six types of scintillators but commonly used types are organic scintillators and inorganic crystals, each having a different mechanism responsible for its output of light. This section will examine how these mechanisms work for each type of scintillator, and what this ultimately means when detecting light. So we will deeply describe the organic scintillators in the following section, and briefly commenting on the other types of scintillators for completeness.

4.3.1 Organic Scintillators

Organic scintillators are composed of hydrocarbon compounds, containing benzene cycle. They are commonly found in both liquid or crystal form, with the former usually a combination of various organic scintillators in a solvent. Their most distinguishing property is a very rapid decay time on the order of a few nanoseconds or less. The scintillation mechanism for this variety of detector is due to transitions made by free valence electrons in the molecule, thus making it strictly due to the chemical nature of the scintillator.

4.3.1.1 Energy Levels in Organic Scintillators

The fluorescence mechanism in organic materials appear from changes in the energy levels of a *single* molecule. Majority of the feasible organic scintillators are organic molecules which have symmetry effects related to the electron structure. Detached electrons filling the π -molecular orbitals in the material get excited in the ionization interaction, consequently an excitation to electron and vibrational levels. Energy from a charged particle is absorbed and excited states - the singlet states (spin = 0) are labeled S_1, S_2, S_3 and the triplet states are T_1, T_2, T_3, \dots which are shown in Figure 4.2. In the π -molecular orbital, there are various singlet and

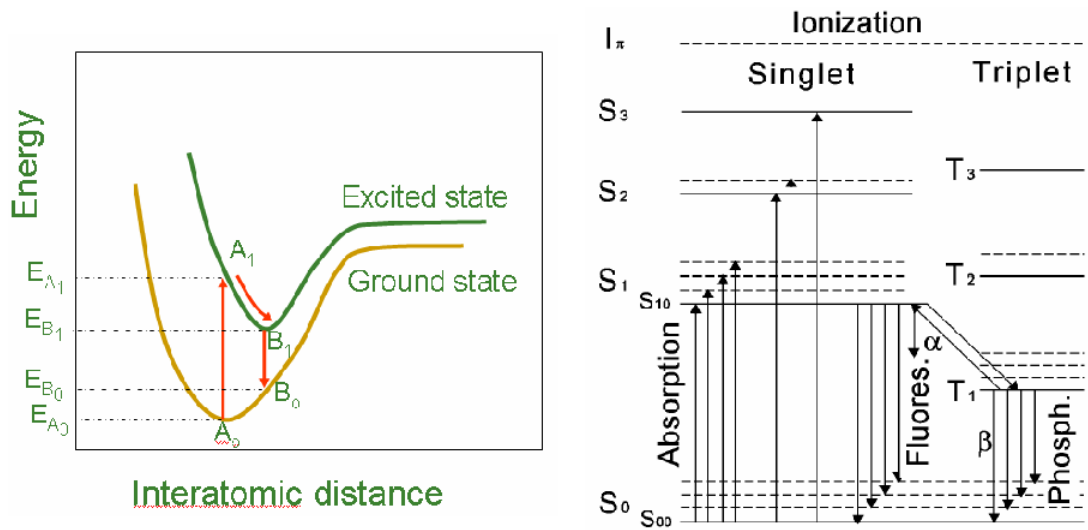


Figure 4.2: Energy levels of organic molecules.

triplet spin states, with the ground state of the system represented by the S_0 , singlet state. Any levels over this state are an excited differences of both the singlet and triplet states, with the ground system of the triplet state being T_0 . At both the ground and excited levels of the single and triplet spin states exist a fine structure, with energy spacings of the order of a few keV, associated with the vibrational modes each molecule can have. The derivation of these variety of states is entirely a quantum mechanical effect. Quantized angular momentum gets the form:

$$\|S\| = \sqrt{s \cdot (s + 1) \cdot \hbar} \quad (4.1)$$

where $\|S\|$ is the norm of the quantized spin vector, s is the spin quantum number related to spin angular momentum and \hbar is the reduced Planck constant. Given a direction, z , spin projection on this axis is given by:

$$s_z = m_s \cdot \hbar \quad (4.2)$$

Where m_s is the secondary quantum number that span from $-s$ to $+s$ in steps of one, which leads to values of $2s + 1$ as values for m_s . Hence both spin vectors S_1 and S_2 are quantized, for the electron, there exists only two directions along the z-component which results in a "spin-up" and "spin-down" term; $S = \pm\hbar/2$. If $S_1 = -S_2$ (i.e. anti-parallel), then the total spin is $S_T = S_1 + S_2 = 0$, where the magnitude of the total spin is 0 and the quantum number, m_s , has to be zero. If S_1 and $S_2 \neq 0$, then the vector is also non-zero. The only non-zero value is \hbar in magnitude, which leaves; $m_s = -1, 0, +1$, which are triplet states. A single spin state with total spin of zero is known as a singlet state. The singlet state is anti-symmetric with respect to the exchange of the spin, and follows a two electron spin state:

$$\Psi_s(S_1, S_2) = \frac{1}{\sqrt{2}} \cdot [\Psi_{\uparrow}\{S_1\} \cdot \Psi_{\downarrow}\{S_2\} - \Psi_{\uparrow}\{S_2\} \cdot \Psi_{\downarrow}\{S_1\}] \quad (4.3)$$

Similarly, a triplet state where $m_s = -1, 0, +1$, is described as:

$$\Psi_{t,m=1} = \Psi_{\uparrow}\{S_1\} \cdot \Psi_{\uparrow}\{S_2\} \quad (4.4)$$

$$\Psi_{t,m=0} = \frac{1}{\sqrt{2}} \cdot [\Psi_{\uparrow}\{S_1\} \cdot \Psi_{\downarrow}\{S_2\} + \Psi_{\uparrow}\{S_2\} \cdot \Psi_{\downarrow}\{S_1\}] \quad (4.5)$$

$$\Psi_{t,m=-1} = \Psi_{\downarrow}\{S_1\} \cdot \Psi_{\downarrow}\{S_2\} \quad (4.6)$$

Singlet excitations degrade within a few picoseconds without releasing of radiation known as internal decay. The transitional state, S^* , goes through a most likely radiative decay to one of the vibrational states in S_0 , known as fluorescence, reported by the prompt component Figure 4.2. A similar internal decay process is found in the triplet spin system, although without an intermediate step. Transitions from T_0 to S_0 are mostly disallowed by multipole selection rules. It is more suitable for the T_0 state to interact with a molecule at the ground state and thereafter decay to the intermediate and ground states in the singlet spin

state alternatively, creating phonon emission. This process is in charge of the postponed component in scintillator light. It is this molecular structure of the luminescence process in these organic scintillators which make them an important alternative to common scintillators for identification of the particle.

4.3.1.2 Scintillation Mechanism in Organic Scintillators

When scintillator materials, because of having the property are known as *luminescence*, exposed to certain form of energy (light, radiation, heat etc. . .) absorb and emit the energy in the visible light form. If this emission occurs immediately after absorption or within $10^{-8}s$ (atomic transition time), the process is usually called *fluorescence*. If it has a delay due to the excited state is metastable, the process is called *phosphorescence*. So the scintillation mechanism in organic materials is the *fluorescence* mechanism, arises from transitions in the energy levels of a single molecule and therefore the fluorescence can be observed independently of the physical state. Because of the average energy is about 0.025 eV, at room temperature, all molecules are in the S_{00} state. When the charged particle passes through, kinetic energy is absorbed by the molecules, and electrons are excited to the upper levels. The higher states S_2, S_3 , de-excite quickly ($\sim 10^{-12}$ s) to S_1 state through radiation-less transitions (internal conversion). The states such as S_{11}, S_{12} that have extra vibrational energy and are not in thermal equilibrium with neighboring molecules, quickly lose energy. After in a short time a population of excited molecules in S_{10} state is produced as the net influence of the excitation process. Scintillation light, (prompt fluorescence) is released in transitions between S_{10} and ground state. The prompt fluorescence strength at time t succeeding excitation is characterized by

$$I = I_0 e^{-\frac{t}{\tau}} \quad (4.7)$$

where τ is the fluorescence decay time for the S_{10} level. In the majority of organic scintillators, τ is the order of a couple of nanoseconds thereby organic scintillators are **fast**. The lifetime for the T_1 is considerably prolonged than the S_1 state. T_1 is populated by a transition called an inter-systems crossing. The lifetime of the T_1 state can be ms. Transitions from T_1 to S_0 give rise to phosphorescence (delayed light emission). T_1 lies below S_0 , for that reason the wavelength of the released phosphorescence is long-lasting than the wavelength of the fluorescent light. The phosphorescent light can be distinguished from the scintillation light in terms of timing and wavelength. The energy-level diagram, shown in Figure 4.2, describes why organic scintillators can be transparent to their own fluorescence emission. All fluorescence emissions (except $S_{10} \rightarrow S_{00}$) have a lower energy than the minimum required for absorption. There is a small overlap between emission and absorption spectra, thus the released light generally passes straight on through the scintillation medium. So while selecting a good scintillator detector one should care the following requirements [31, 32]:

1. high efficiency for conversion of exciting energy to fluorescent radiation
2. transparency to its fluorescent radiation to allow the light transmission.
3. a short time decay constant
4. emission in a spectral range consistent with the spectral response of existing photomultiplier.

However we use KURARAY organic scintillators, which are $20 \times 20 \text{ cm}^2$ and 1.5 cm thick is shown in Figure 4.3 have the properties shown in Table 4.1.

Table 4.1: Physical parameters of KURARAY SCSN-61 scintillator.

Description	Light Output	Peak of Emission	Attenuation Length	Decay Time
SCSN-61	55% Anthracene	430 nm	0.92 m	2.5 ns



Figure 4.3: KURARAY organic scintillator $20 \times 20 \text{ cm}^2$ and 1.5 cm thick.

Test sample's sizes of described above are $1500 \text{ mm} \times 50 \text{ mm} \times 10 \text{ mm}$, and the emission spectra is shown in Figure 4.4.

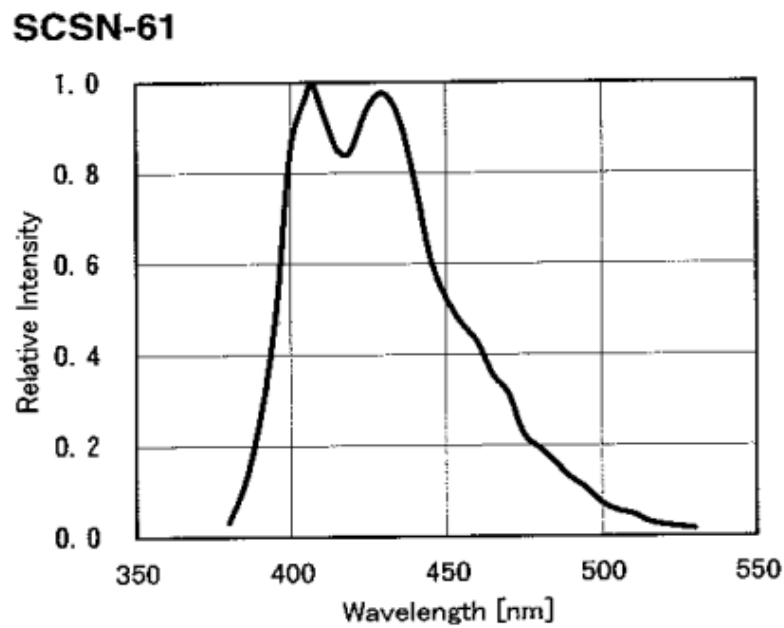


Figure 4.4: Emission spectrum of the KURARAY SCSN-61 scintillator [33].

4.3.1.3 Plastic Scintillators

Plastic scintillators are the commonly used of the organic scintillators because of their exceptional fast timing properties. Plastic scintillators, like organic liquids, are solutions of different organic scintillators in a solid plastic solvent.

Remarkably fast signals make plastic scintillators very attractive, as they have abnormally high light yield, and a decay constant of the order of 2-3 ns. They can also be smoothly cut and arrange into various shapes, thus making them cost efficient as well.

4.3.1.4 *Inorganic Scintillators*

Inorganic scintillators are the mostly used scintillator in the field of nuclear and particle physics with high stopping powers and high light yields. Inorganic scintillators are mainly alkali halide crystals which include a few activator contamination. This contamination that plays a fundamental role in one of the processes behind the scintillation mechanism. The scintillation mechanism in organic scintillators is discussed in section 4.3.1.2. There is two processes can be seen when incident radiation interacts with the scintillator crystal, The first one is, *ionization* inside the crystal which occurs since the excitation of an electron from the valence band to the conduction band that produces a free electron-hole pair. However, the second process requires the creation of an exciton; the excitation of an electron from the valence band to a exciton band just below the conduction band. The electron-hole pair persists delocalised, are free to move throughout the crystal. Hence, the presence of an activator or impurity behaves as a generator of electron levels, happening in the earlier forbidden energy gap. This means that the impurity builds a pitfall by which any moving created electron-hole exciton pair moving near the impurity can undergo ionization with the corresponding atom. Free electrons can also fall into any holes left behind and make a transition from its excited state to the ground state, emitting radiation when it is allowed. Other extra "exotic" processes, spans scintillator afterglow and quenching. Afterglow appears due to the detrapping and recombination of charge carriers for the time of long periods of excitation, which results in a postpone of the scintillation light, because of an increase in the decay time of the electrons to the ground

state. Quenching effects concluded with no emission of radiation, and a reduced light output since the deexcitation processes in the scintillator mechanism.

The SiPM readout of the detector prototype delivers fast signals about 5 ns FWHM wide and the readout used a FADC running at 2 GSamples/s. For fast muon pulses, a FADC with 2 GSamples/s can provide at least four sampling points. This allows a reasonable reconstruction of the pulse shape and could yield an improved particle identification based on the timing information.

4.4 Switched Capacitor Array Chip

Flash ADC technique is frequently applied for sampling and converting ultra-fast signals. Switched Capacitor Array (SCA) is used as a ring buffer that can sample progressively the signal till pulled down by an external trigger. Once the last cell is written, it overwrites the first one. The array registers the previous information in the N-1 cells. This leads to a postpone in the sampling period and the array depth, which is 120 ns for a 128-cell array at 1 GHz sampling rate. This rate synchronized by an external clock at the sampling rate divided by the array depth. The first idea of a SCA was the Domino Sampling Chip (DSC), a fast analog memory fabricated in CMOS technology in 1989 [34].

In the case of the detector prototype the new data acquisition system is based on an ultra-fast analog-sampler, the Domino Ring Sampler version 4 (DRS4), with a frequency from 1 GSamples/s to 5 GSamples/s, and high resolution digitizers, 11 bits. The DRS4 is a SCA chip for fast waveform sampling of photomultiplier developed at Paul Scherrer Institute, Villigen Switzerland by Stefan Ritt. It is capable of digitizing nine channels at sampling speed up to 5 GSPS. It has SMA connectors for four input channels, each with 1024 capacitive sampling cells. Waveform digitizing takes place with an on-chip generated frequency ranging from 0.5 GHz to 5 GHz.

4.4.1 The Domino Ring Sampler chip version 4

The Domino Ring Sampler consist of an on-chip inverter chain generating a sampling frequency up to 5 GHz (domino wave circuit), eliminating the need to feed an external sampling clock in the GHz range into the chip. This signal opens a series of writing switches in all 8 sampling channels, where the single-ended input signal is sampled by low value (200 fF) capacitors. After being started, the domino wave runs continuously in a ring fashion until it is decoupled from the write switches by a trigger signal, which freezes the current stored in the sampling capacitors. The signal is then readout via a read shift register for external digitizers. A schematic view of DRS4 is shown in Figure 4.5.

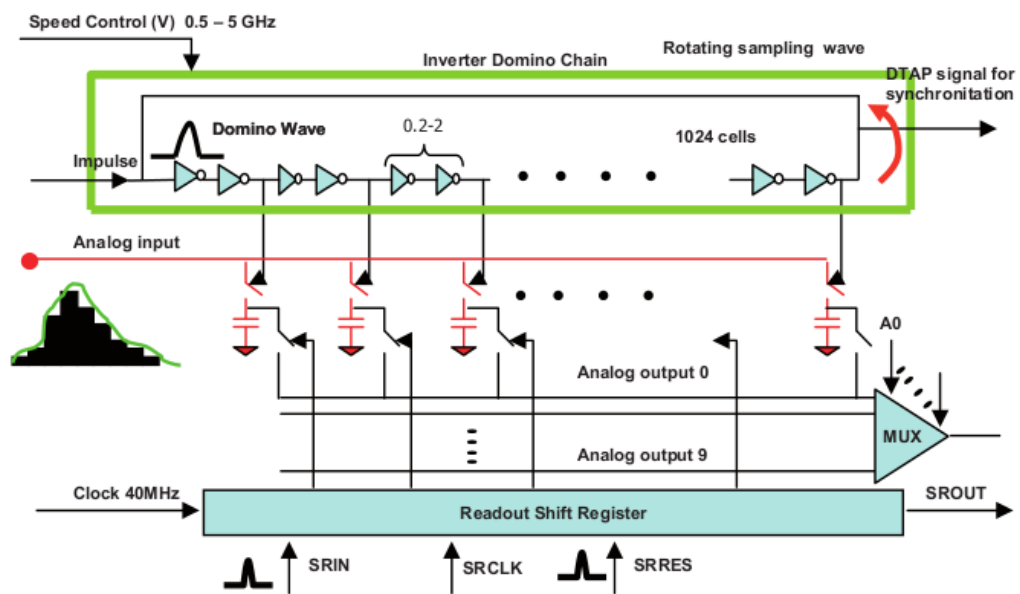


Figure 4.5: Schematic drawing of DRS4 chip [35].

4.4.2 The Domino Wave Circuit

The domino wave circuit is essentially a series of 1024 double inverters. After pushing up the DENABLE signal, a wave passes through these inverters providing the write signal for sampling cells. Figure 4.6 depicts a simplified schematic of three double inverter blocks. The first inverter is in reality an AND gate. This

permits to enable and to stop the domino wave at any time via the DENABLE. The domino wave runs continuously until it is stopped by a trigger signal that pulls down the DENABLE signal, disabling the WRITE signal and freezing the current stored the signal in the sampling capacitor [28, 35].

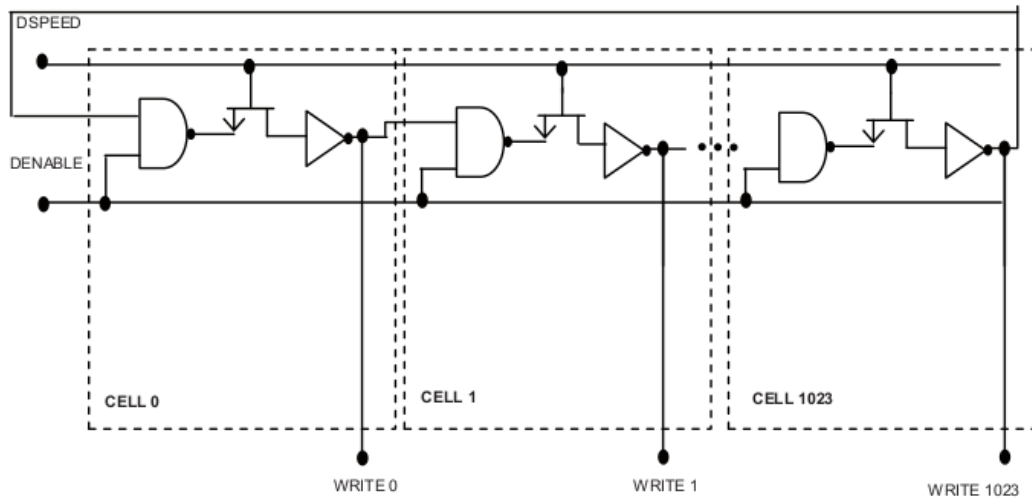


Figure 4.6: Simplified schematics of three out of 1024 double inverter blocks forming the domino wave circuit [28, 35].

The DRS4 board has some features, is powered with +5 V by USB port, and 50 Ω terminated TTL compatible input is implemented (LEMO 00 connector) for trigger purposes. An on-board discriminator with programmable level allows for self triggering on any of the four input channels. Figure 4.7 shows all components and final version of the DRS4 board [30].

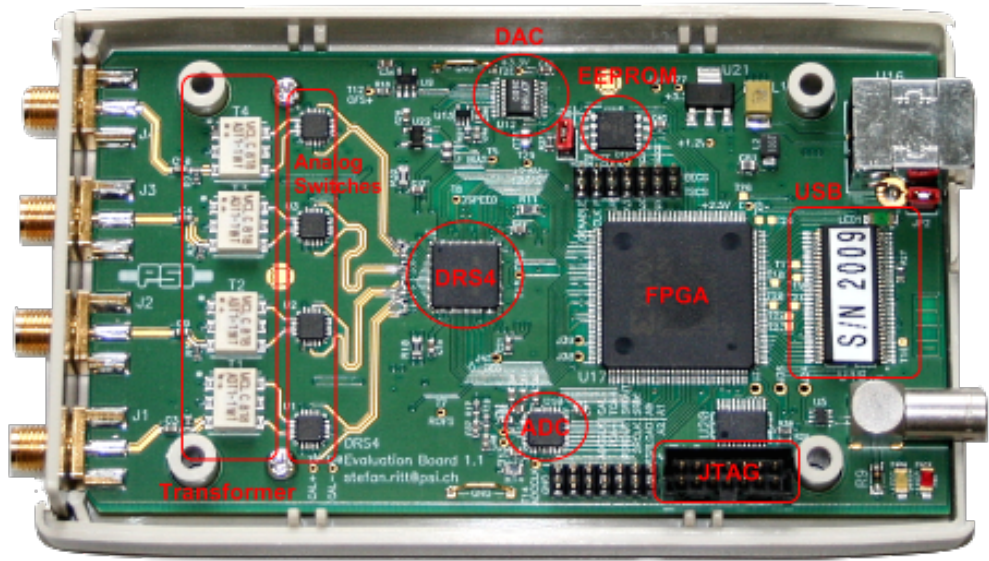


Figure 4.7: Picture of the DRS4 Evaluation Board with different components.

4.5 Verification Test of the Counter Box Heat Protection

The detector station is at the harsh environmental conditions the detector components, like photomultiplier, inside the box, must be protected by its environment to operate continuously as well as reliably. The SiPM device is installed on a board with a readout circuit and an ultra low noise 0.05 to 4 GHz Amplifier (Mini Circuits PSA-5454+) operating between $-40\text{ }^{\circ}\text{C}$ to $85\text{ }^{\circ}\text{C}$ and 390 mW dissipation power. These components, in particular the amplifier, generate heat inside the box so that heat can be restrained by using insulator material. Jakodur extruded polystyrene foam (XPS) insulator is a promising product thanks to its thermal conductivity, $0.034\text{ W}/(\text{m}\cdot\text{K})$ at $\lambda_D \leq 60\text{ mm}$. In order to be insensitive to the temperature differences, we need to estimate the thermal transmittance of the structure (seen in Figure. 4.8).

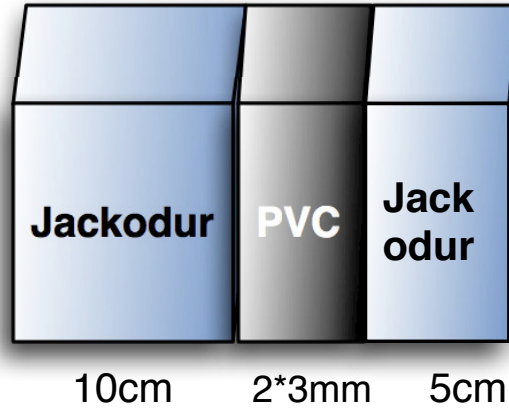


Figure 4.8: Schematic view of the structure.

The structure is consists of the three layers, one Jackodur box at 10 cm, one 2 sided 3mm PVC box which has $0.19 \text{ W/m}\cdot\text{K}$ thermal conductivity, and one Jackodur box at 5 cm thick. So as to evaluate the total thermal transmittance of the structure, the thermal resistance of the each section must be found. The thermal resistance formula is defined as thickness per conductivity. For the first section of the structure it is found that $(10 \text{ cm})/(0.034 \text{ W}\cdot(\text{m}\cdot\text{K})^{-1}) = 2.94 \text{ m}^2\cdot\text{K}/\text{W}$, for the second section it is evaluated that $(2\times 3 \text{ mm})/(0.19 \text{ W}\cdot(\text{m}\cdot\text{K})^{-1}) = 0.032 \text{ m}^2\cdot\text{K}/\text{W}$ and for the last section it is half of the first section, $1.47 \text{ m}^2\cdot\text{K}/\text{W}$. The total resistance is $4.44 \text{ m}^2\cdot\text{K}/\text{W}$ and the total thermal transmittance of the structure is $0.23 \text{ W}/\text{m}^2\cdot\text{K}$. Now one can estimate the supported temperature differences. The surface area of the box is $[2\times(20 \text{ cm} \times 30 \text{ cm}) + (100\times 3) \text{ cm}^2] = 0.15 \text{ cm}^2$, and if the generated power inside is 390 mW then the temperature inside the box, T_{hotter} can be found by the given formula, $\Phi = A\times U\times [T_{hotter}-T_{colder}]$, where Φ is the heat transfer in Watts, A is the area in square meters, U is the rate of the transfer of heat (in Watts) through one square meter, T_{hotter} and T_{colder} is the temperature (in Kelvin) inside and outside the box, respectively.

The supported temperature differences is given in equation. 4.8.

$$\begin{aligned}
 T_{hotter} - T_{colder} &= \frac{390 \times 10^{-3} W}{0.15 m^2 \times 0.23 \frac{W}{m^2 \times ^\circ K}} \\
 &= 11.3 \text{ } ^\circ K
 \end{aligned}
 \tag{4.8}$$

In the period of the data taking the external temperature varied from -25 °C to -5 °C that corresponds to an internal temperature between -13.7 °C to 6.3 °C [36]. Figure 4.9 shows the study about finding the optimum thickness of the used insulator to keep the heat inside the box.

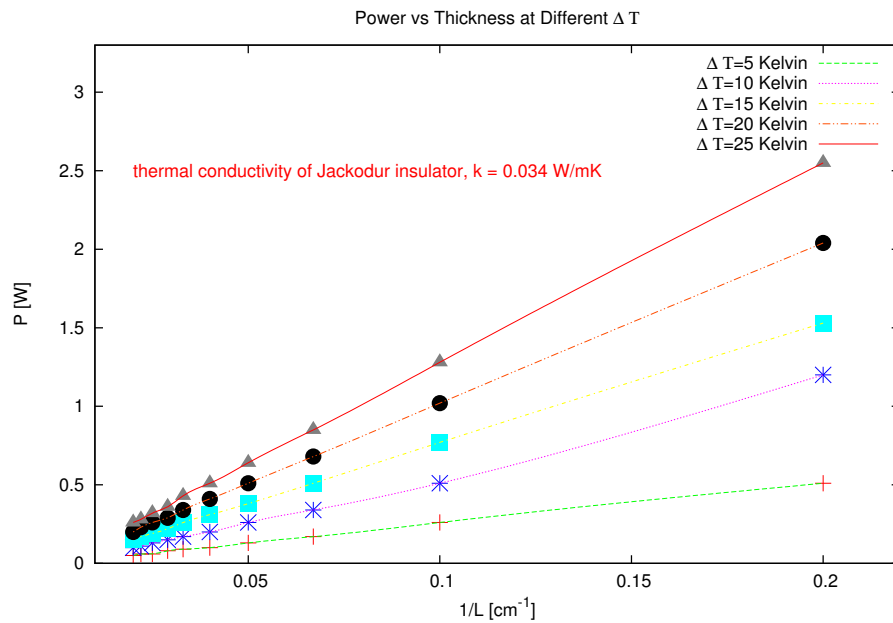


Figure 4.9: Produced power vs thickness of the shielding at different temperature differences.

The study shown in the Figure 4.10 shows the chill temperature variation in the data taking period. As we seen from the graph that the average chill temperature is around 0 °C.

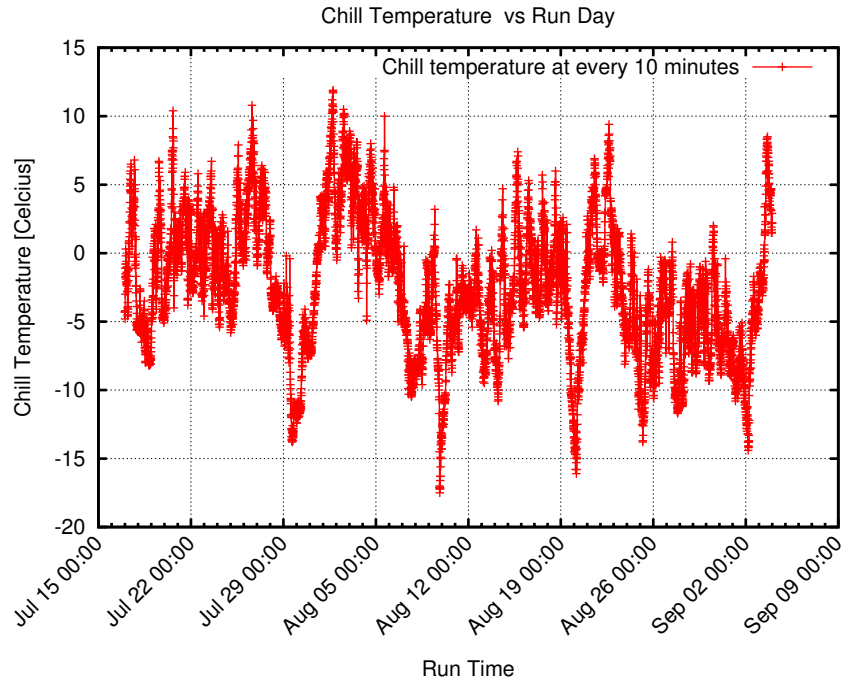


Figure 4.10: Chill temperature variation in the summer period.

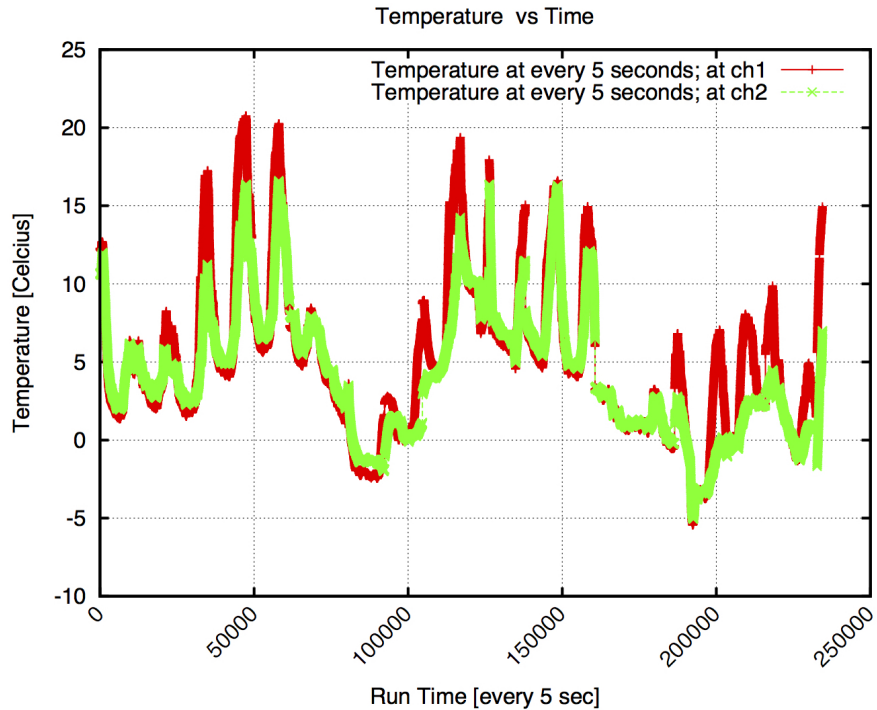


Figure 4.11: Internal variation of the temperature for each counter box in the summer period.

We found the temperature variation is $11\text{ }^{\circ}\text{K}$, in the equation 4.8, inside and outside of the counter box due to the insulators. Figure 4.11 shows the average

temperature is around 10 °C inside the counter boxes. But in the Figure 4.10 shows the outside temperature is about 0 °C, so means that the insulators were keep the heat inside and the estimation done in equation 4.8 is verified by experimentally.

4.6 DAQ & Event Selection Method

The Data Acquisition (DAQ) program is based on the setup described in section 4.2, and schematically shown in Figure 4.12. The DAQ program is based on a shell script that controls the two main C++ programs written by thesis author and Fabio Ferrarotto. One of the program is controlling the Arduino so that reads temperatures from the SiPM readout circuit and adjust the operating voltage in order to keep constant the gain of the SiPM. The other program manages the DRS4 which digitizes the signal detected by the SiPM and stores in root binary format for further analysis.

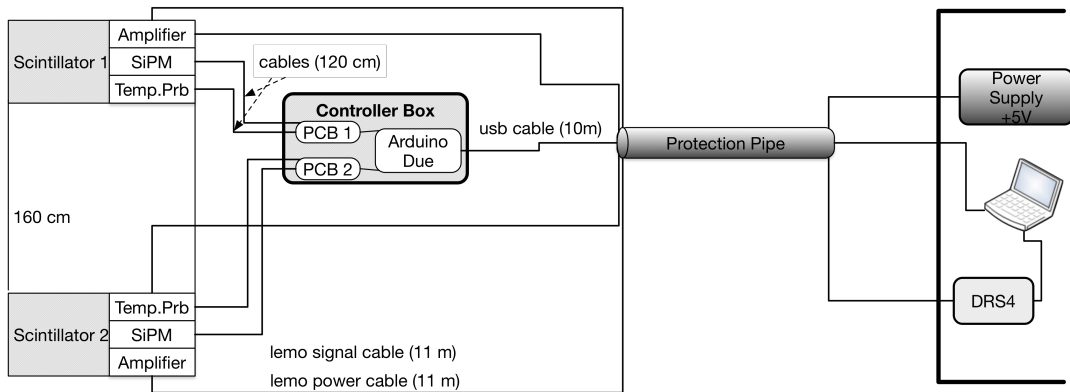


Figure 4.12: Data Acquisition at Sphinx (HFSJG).

The measured temperature as a function of time for each tile and adjusted operating voltage of the SiPMs in order to keep the gain constant for each board seen in Figure 4.13.

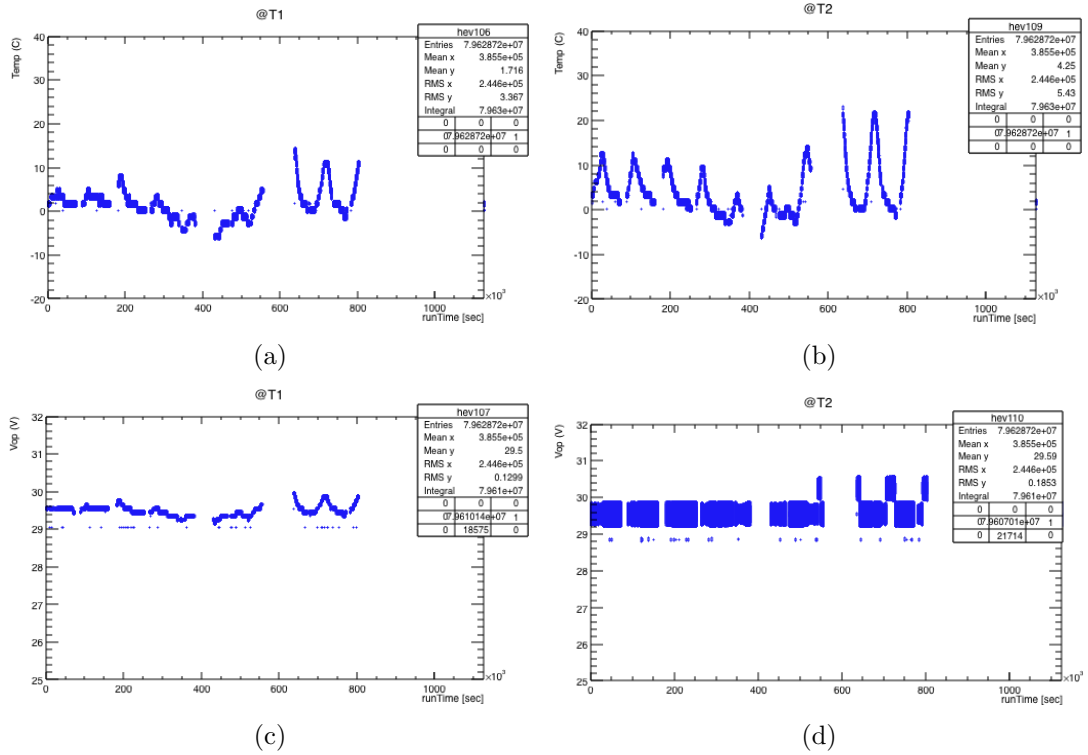


Figure 4.13: Temperature dependence as a function of time for Tile 1 (a) and Tile 2 (b) and adjusted operating voltage of the SiPMs in order to keep the gain constant for each board seen in (c) and (d), respectively.

The adjusted operating voltage as a function of temperature for Tile 1 and 2 is seen in Figure 4.14, respectively.

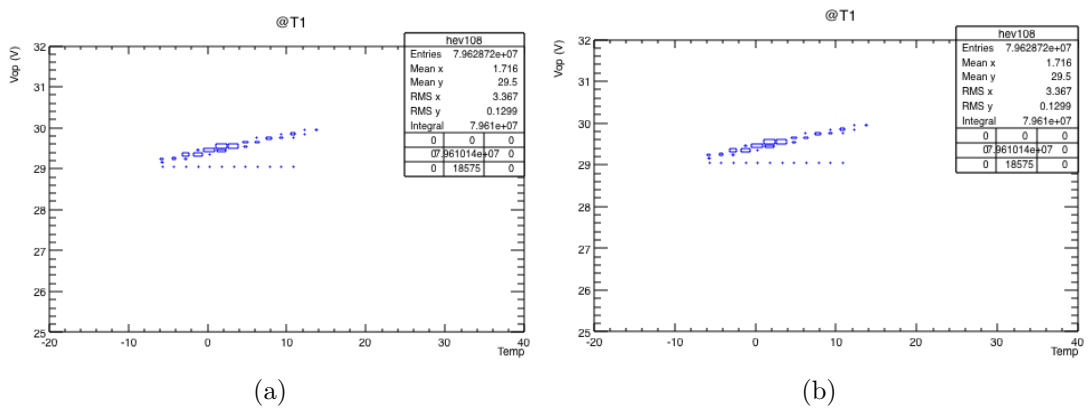


Figure 4.14: Operating voltage dependence as a function of temperature for Tile 1 (a) and Tile 2 (b), respectively.

The reconstruction program, is based on ROOT analysis package [37] using C++ programming language, represents a necessary tool for the analysis of the data.

Some quality parameters, provided by the reconstruction algorithm, can be used to improve the analyzing of the data sample. In any case the algorithm, presented in this section, takes into account the reconstruction errors. In section 5 the rate of atmospheric muons as a function of the zenith angle is computed. In the following a sequence of cuts on the reconstructed events, based on the quality parameters of the reconstruction program, are defined. The cuts intend to select a data set with a higher purity, in particular concerning the reconstruction of the zenith angle. Finally some quantities needed in the analysis code are defined and calculated. An algorithm optimized for high precision in measuring peak heights and rise times is needed to effectively use the peak height readout option. The algorithm described in this section is designed to analyze a continuous signal from a SiPM, composed of several different avalanche events occurring at random times. This signal will be referred to in the following as trace. The difficulties in achieving the goals listed above with existing algorithms lie in the following issues:

- *Changing baseline of the signal:* for high over-voltages, when the dark count rate increases substantially, peaks are often superimposed on each other with a time delay, so that the algorithm needs to identify and measure peaks starting at different heights.
- *Electrical noise:* when mainly first order peaks are measured, the signal to noise ratio can be as low as 5 in the worst cases (low over-voltages and high electronic noise), giving an uncertainty of 20% on the peak height if it is measured directly, leading to the need of a fitting algorithm.
- *Very different peak heights and widths:* these features change drastically with overvoltage and SiPM model, hence the code has to be able to adapt itself to measuring different features without the user having to vary and optimize the parameters for every measurement.

To identify the peaks starting and end points, a standard first derivative threshold method such as the one described in section 4.6.1 can be used. However, the analysis codes, based on the time domain, have serious difficulties in meeting the requirements listed above, the algorithm we developed uses multiple approaches. Because of the signal has standard delay (~ 200 ns) in the full time window (0-512 ns) it typically starts around 200 ns and ends around 250 ns depends on the recovery time. For the reason that the code first calculates the average of the baseline and its spread from from the baseline , σ_{RMS} , for first 30 ns corresponds 60 number of points, and assigning to it this value: $vBaseAvgN$ is thus known as the averaging window width. These two parameters lead to select a *safePoint* is defined as $vBaseAvgN + 3 \cdot \sigma_{RMS}$, is important to discriminate the a signal from electronic noise, for fitting the signal rise time (seen in Figure 4.15).

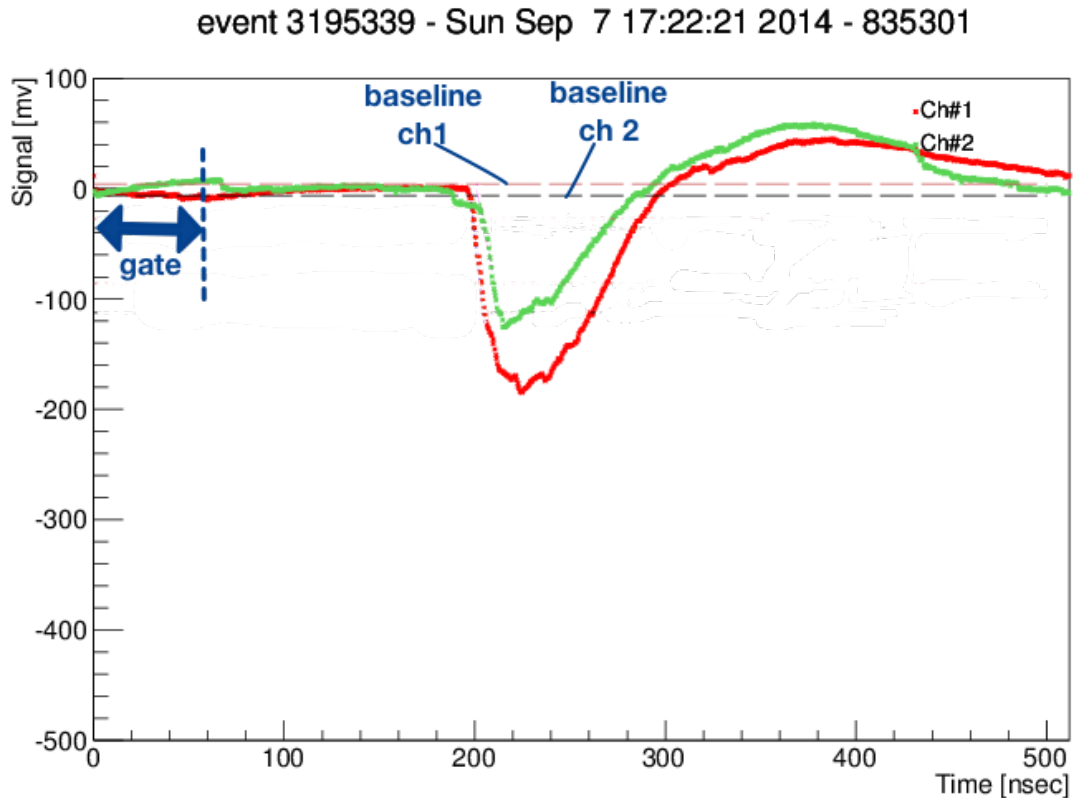


Figure 4.15: Determining the baseline of the SiPM signal.

The average of the baseline is around -1.172 mV and -1.385 mV for Tile 1

and Tile 2, respectively. The spread from the baseline means that the root mean squared (RMS) values, are depicted in Figure 4.16, is 0.06964 mV for the Tile 1 and is 0.1424 mV for the Tile 2. These information are automatically calculated by the function for each signal in the DAQ program in order to estimate the *safePoint*.

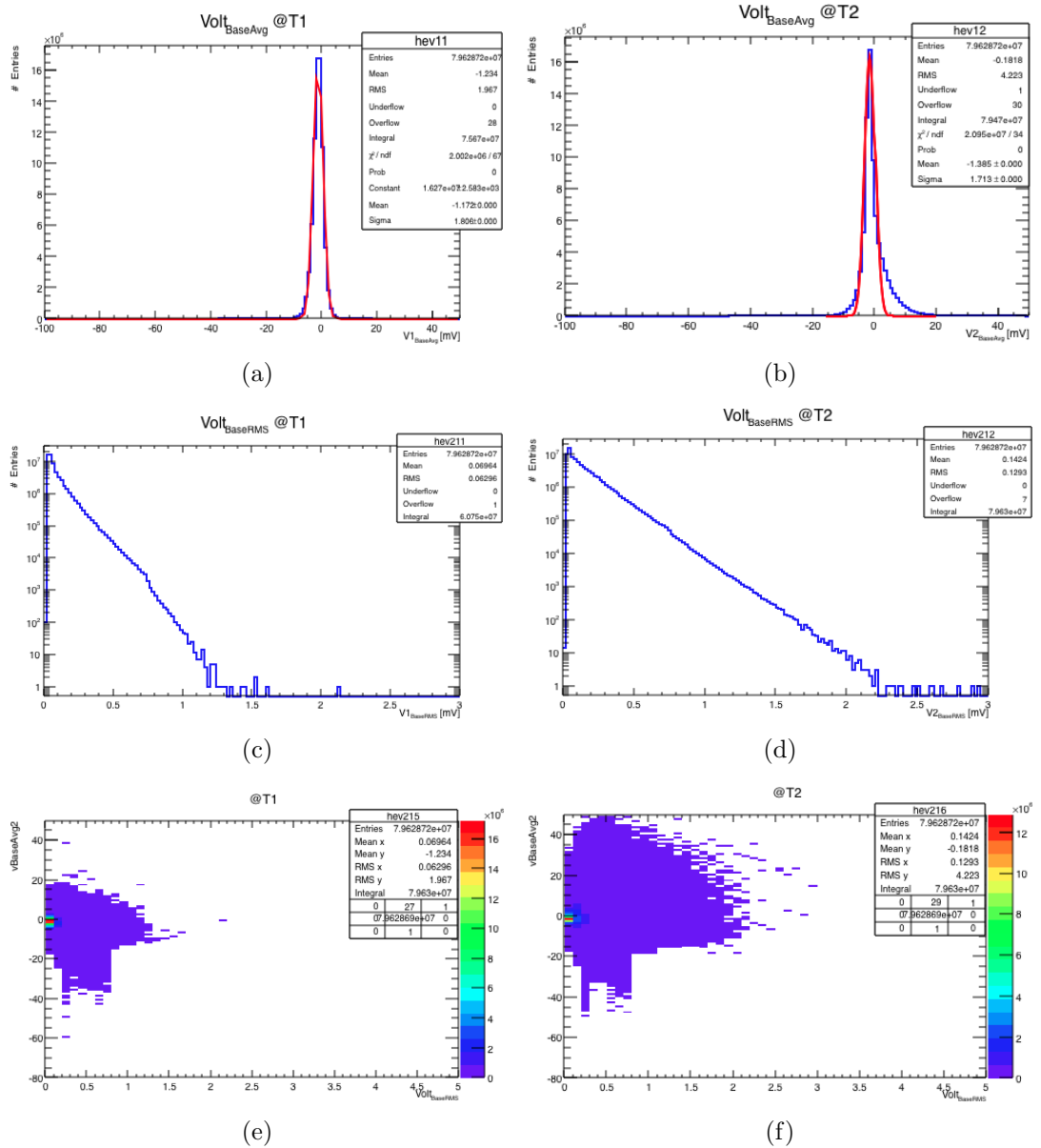


Figure 4.16: Average baseline and their RMS distributions of the SiPM signals for phase 6_2 is shown in (a) is for Tile 1 and in (b) is for Tile 2, respectively. Figure (c), and (d) depicts that the RMS of the distribution of the baseline for Tile 1 and Tile 2. Average of the baseline versus its RMS value is seen in the Figure (c) and (d), their 2D plots are depicted in (e) and (f).

In the analysis code, one of the functions searches full sampling window (0-512 ns) in order to find the peaks is above the threshold value and assign them into $nFindMin$. The signal produced by the cosmic rays has huge pulse height (bigger than 80 mV) at at the observation level (is 3800 m. above the sea level) are shown in Figure 4.17. After then the gate window, is around 150 to 280 ns, is determined around the most probable timing of the signal. These gates are used to select possible events, are called *candidateEventN*.

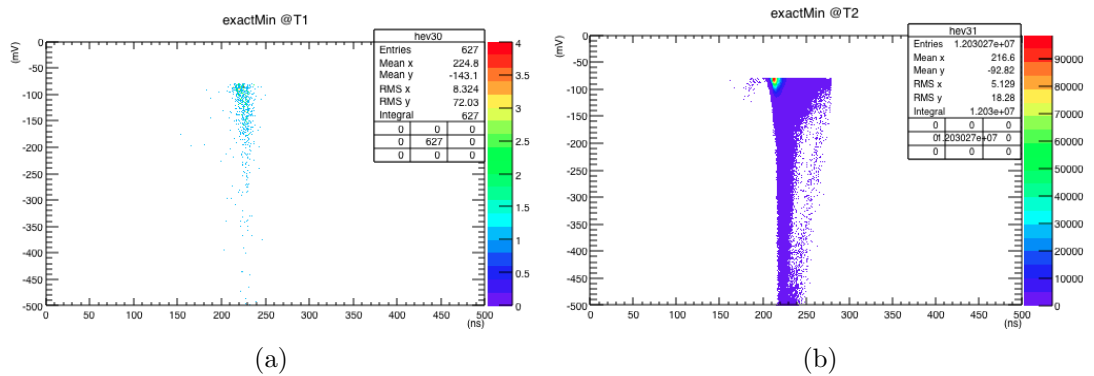


Figure 4.17: Peak distribution of the signals over sampling time window (a) is for Tile 1 and in (b) is for Tile 2, respectively.

4.6.1 Least Square Method

One of the functions was written in the analysis program in order to determine the the starting point of the signal which gives the timing information of the particle, so that a mathematical procedure can be applied for finding the best-fitting curve to a given set of points by minimizing the sum of the squares of the offsets ("the residuals") of the points from the curve. By fitting a set of N data points (x_i, y_i) to a straight-line model

$$y(x) = a + bx \quad (4.9)$$

where $y(x)$ and x are holding the voltage and time informations of the SiPM signal, respectively. The equation is generally called *least square method* or *linear regression*. Assuming that the uncertainty σ_i associated with each measurement y_i is known, and that the x_i 's (values of the dependent variable) are known exactly. The chi-square, χ^2 , function is used to measure how well the model agrees with the data.

$$\chi^2(a, b) = \sum_{i=0}^{N-1} \left[\frac{y_i - a - bx_i}{\sigma_i} \right]^2 \quad (4.10)$$

If the measurement errors are normally distributed, then this function will give maximum likelihood parameter estimations of a and b ; if the errors are not normally distributed, then the estimations are not maximum likelihood but may still be useful in a practical sense. In order to determine a and b the equation 4.10 is minimized. At its minimum, derivatives of $\chi^2(a, b)$ with respect to a, b become zero:

$$\begin{aligned} \frac{\partial \chi^2}{\partial a} &= -2 \cdot \sum_{i=0}^{N-1} \frac{y_i - a - bx_i}{\sigma_i^2} = 0 \\ \frac{\partial \chi^2}{\partial b} &= -2 \cdot \sum_{i=0}^{N-1} \frac{x_i \cdot (y_i - a - bx_i)}{\sigma_i^2} = 0 \end{aligned} \quad (4.11)$$

These conditions can be rewritten in a convenient form seen in the following sums:

$$\begin{aligned} S_\sigma &\cong \sum_{i=0}^{N-1} \frac{1}{\sigma_i^2} & S_x &\cong \sum_{i=0}^{N-1} \frac{x_i}{\sigma_i^2} & S_y &\cong \sum_{i=0}^{N-1} \frac{y_i}{\sigma_i^2} \\ S_{xx} &\cong \sum_{i=0}^{N-1} \frac{x_i^2}{\sigma_i^2} & S_{xy} &\cong \sum_{i=0}^{N-1} \frac{x_i y_i}{\sigma_i^2} \end{aligned} \quad (4.12)$$

the equation 4.11 can be rewritten by using the definitions in the equations 4.12;

$$\begin{aligned} aS_\sigma + bS_x &= S_y \\ aS_x + bS_{xx} &= S_{xy} \end{aligned} \quad (4.13)$$

The solution of these two equations in two unknowns is calculated as

$$\begin{aligned} \Delta &\cong S_\sigma S_{xx} - (S_x)^2 \\ a &= \frac{S_{xx}S_y - S_xS_{xy}}{\Delta} \\ b &= \frac{S_\sigma S_{xy} - S_xS_y}{\Delta} \end{aligned} \quad (4.14)$$

The solution for the best-fit model parameters a and b is given in the equation 4.14. The probable uncertainties in the estimation of a and b should also be estimated since obviously the measurement errors in the data must introduce some uncertainty in the determination of those parameters. Assuming the data are independent, then each contributes its own bit of uncertainty to the parameters. Consideration of propagation of errors shows that the variance σ_f^2 in the value of any function will be

$$\sigma_f^2 = \sum_{i=0}^{N-1} \sigma_i^2 \cdot \left(\frac{\partial f}{\partial y_i} \right)^2 \quad (4.15)$$

The derivatives of a and b with respect to y_i can be directly evaluated from the solution for the straight line equation:

$$\begin{aligned} \frac{\partial a}{\partial y_i} &= \frac{S_{xx} - S_x S_{x_i}}{\sigma_i^2 \cdot \Delta} \\ \frac{\partial b}{\partial y_i} &= \frac{S_\sigma S_x - S_{x_i}}{\sigma_i^2 \cdot \Delta} \end{aligned} \quad (4.16)$$

after the summation over the points as in the equation 4.15;

$$\begin{aligned}\sigma_a^2 &= \frac{S_{xx}}{\Delta} \\ \sigma_b^2 &= \frac{S_{xx}}{\Delta}\end{aligned}\tag{4.17}$$

which are called the variances in the estimates of a and b, respectively [38].

4.7 Time of Flight (TOF) Method

Time of Flight (TOF) is a method that measure the time that it takes for a particle to travel a distance of a medium. While a particle interact one of the scintillator counter as shown in Figure 4.18 that starts the time counter and it will be stopped when the particle interact with the second scintillator counter. The counter telescope (shown in Figure 4.18) is useful in experiments where a comparatively small number of wanted particles is to be counted in a large background of unwanted radiations. The resolving time of the coincidence logics, which follows the counters, is useful to eliminate the spurious counts recorded due to the random coincidence of counts in the individual detectors.

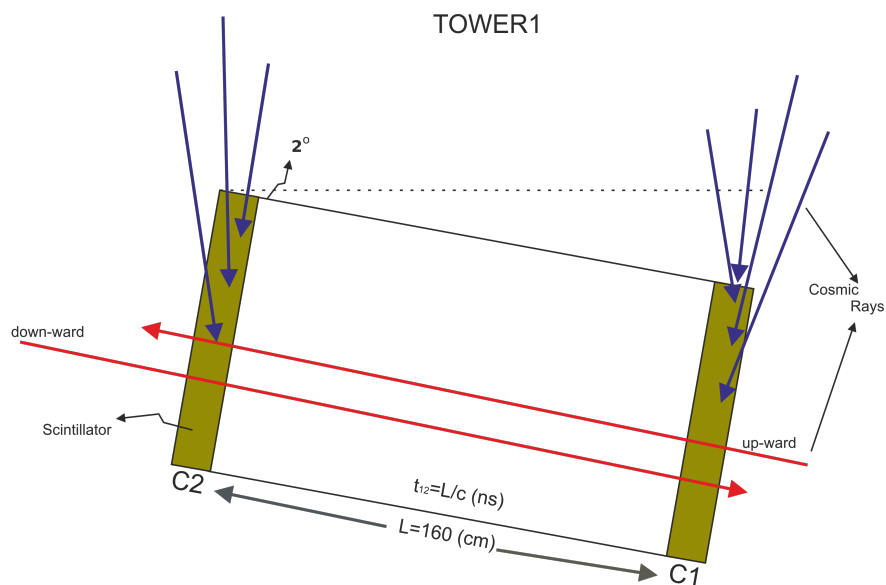


Figure 4.18: Schematic view of a tower.

The time of flight technique is also useful to discriminate the particle direction (*upward or downward*). If the particle hit the C1 firstly, then C2 means the particle is going to *up-ward* direction, the expected result of the time difference ($C1-C2$) should *negative*, if not, the particle is going to *down-ward* direction.

Figure 4.19 shows the method used in this thesis, which uses the algorithm mentioned in section 4.6.1 to calculate the time of flight. The signals are registered by using DRS4 board and then plotted by *ROOT* program to see the time difference between two counters. If the signal is greater than the threshold voltage and is inside the gate defined as mentioned above section, the analysis program firstly finds the absolute minimum of the signal is the 100% of the amplitude, then goes backward until *safePoint* then store the points starting forward direction just after the *safePoint*. After that it locates the 20% and 70% percents of the amplitude, are not fix number, are just below the threshold value and safe-Point, and fitting a line using these registered points, according to the method, which crosses the time axis. This point registered as t_0 . The difference of t_0 gives us the time of flight between two counters.

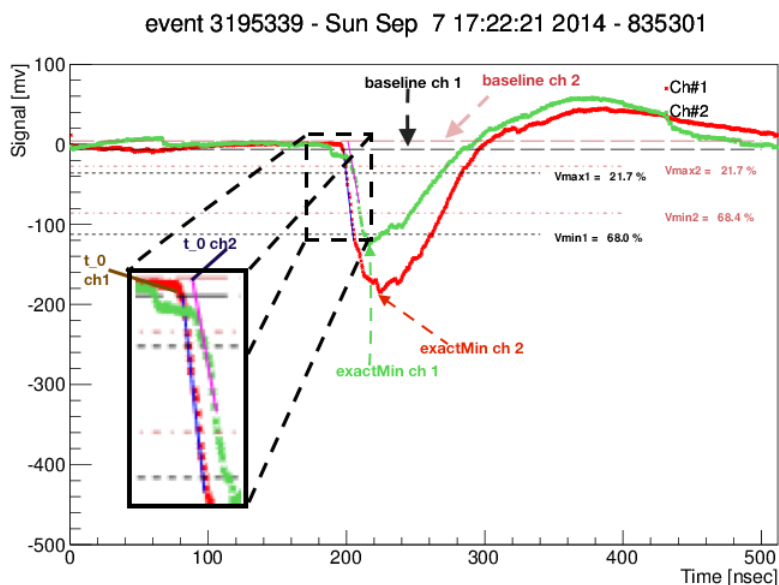


Figure 4.19: Time of flight (tof) calculation method used in this thesis. Tile separation is 160 cm. Magenta and blue lines indicate the fitted lines according to the method works forward direction from 20% until 70% of the amplitude.

Figure 4.19 shows the scheme of this algorithm which computed the TOF is about 5 ns for a *downward* going particle is shown in Figure 4.20.

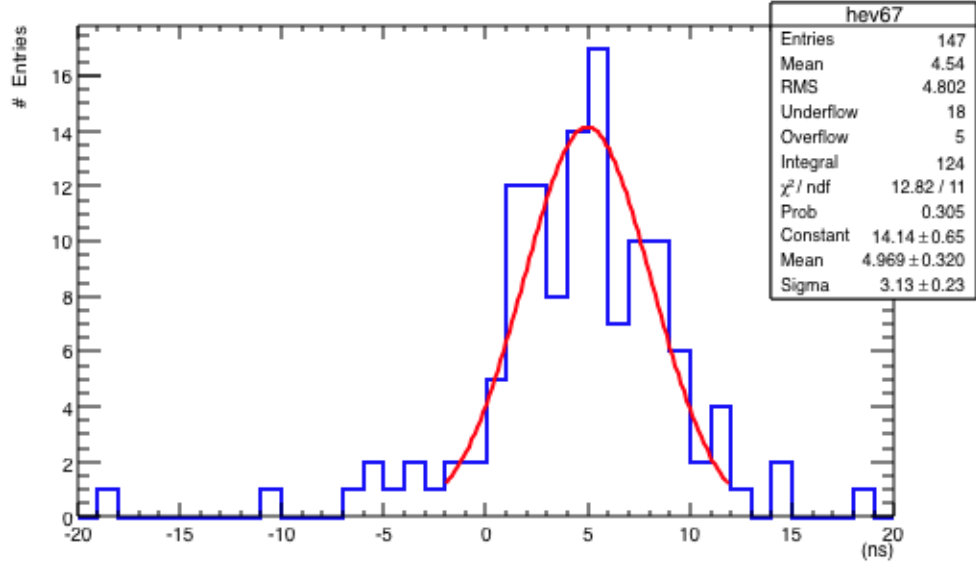


Figure 4.20: Time of Flight distribution for phase6. Tile separation is 160 cm. The peak around +5 ns is due to the particle coming from atmosphere side (downward direction).

4.8 Rise Time

A typical SiPM signal registered by the detector is seen in Figure 4.21. It has a final rise and fall times. Time taken by the signal to rise from LOW level to HIGH level is called the *rise time*, and the time taken by the signal to go from HIGH level to LOW level is called *fall time*. The nonlinearity of the signal typically takes place at the bottom and at the top of the signal so that the rise time is determined between the 10% and 90% percent of the amplitude of the signal. In order to be in a safe place we defined it between 20% and 70% percent of the amplitude of the signal. The outcomes are seen in the Figure 4.22.

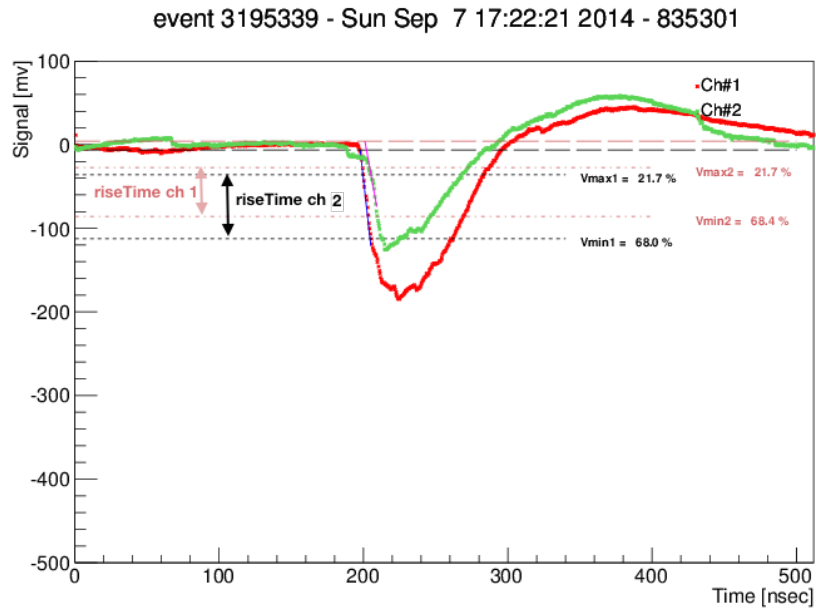


Figure 4.21: Signal shape of the rising time between the boundaries are 20% percent of the amplitude and 70% percent of the amplitude.

The mean of the gaussian fit on the rising time distribution shown in Figure 4.22 is $6.27 \pm 0.16 \text{ ns}$ and $4.979 \pm 0.165 \text{ ns}$ for Tile 1 and Tile 2, respectively.

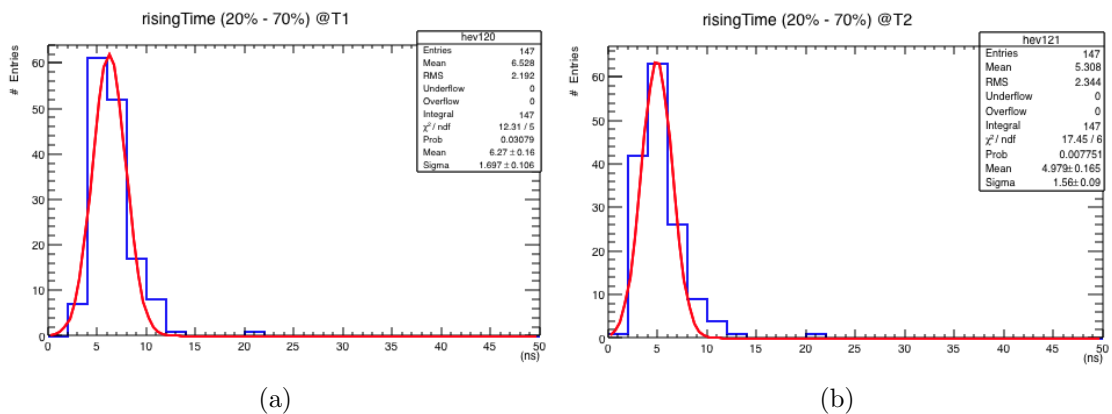


Figure 4.22: Rising time distribution of the signal is between 20% and 70% percent of the amplitude. (a) is for Tile 1 and in (b) is for Tile 2, respectively.

4.8.1 Robustness of the Fit

Goodness of fit, R^2 , is called correlation coefficient, is a quantity that gives the quality of a least square fitting to the data. If $R^2 = 1$ means the fit is perfect

but generally expected that this is close to 1. Figure 4.23 depicts that the R^2 distribution for all registered events for each tile. The value is 0.9752 and 0.9654 for Tile 1 and Tile 2, respectively.

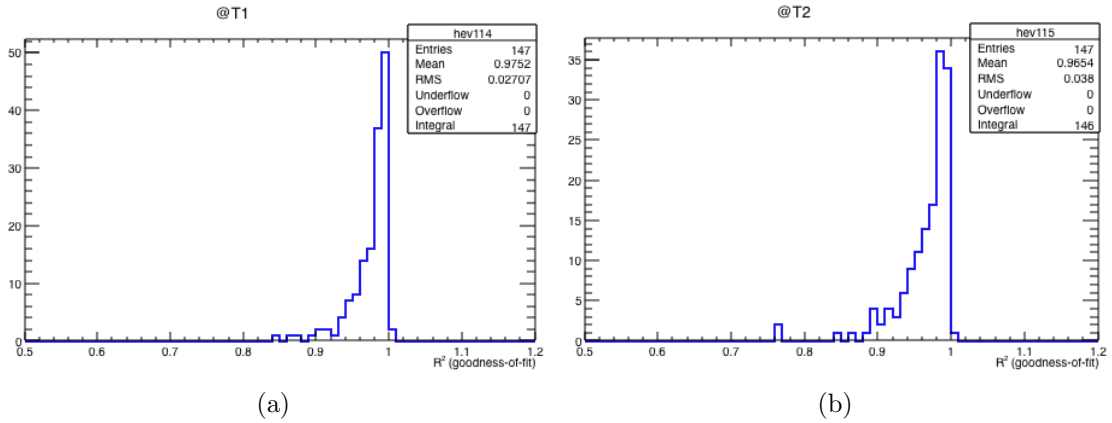


Figure 4.23: Goodness of Fit distribution of the signal is between 20% and 70% percent of the amplitude. (a) is for Tile 1 and in (b) is for Tile 2, respectively.

4.9 Multiplicity of the Signal

Multiplicity is defined as the number of hits the SiPMs had per event inside the full sampling window shown in Figure 4.24.

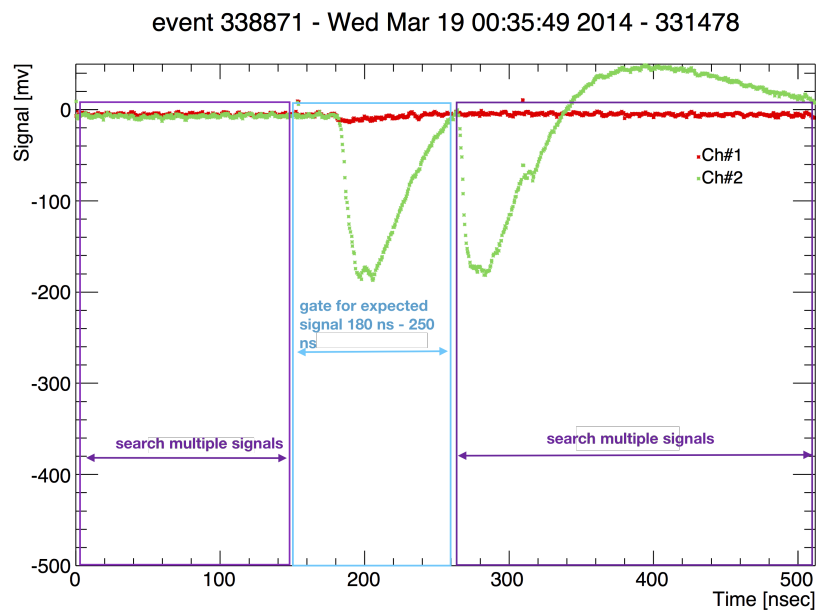


Figure 4.24: Multiplicity of registered SiPM signal in a full sampling window.

Since the detector is not limited to one characteristic of event, those particle would both be present, and point towards a nearby region, causing the total charge to be exceeded. Integrated charge for all signal where the baseline was removed from each signal are depicted in Figure 4.25 (a) and (b), the integrated charge for signal where the signals coming in the gated window and the baseline was removed from each signal are depicted in Figure 4.25 (c) and (d).

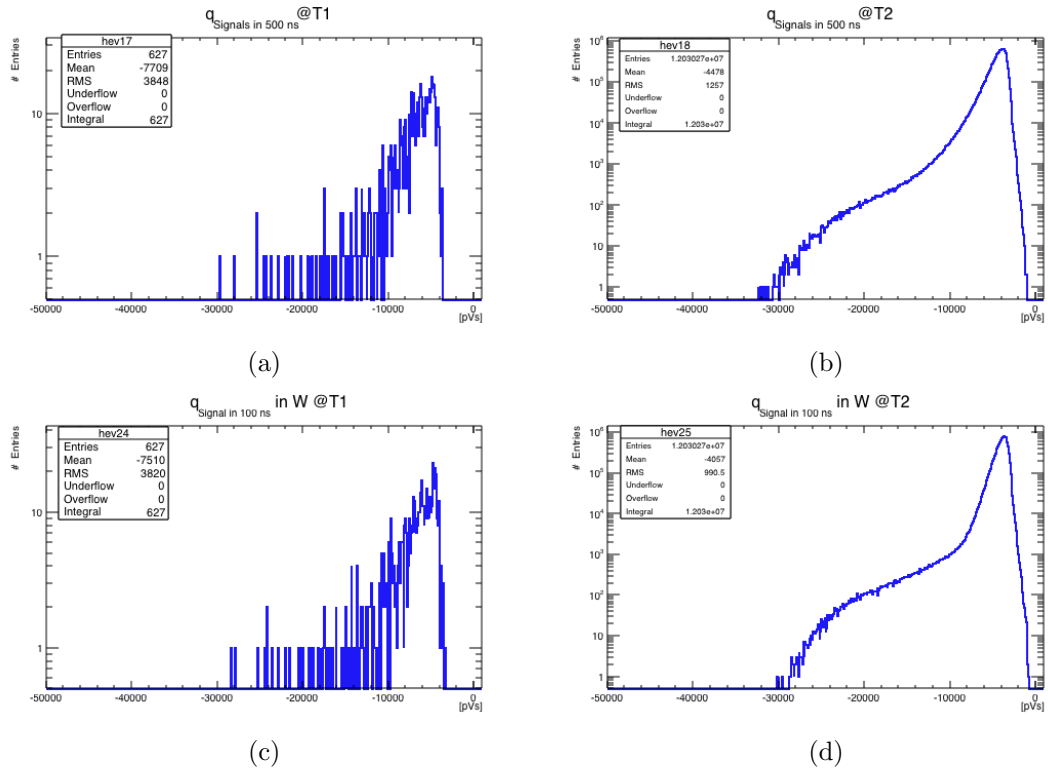


Figure 4.25: Integrated charge for all signal where the baseline was removed from each signal. (a) is for Tile 1 and in (b) is for Tile 2, respectively. The integrated charge for gated signals (c) is for Tile 1 and in (d) is for Tile 2, respectively.

The histograms shown in Figure 4.26 (c) and (d) has a main things. The first is only the number of hits found in that specific region which was the reason of the expected SiPM signal. Those values above 1 in Figure 4.26 (c) and (d) are due to more than one particle interacting with one cell. In the first type of event, a single cosmic ray (generally muon) points towards the region of the SiPMs. Cosmic rays are large collections of particles that have been reconstructed by the DAQ program. Because these cosmic rays contain many particles, the particles

will often separate, which could cause multiple hits in the region of the SiPM. From the Figure 4.24 shows next to it, one can see that there are two main hits in this particular event.

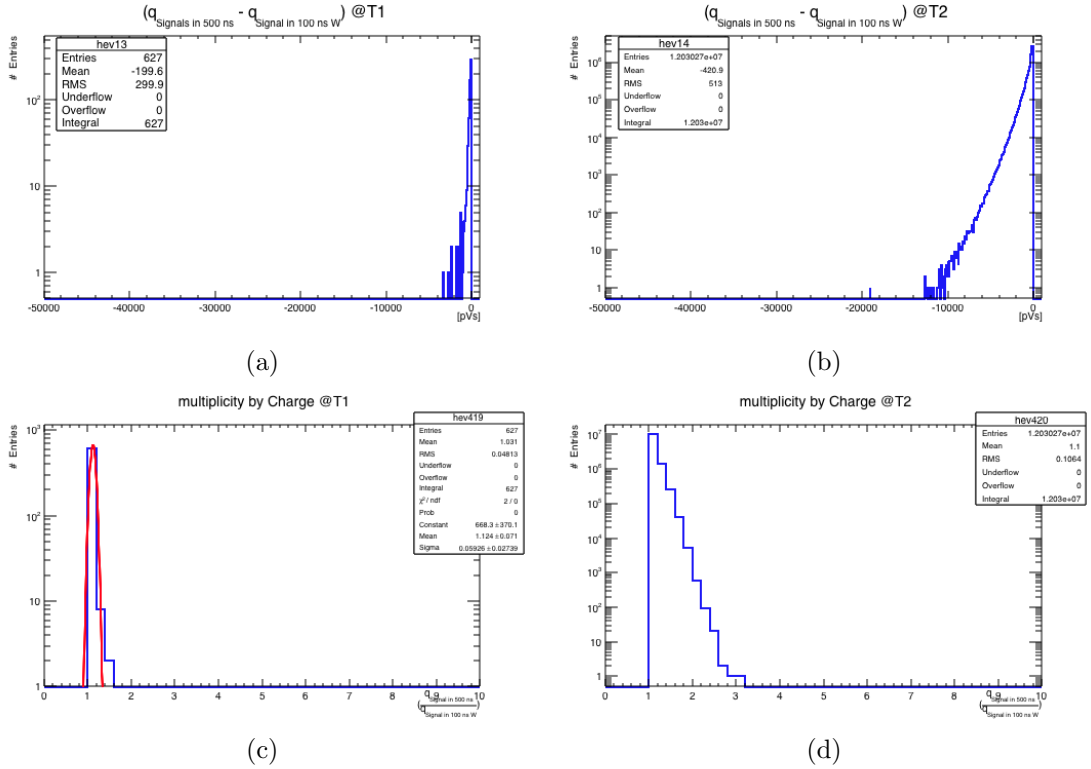


Figure 4.26: Multiplicity events in terms of integrated charge for the full sampling window. (a) for Tile 1 and (b) for Tile 2, and (c) and (d) give the multiplicity in terms of the number of events.

4.10 phi Dependence Measurement

Hence the detector prototype is depicted in Figure 4.1 is a part of a large array which will be observe the horizontal and upward going exceptional Ultra High Cosmic rays (UHECRs) and fever neutrino triggered air-showers may caused by the interactions in air or by higher energy tau air-showers originated by ν_τ skimming the Earth. In order to find a good place to observe an air-shower as its maximum developed altitude and directions should be studied at high altitude since the air density is so low the noise contribution is also few. In order to

increase the detection probability of the air shower initiated by tau-neutrino, the distance between the cosmic ray interaction and detection point (which is here our detector prototype) should be larger enough to develop a broad shower. This can be increase the detection probability up to three order of magnitude more than perpendicular showers; the detection of a maximal electromagnetic shower progression may intensify the signal by two-three order of magnitude regard to suppressed shower at sea level; the peculiar altitude-angle range (twenty km. height and $\sim 80^\circ - 90^\circ$ zenith angle) may smooth out at best the primary cosmic ray energy and composition [29]. To detect these range (the distance between cosmic ray interaction point and detection level) influence, the detector prototype, is installed on the terrace of the Sphinx Observatory Center, Jungfrauoch is 3800 m is above the sea level, is pointing valley 3.3° below the horizon and the distance between cosmic ray interaction point and the detector is around 14.5 km . The phase 4 data is taken for this circumstance and the setup is shown in Figure 4.27.

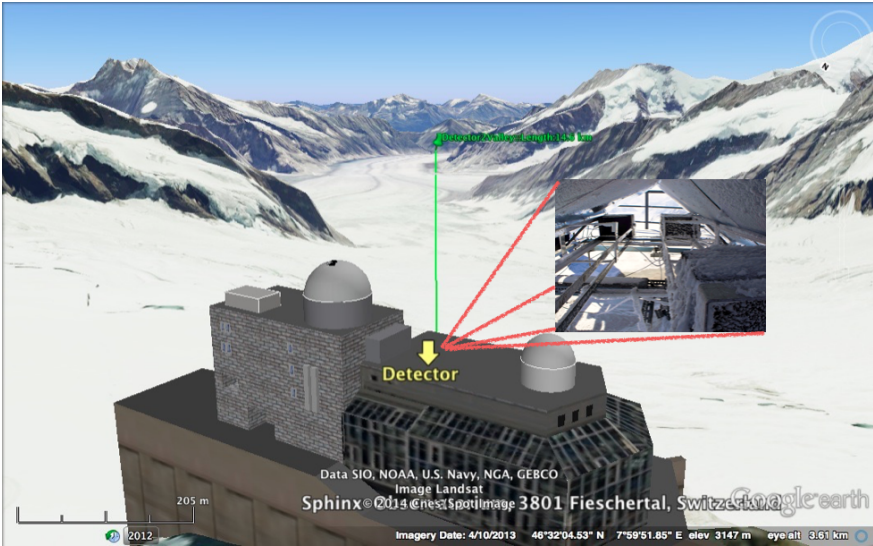


Figure 4.27: Detector station located at Sphinx Observatory Center. The green arrow, is pointing to the valley, is about 14.5 km from the mountain.

In order to understand reducing the distance between cosmic ray interaction point and observation point, the detector setup was rotated 56° from the previous (phase 4) setup and one side pointed to the Jungfraujoch and the other side pointed to the Monch mountains. The distance between detector to Jungfraujoch is 1.75 km and to Monch is 0.76 km. The setup is depicted in Figure 4.28 and the data taken in this setup is labelled as phase 5.



Figure 4.28: Detector station is located at Sphinx Observatory Center. (a) The magenta arrow, is pointing to the Jungfraujoch mountain, is about 1.76 km from the detector. (b) Turquoise color arrow is pointing to the Monch mountain is about 0.76 km from the detector.

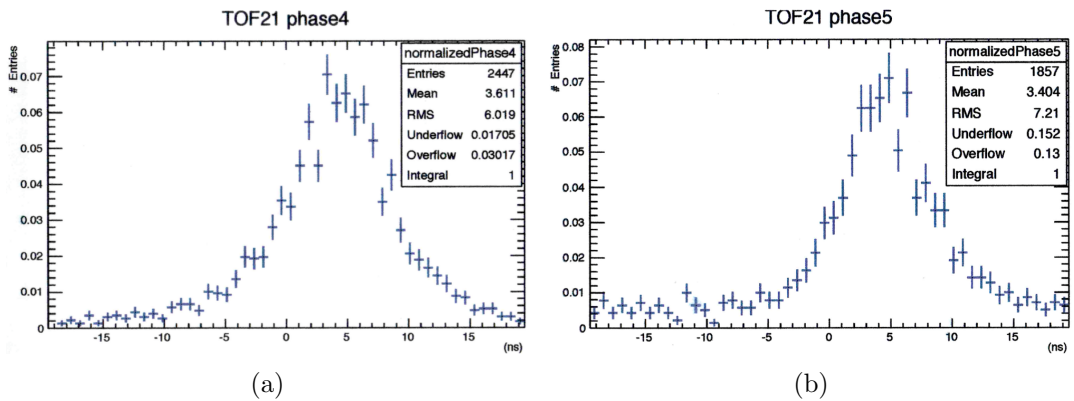


Figure 4.29: TOF distribution for phase 4 (a), and for phase 5 (b).

Φ , ϕ , dependence of the rate is clearly seen in Figure 4.30. The peaks around +5 ns is representing the downward going particles are from counter 1 to counter 2. The green gaussian peak shows exactly vertical TOF distribution of the cosmic rays, was measured in reference [39], is used to eliminate the contribution coming

from vertical direction. The excess above 2σ from the mean, that is between 7 to 15 ns is due to the almost parallel and some uncorrelated tracks coming from the open side (atmosphere side). The additional events within the 2σ below the mean, is between 3 to -6 ns, depicts that the events also coming partly from atmosphere plus from the shower produced while the particle emerging from valley. Because of the expected ratio is one for both measurement setup (phase 4 and phase 5) but there is an excess around -4 ns since the particle is more than downward direction (seen in Figure 4.30).

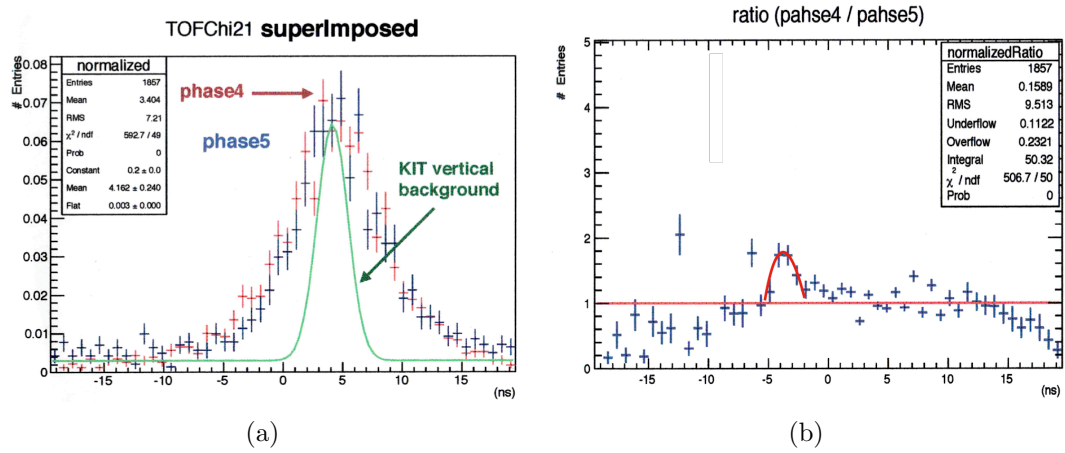


Figure 4.30: Rate distribution as a function of ϕ . (a) Red dagger represents the setup is pointing to the valley (14.5 km from the detector seen in Figure 4.27), blue dagger represents the setup is pointing to the Jungfrauoch-Monch direction (1.76 km from Jungfrauoch seen in Figure 4.28). The green gaussian fit shows that the TOF distribution exactly for vertical cosmic rays [39].

CHAPTER 5

SOLAR ACTIVITY

5.1 Theoretical Background

Climate is the pattern of variation in atmospheric temperature, pressure, humidity, wind and other meteorological parameters over a long period of time, ranging from months to thousands or millions of years. It is familiar that the Sun has a crucial role in the Earth's climate. In 1801, William Herschel proved that the price of the wheat was directly related to the Sunspot numbers based on his observations [40]. In 1993, Labitzke et al. found a correlation between 11-year variation of stratospheric pressure and solar activity [41]. Latest studies by Svensmark [42], recommended that climate fluctuation is leastway a certain degree of changed by the Earth's *cloud concentration* which is influenced by galactic cosmic rays. Galactic cosmic ray contain very high energetic particles, mainly protons that coming into our solar system from distant in the galaxy. A portion of them passes into the atmosphere of the Earth and collide to the atmospheric molecules and then initiates showers including the secondary particles. Galactic cosmic rays are the main source of creating ionization in the lower part of the atmosphere especially at 1 km to 35 km over the ground and 0 to 35 km over the ocean [43]. This fluctuation of ionization might likely effect the evolution of cloud concentration in that area and consequently change the atmospheric temperature. Recent findings also depict that cosmic ray intensity is effected by *Interplanetary Magnetic Fields* (IMF) and *Solar Plasma Wind* [44, 45], and the *atmospheric temperature* and *pressure* of the Earth [46, 47]. The number of Sunspots during a cycle is a good indicator of solar activities. Solar minimum shows that the period of time when the number of Sunspot are comparatively

small on the contrary solar maximum depicts the time period when Sunspot numbers are comparatively high. The Sunspot position relays on the solar activity in a cycle. Normally, they become visible in the mid latitudes during the solar maximum and Sunspots move closer to the equator as the Sun reaches to solar minimum. There can be a completely lack of Sunspots when solar minimum is seen. The Sunspot numbers are most decisive, since they are the visible proof of extreme magnetic events in the Sun. Latest researches done by NASA confirm that these magnetic fields are in the charge of the arising of solar flares and coronal mass ejections [48]. The coronal mass ejection is a enormous eruption of solar plasma wind and magnetic fields from the Sun into the space, which can effect the Earth and other planets in the solar system. The observation of 11-year solar cycle is because of the inverting of polarity of Sun's magnetic field. The short term variation of cosmic ray was carried out in the Reference [42], represented in Figure 5.1 .

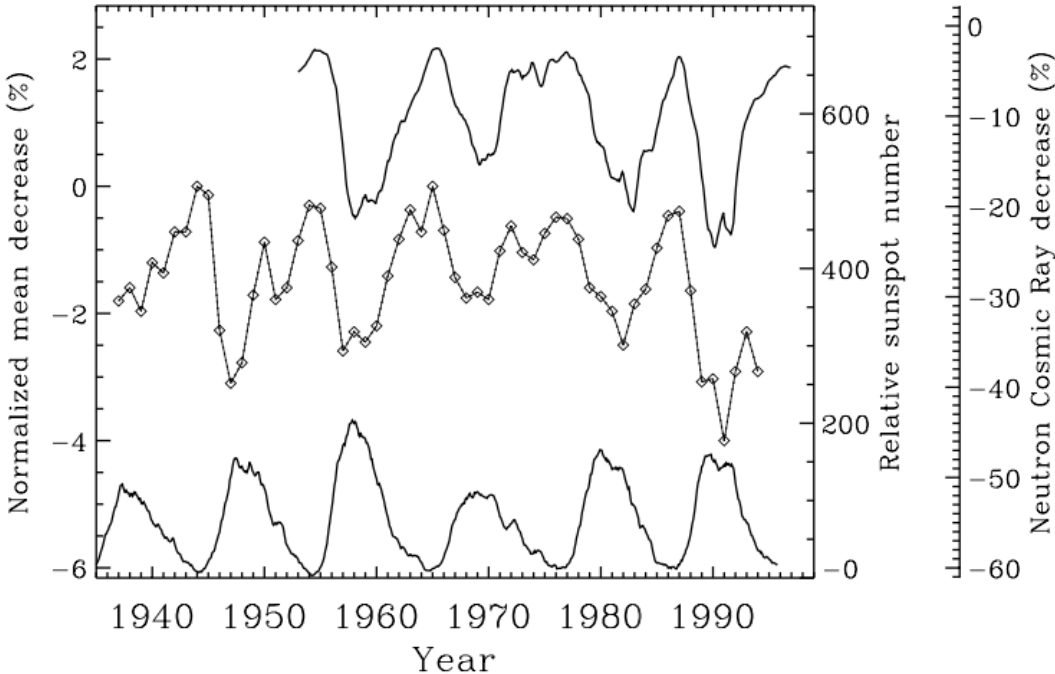


Figure 5.1: Bottom distribution is depicted for the relative Sunspot number. The middle distribution is for the annual average variation of the cosmic ray flux, and the top curve is cosmic ray flux from the neutron monitor in Climax [42].

The rate of cosmic rays at ground level varies in time due to changes in both the incident flux at the top of the atmosphere and changes in atmospheric conditions [40, 49]. Variations in the primary spectrum are thought to be due in part to the indirect effect of the magnetospheric distortions caused by solar activity, and these "Forbush" variations can occur on a timescale of hours and days and be up to about 20% in magnitude. Separately, the evolution of cosmic ray showers in the atmosphere is affected by gas density variations, which are in turn related to measurable pressures and temperatures at various altitudes, as has been discussed in the literature for decades. Incident protons between roughly 15 and 20 km altitude initiate collisions with nuclei that produce primarily pions and spallation nuclear fragments. When this occurs at comparatively higher altitude and at lower air density, the pions are more likely to decay to muons rather than to interact again to create lower energy pions and nucleonic secondaries. Higher average energy decay muons, though fewer in number, are less likely to suffer enough ionization energy loss to stop and decay before reaching the ground. On the other hand, if the pionic interactions take place at comparatively lower height and higher air density, pions are more likely to interact again before decaying, ultimately producing a larger number of lower energy muons closer to the ground. The interplay of these processes leads to the well-known broad momentum spread of muons and other particles at ground level [50], but also to correlations of particle rates and atmospheric conditions. The air pressure and rate of the cosmic ray are anti-correlated, since denser air causes more ionization energy loss to occur, and therefore earlier stoppage of muons. Also, for a given temperature lapse rate, denser air at ground level means a higher altitude at which muons are formed, which in turn gives muons more chance to decay before arriving at the surface. The temperature of the atmosphere at the mean muon production altitude may be supposed to affect the muon rate in the following way: if the air is warmer it is less dense (at fixed pressure), so the pions have greater

probability of decaying to muons before they interact again. This would favor creation of higher average energy muons that reach ground level, and also lead to larger numbers that penetrate deep underground. A positive correlation with temperature is seen underground, for instance in References [51, 52]. But the expected effect at ground level is less definite, since lower average energy muons created from pions in a denser atmosphere may be more copious in number at the surface, formed together with fewer higher energy muons. Indeed the temperature correlation was too small to measure in Reference [53] for vertically incident muons in a sea-level telescope of counters. The goal of this study summarized in this chapter is to determine experimentally the correlation included in various atmospheric parameters and the rate of the ground-level cosmic ray. Such type of measurements are performed at high mountain altitude (Jungfrauoch mountain, Switzerland). The advantages of high mountain altitude are connected with the possibility to register precisely secondary cosmic ray particles as compared to lower altitude observation levels. The properties of the atmosphere that we examined in relation to the particle rates were as follows. First, the used the station-level air pressure, P , measured at the site of the detector via MeteoSwiss weather station [54], second the temperature data is taken simultaneously by the DS18B20 temperature sensor mounted on the readout circuit of the prototype detector.

5.2 Effect of Atmospheric Pressure

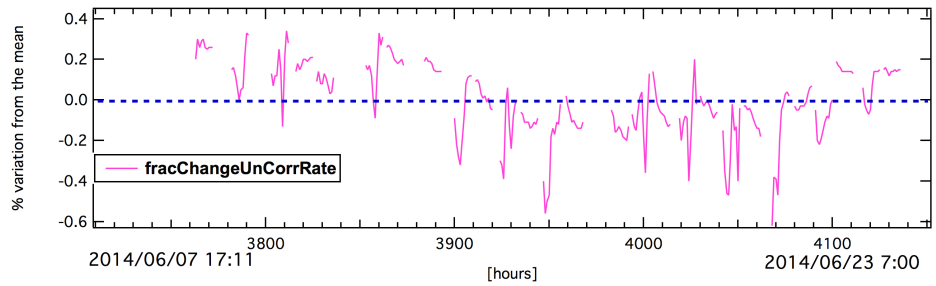
Atmospheric pressure at any altitude is relatively depended on the density of air, since it is the inverse of air temperature, and it is the density that eventually control the development of cosmic ray showers. The consequences were quite good, but, when looking for the separate correlations with the given parameters. To understand the confidence in the cosmic rays rate, the subsequent linear re-

gression model is used. In the next section, one month span of time during which the data did not show radical fluctuations in rate, Φ was defined by observation of the data from a 1 month long run. For that span of time the average values of all variables in the data were established (bracketed symbols). The expression for relating the variables was taken to be

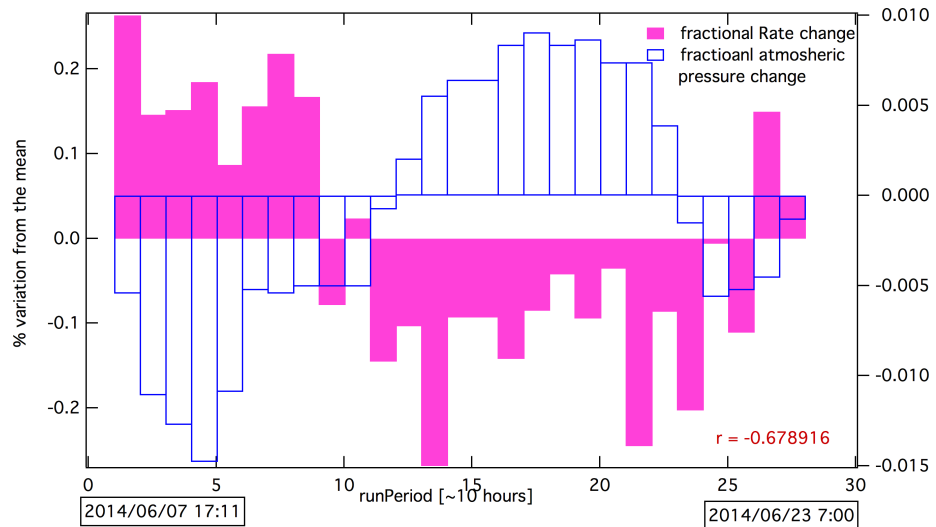
$$\frac{\Phi - \langle \Phi \rangle}{\langle \Phi \rangle} = \alpha \left(\frac{P - \langle P \rangle}{\langle P \rangle} \right) + \gamma \left(\frac{T - \langle T \rangle}{\langle T \rangle} \right) \quad (5.1)$$

where α is called as "total barometric correlation coefficient" while the γ is the temperature correlation coefficient is constant. They are unit-less coefficients of fractional change. In this study the data taken by new generation of cosmic ray detectors, seen in Figure 4.1, such as new readout circuit with SiPM described in chapter 4. The experiment ran from June 6, 2014 to June 23, 2014, with some gaps between the runs. This section is mainly focused to the understanding the effects of atmospheric and solar parameters on the variation of cosmic ray particles arrived at the surface of the Earth. The majority of cosmic rays reaching the Earth atmosphere come from outside the galaxy. This means that a galactic cosmic ray particle is required to propagate through the heliosphere as well as the Earth atmosphere by the time it reaches the surface of the Earth. This causes the cosmic particles to contact with both heliosphere disturbances in Earth's atmosphere during their flight. In order to understand the particle information such as its inherent acceleration mechanism, information about its source and transient modulation effects posed by the Sun, it is necessary to know both terrestrial and Earth atmospheric influences precisely. The barometric effects are the most effecting variable on the rate of secondary particle [55],. Hence, first thing to do that it is mandatory to precisely determine the barometric coefficient for a cosmic detector to flatten the solar variation influences. Thus the fluctuation on the rate of cosmic ray can be originated by the major atmospheric

variables; first one is the atmospheric temperature and second one is the atmospheric pressure [55]. While a cosmic ray traverses through the atmosphere, the distance through the atmosphere from the position of creation to the detection is needed to determine the effects of atmospheric temperature. However, the atmospheric pressure at the detection point is enough to examine the barometric effects because the density of air mostly is larger or near to the surface of the Earth. Figure 5.2 shows the resultant fractional rate variation of cosmic rays and atmospheric pressure over the entire data period. Because of the measured



(a)

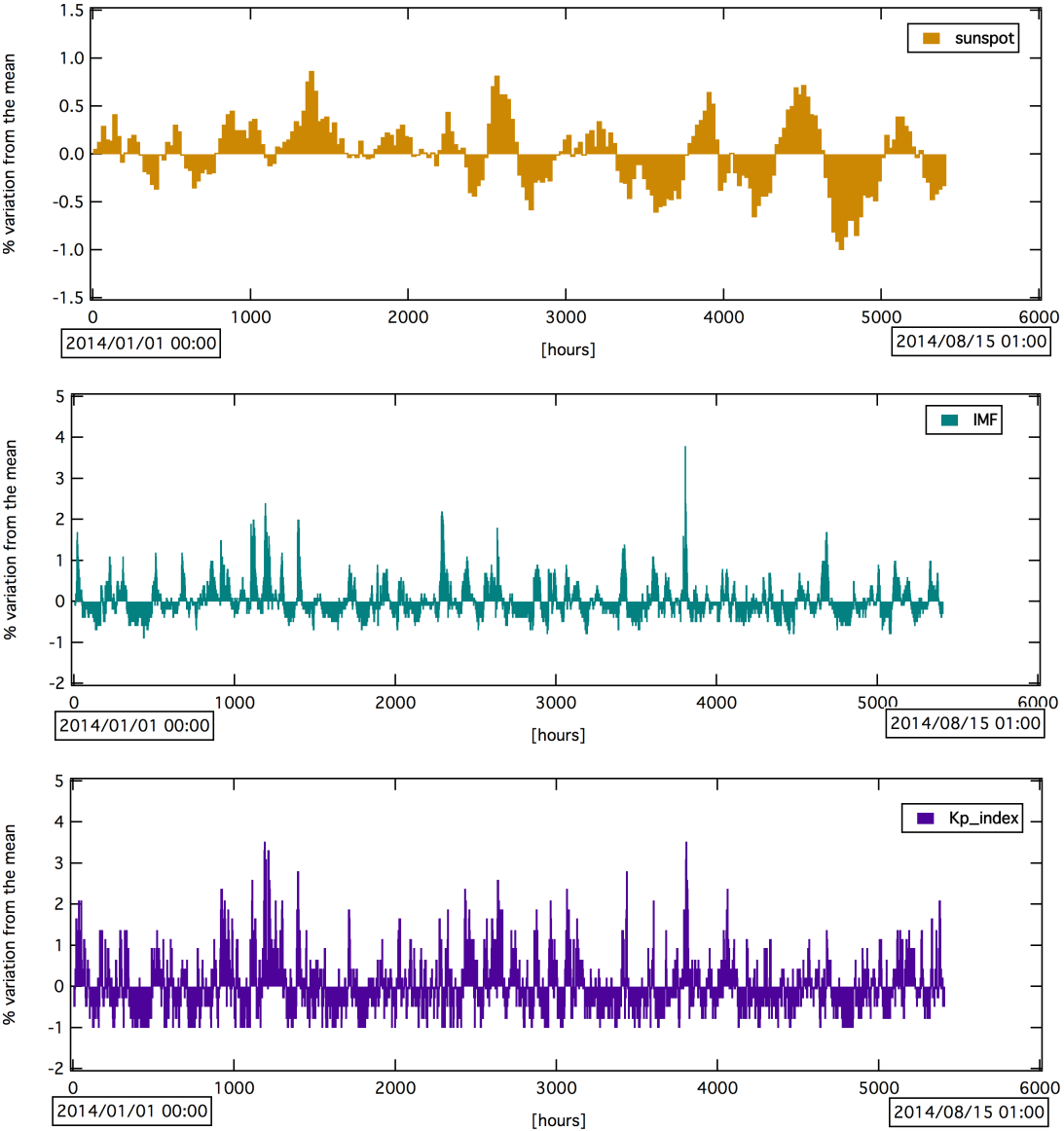


(b)

Figure 5.2: (a) Percentage variation of cosmic ray flux (pink) in terms of hours where time gaps between two sequenced run, (b) variation of the pressure data (blue empty bars) taken by Meteoswiss weather station and variation of the cosmic ray flux (pink) in terms of each run period for measurements at Sphinx Observatory Center.

counts reliance on pressure is higher than that for the prototype detector, there is

a -0.68 correlation coefficient between atmospheric pressure and counts from the detector in that period is shown in Figure 5.2. In order to remove this pressure dependence (to see correlations with other atmospheric and solar parameters), initially the barometric coefficient corresponding to the measurements should be calculated. Figure 5.3 shows the variation of solar parameters in the year of 2014.



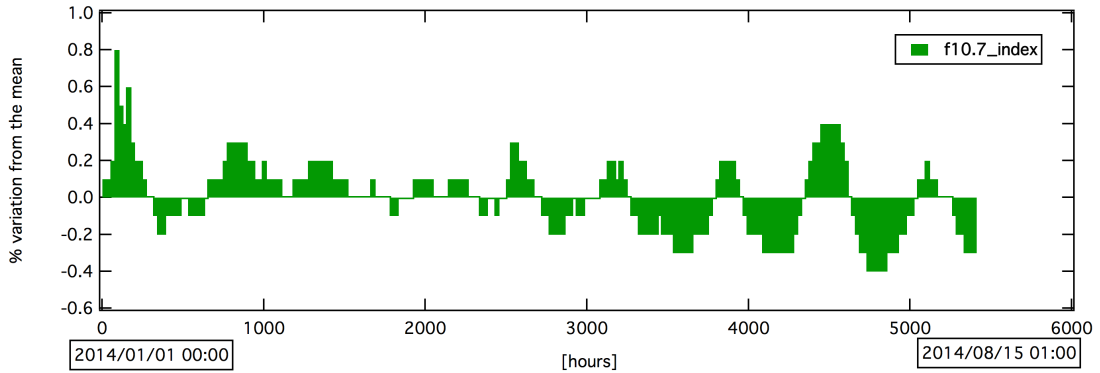
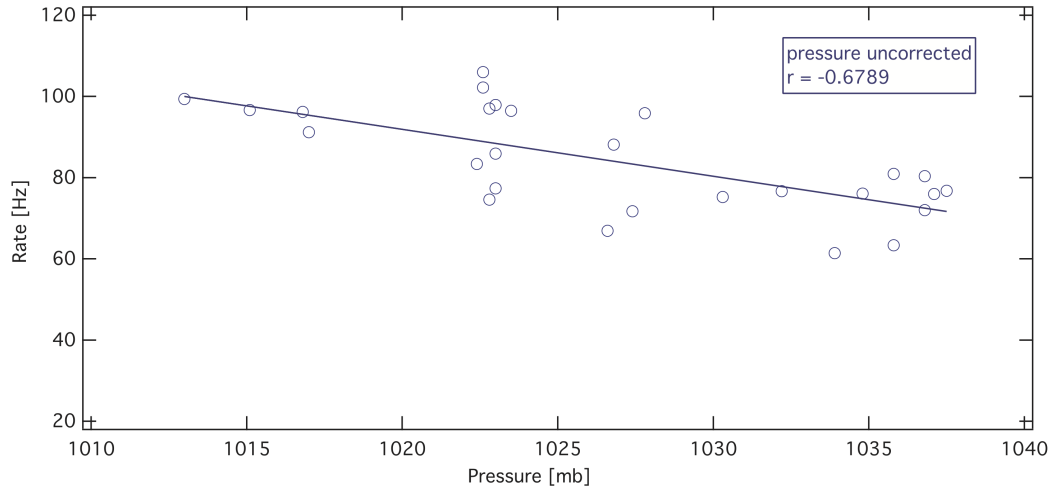


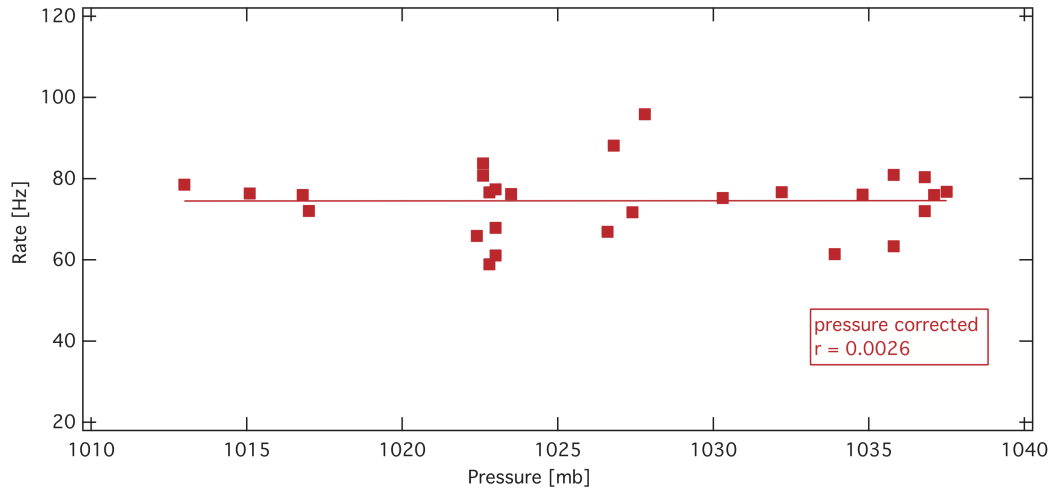
Figure 5.3: Variation of solar parameters in the year of 2014. The highlighted regions are time periods selected for calculating barometric coefficient for the detector. Data was obtained from OMNI solar weather station [56], the data taking period in terms of hours is corresponding between 3763 to 4136 from the beginning of 2014.

The variation of five solar parameters: IMF, plasma speed, Kp index, solar index F10.7 and Sunspot number were analyzed in order to obtain the low solar activity period. Among these, IMF and plasma speed are two significant parameters that highly influence the rate of the cosmic rays [45, 57]. The data sampling window is starting from 3763 hours behind the beginning of the year up to 4136 hours. The data taken in that region is used to estimate the α barometric coefficient value which was evaluated to be $(-0.11 \pm 0.01)\%/mb$.

The correlation of cosmic ray rate with atmospheric pressure is seen in Figure 5.4, where (a) represents the uncorrected rate with pressure, and (b) shows the pressure corrected rate. The visual appearance of the fit in the range is good. It is noted that there is an anti-correlation of pressure with the rate of cosmic ray, since α is large and negative. The temperature data is also taken the same data taking period by DS18B20 sensors mounted on the SiPM readout board.



(a)



(b)

Figure 5.4: Dependence of rate on atmospheric pressure measured by the detector where the pressure data taken from Meteoswiss weather station [54].

The correlation of atmospheric temperature on the uncorrected rate of cosmic ray is seen in Figure 5.5, is notably positive value for γ that is consistent with the literature Table IV given in reference [58].

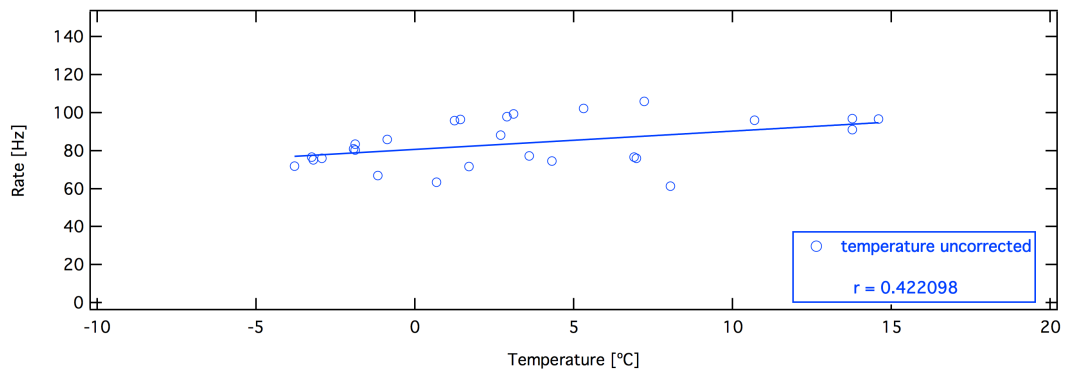
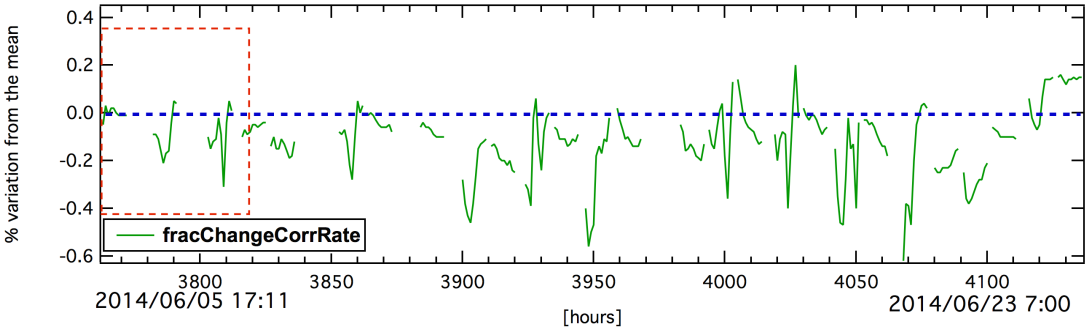


Figure 5.5: Dependence of rate on atmospheric temperature measured by the detector.

5.3 Correlation with Space Weather

"Sunspots" shown as dark spots on the surface of the Sun. Temperatures in the dark points of Sunspots fall about 3700 K (contrast to 5700 K for the surrounding photosphere). They generally last for several days, however very large ones may exist for several weeks. Sunspots are magnetic belts on the Sun with magnetic field strengths thousands of times stronger than the Earth's magnetic field. Sunspots generally move in groups with two sets of spots. One set will have positive or north magnetic field while the other set will have negative or south magnetic field. The field is powerful in the darker sides of the Sunspots. The "*F10.7 index*" is a measure of the noise level produced by the Sun at a wavelength of 10.7 cm at the Earth's orbit. The radio emission from the Sun at a wavelength of 10.7 centimeters (generally called "the 10 cm flux") has been found to correlate well with the Sunspot number. Sunspot number is defined from counts of the number of individual Sunspots as well as the number of Sunspot groups and must be reduced to a standard scale taking into account the differences in equipment and techniques between observatories. The "*Kp index*" quantifies the disturbances in the Earth's magnetic field from ground level. K perturbation arises from solar particle radiation that is derived from an influx of cosmic rays. There is an anti-correlation exists between rate of the cosmic ray and Kp index. The "*solar*

wind” is the supersonic outflow into interplanetary space of plasma from the Sun’s corona, the region of the solar atmosphere beginning about 4000 km above the Sun’s visible surface and extending several solar radii into space. The solar wind changes in density, velocity, temperature, and magnetic field properties, with the solar cycle, heliographic latitude, heliocentric distance, and rotational period. It also varies in response to shocks, waves, and turbulence that perturb the interplanetary flow. The *”interplanetary magnetic field”* (IMF) is a part of the Earth’s magnetic field that is carried into interplanetary space by the solar wind [59, 60]. Figure 5.6 shows the variation of observed muon flux during a higher solar activity period. On the y-axis is the percentage variation of muon counts, interplanetary magnetic field (IMF), solar proton density, solar plasma speed and plasma pressure and on the x-axis is the number of hours in a day. The higher solar activity time period is indicated by the enhancement of solar parameters, especially the IMF and plasma speed. Moreover to the IMF and plasma speed are two significant parameters that highly impact the variation of galactic cosmic rays with energies below 15 GeV [45, 57, 61].



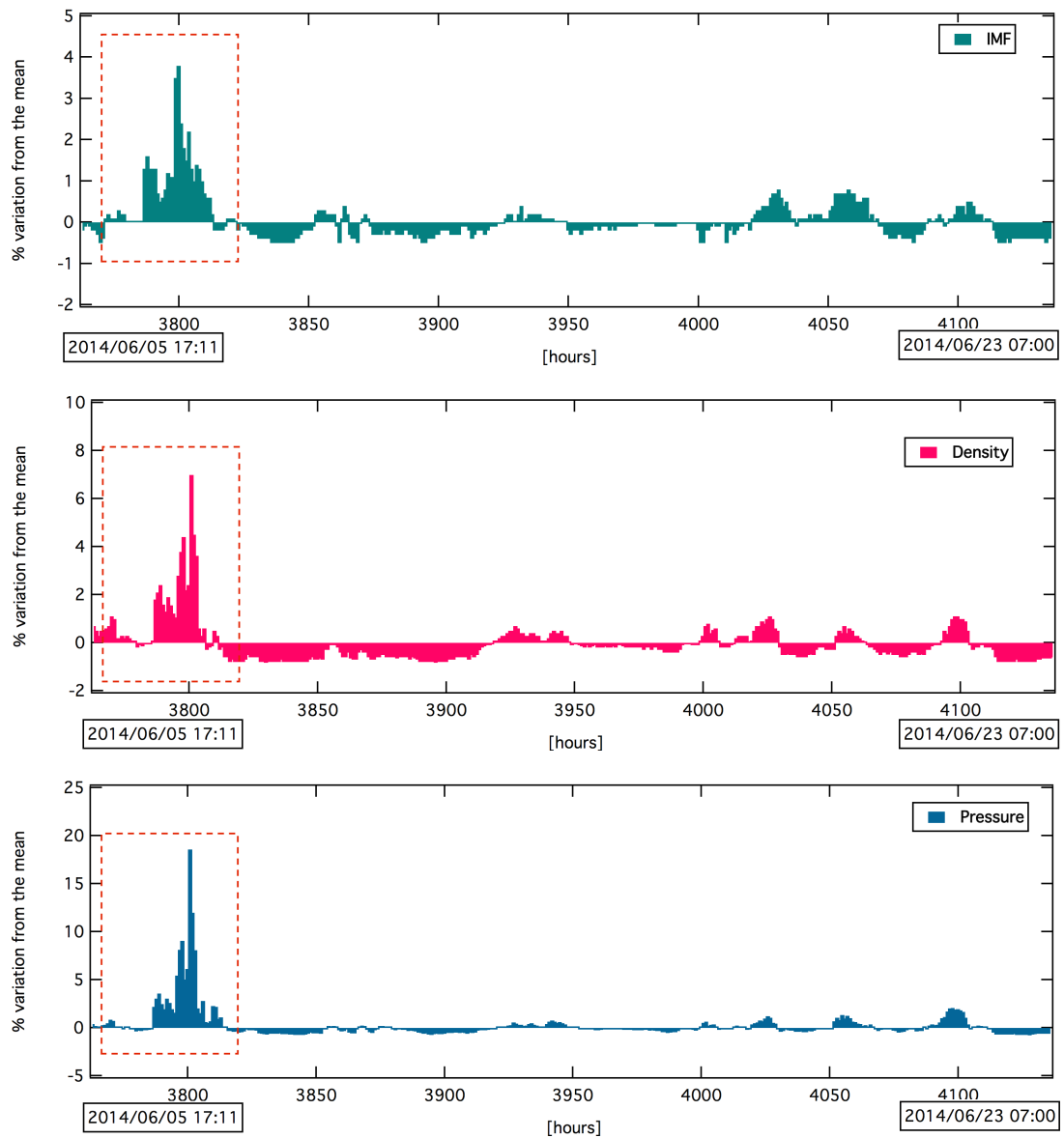


Figure 5.6: Solar activities observed in the June of 2014. The percentage variation from the mean pressure corrected rate of cosmic ray (green) was measured by prototype detector working at Sphinx Observatory terrace. The variation of the mean of solar parameters such as interplanetary magnetic field (teal), solar proton density (red), solar plasma flow speed (blue) and plasma flow pressure (ocean) were taken from OMNI solar weather station [56], the data taking period in terms of hours is corresponding between 3763 to 4136 from the beginning of the year.

While the higher solar activity hours around 3800 hours from the beginning of the year, there is trend of 2.0% decreasing the measured rate of the cosmic rays however the increasing the solar activity is shown in Figure 5.6 . A slowly

exponential recovery of cosmic flux, after its decreases, is another well known feature shown in the Figure 5.6. These decreasing trend is called a "*Forbush Decrease*". The Forbush decrease is a temporary decline in the galactic cosmic ray flux. Forbush decreases are generally represented by an unexpectedly start and arriving a minimum within about a day, followed by a more slow recovery stage generally lasting from several days up to a few weeks. The magnitudes of Forbush decreases fluctuate from a few percent up to 25% in the measurements which are typically originated by temporary interplanetary events that are akin to coronal mass ejections and shocks. Typical Forbush decrease is seen in Figure 5.7 [61].

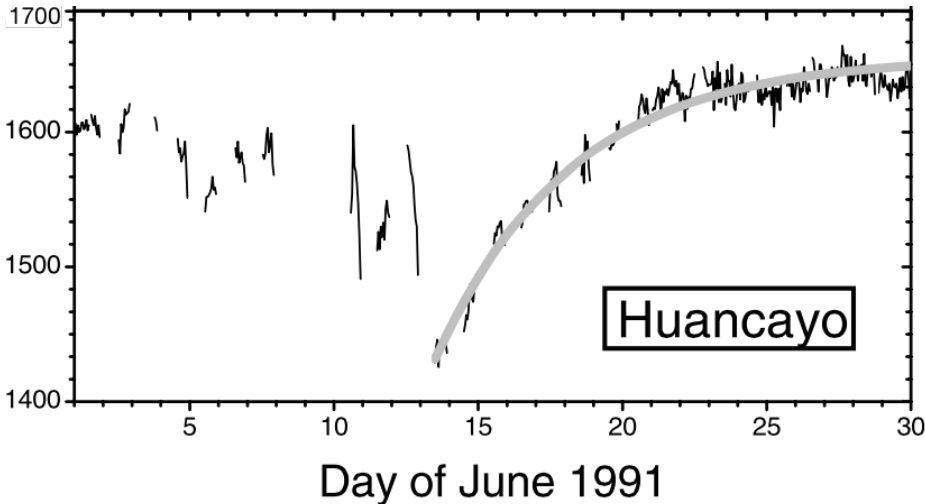


Figure 5.7: Typical Forbush decrease of the cosmic ray flux [61].

For the reason that the Forbush decrease events are well correlated with various interplanetary, solar parameters, the current cosmic ray flux measurement done in this study allow us to correlate our measurements in order to work out the temporal behavior of space weather.

CHAPTER 6

SUMMARY AND CONCLUSION

Currently, silicon photomultipliers represent as an attractive replacement to the traditional PMTs especially in high energy, astroparticle and space physics applications, where strict requirements in terms of magnetic insensitivity, power consumption, dimensions and costs have to be satisfied. The crucial necessity of the next generation high energy physics experiments will be efficient identification of the particles. For the next generation space experiments will involve large area calorimeters with quality of segmentation and large dynamic range. Moreover, for both fields, scintillator based detectors have been selected by various projects for their benefits in terms of cost per channel, mechanical durability and weight. Despite the fact that the light readout system is still a large area with various alternatives determined by the application, an area where silicon photomultipliers stands for a real advance. This thesis has dealt with the study of two types of silicon photomultipliers (with same dimension) and the development of a complete readout system for scintillating detectors. Both of the subjects have been satisfied by means of an application used as characterization for the study of the SiPMs and the readout systems. Extensive characterizations studies of SiPMs were presented in this thesis. The purpose of the studies was to investigate potential advantages and difficulties of using SiPMs as light detectors in fluorescence telescope used in the application described in chapter 4. The first investigated problem was the dependence of the breakdown voltage, and accordingly the overvoltage on the temperature. A linear dependence of the breakdown voltage on the temperature was observed with a constant of proportionality of $36 \text{ mV}/^\circ\text{C}$. As a stable overvoltage is essential for many applications, a method is required to keep the overvoltage stable. In order to perform this

goal, it is necessary to monitor the temperature and regulate the bias voltage accordingly. An automatic implementation of this method has been tested and found to keep the overvoltage stable over a wide temperature range. This was done by the Arduino micro-controller uses the SPI library. Another difficulty of using SiPMs is their correlated noise in the form of optical crosstalk and afterpulsing. Optical crosstalk produces the simultaneous firing of other pixel(s) for the firing of an initial pixel while afterpulsing causes delayed firing. At the upper end of the usually overvoltage range the probability of a crosstalk or afterpulse event to appear is in the range of 15% - 30% and 20% - 33%, respectively. In the most of crosstalk events only one additional pixel is fired. The crosstalk and afterpulsing probabilities were measured over a fixed overvoltage and were found to be stable and to only depend on the specific overvoltage. The dark noise rate and afterpulsing probability were found around 6 MHz and 1%, respectively.

As a consequence of the studies done in chapter 3, the application made on both the components of the Cherenkov light detection camera module (includes 1 SiPM for now) allowed us to widen our knowledge of the different features of such a device. It is shown that the application was engaged on a good trail and that the decision of plan to measure Cherenkov light were justified till now. The components of the camera module are working well and there are no unexpected results seen about their behavior. The angular acceptance of the setup for the detection of Cherenkov photons were also estimated about 22.7 photons assuming the quantum efficiency of the SiPM is 100%. The provided module was able to detect photons released by Cherenkov lights and that the DRS4 was a modified readout device for the camera module, the registered Cherenkov signal is seen in Figure 3.8. The next step of the characterization would be to get more measurements with the DRS4 for running some statistical analysis and validate the results. This would also result in the calibration of the camera module, which is a crucial stage of the development phase. A further concern is to improve the

gain of the test board on which the module is connected, in order to be able to detect single photoelectrons with the DRS4. An additional board is actually in production to achieve this aim. Finally, it would be a good validation of the camera module if we managed to detect an actual Cherenkov cone ring (or at least a part of it) with the module. However, more than one SiPM will be mounted on a board like as a matrix with 4×4 of one SiPM module for this measurement. The expected number of photons was estimated for this camera system is about 91.67 *photons* assuming the same setup and operating conditions will be used when we will replace only the camera module.

The study shows us that the detector prototype, described in chapter 4, was working at the harsh environmental conditions so that the detector components, like photomultiplier, inside the box, was protected by its environment to operate continuously as well as reliably by installing the Jackodur thermal insulator and it is protecting the system for the 10 °C temperature fluctuations (seen in section 4.5). The new DAQ system described in section 4.6 is working automatically. Moreover the new analysis program was written and the new time of flight technique was developed and tested for further analysis. The rise time of the SiPM signals was accumulated and found to be around 6.27 ± 0.16 and 4.979 ± 0.165 *ns* for each tile. The prototype detector station is also capable of discriminating the particles going upward and downward (seen in Figure 4.20). The ϕ dependence of the rate was also studied, and the excess of counts was seen (in Figure 4.30) when the station rotated about 56° from the initial setup where the station was pointing the valley and the shower was developed in 14.6 *km* depth. The results show us that the prototype detector has been working stably without any problem at these hard weather conditions.

As as results of the studies in chapter 5, the rate of cosmic ray measurements depict the regulation effects from both atmospheric and space weather parameters. The linear regression model was used for the data set well, in the sense that

the fits to the data capture the behavior over the period of overall cosmic ray fluctuations, with good reliability. At the beginning of the analysis the atmospheric effect was taken out for understanding the solar variation effect. Cosmic rays rate measurements showed an anti-correlation with atmospheric pressure and the barometric coefficient was obtained to be $(-0.11 \pm 0.01) \text{ \%}/\text{mb}$. This barometric coefficient was used to correct the detector data for pressure. Pressure corrected cosmic data shows a variation within. This count variation occurs due to the fluctuation of primary particle interaction altitude as a result of temperature changes. The temperature coefficient γ for the detector data was found to be 0.42. Pressure corrected muon data also show the effect of solar variation due to coronal mass ejections. The results, consistent with the literature, are most sensitive to variations in atmospheric pressure, P. There was a significant correlation found with temperature. For the future work on this subject, it is recommended to register the data continuously and expect some solar activity in these period in order to further analyze and correlate the solar effects with the detector performance.

REFERENCES

- [1] Gerhard Lutz et al. *Semiconductor radiation detectors*, volume 10. Springer, 1999.
- [2] Simon M Sze and Kwok K Ng. *Physics of semiconductor devices*. John Wiley & Sons, 2006.
- [3] Foteini Oikonomou. The pierre auger observatory: Overview and recent results. *Bulletin of the American Physical Society*, 59, 2014.
- [4] M Actis, G Agnetta, F Aharonian, A Akhperjanian, J Aleksić, E Aliu, D Allan, I Allekotte, F Antico, LA Antonelli, et al. Design concepts for the cherenkov telescope array cta: an advanced facility for ground-based high-energy gamma-ray astronomy. *Experimental Astronomy*, 32(3):193–316, 2011.
- [5] Claus Grupen, Armin Böhrer, and Luděk Smolík. *Particle detectors*, volume 199. Cambridge University Press Cambridge, 1996.
- [6] Roland H Haitz. Model for the electrical behavior of a microplasma. *Journal of Applied Physics*, 35(5):1370–1376, 1964.
- [7] RJ McIntyre. Theory of microplasma instability in silicon. *Journal of Applied Physics*, 32(6):983–995, 1961.
- [8] D Renker and E Lorenz. Advances in solid state photon detectors. *Journal of Instrumentation*, 4(04):P04004, 2009.
- [9] V Saveliev and V Golovin. Silicon avalanche photodiodes on the base of metal-resistor-semiconductor (mrs) structures. *Nuclear Instruments and Methods in Physics Research Section A: Accelerators, Spectrometers, Detectors and Associated Equipment*, 442(1):223–229, 2000.

- [10] D Bisello, A Paccagnella, D Pantano, Yu Gotra, N Malakhov, V Jejer, V Kushpil, and Z Sadygov. Metal-resistive layer-silicon (mrs) avalanche detectors with negative feedback. *Nuclear Instruments and Methods in Physics Research Section A: Accelerators, Spectrometers, Detectors and Associated Equipment*, 360(1):83–86, 1995.
- [11] P Buzhan, B Dolgoshein, A Ilyin, V Kantserov, V Kaplin, A Karakash, A Pleshko, E Popova, S Smirnov, Yu Volkov, et al. An advanced study of silicon photomultiplier. *ICFA Inst. Bull*, 21:28, 2001.
- [12] D Renker. Geiger-mode avalanche photodiodes, history, properties and problems. *Nuclear Instruments and Methods in Physics Research Section A: Accelerators, Spectrometers, Detectors and Associated Equipment*, 567(1):48–56, 2006.
- [13] Alessandro Berra. *Silicon Photomultipliers in High Energy and Space Applications*. PhD thesis, Insubria U., Como, 2012.
- [14] Y Du and F Retiere. After-pulsing and cross-talk in multi-pixel photon counters. *Nuclear Instruments and Methods in Physics Research Section A: Accelerators, Spectrometers, Detectors and Associated Equipment*, 596(3):396–401, 2008.
- [15] Fbk company. <https://srs.fbk.eu>.
- [16] Sensl company. <http://sensl.com>.
- [17] Minicircuits. <http://www.minicircuits.com>.
- [18] CR Crowell and SM Sze. Temperature dependence of avalanche multiplication in semiconductors. *Applied Physics Letters*, 9(6):242–244, 1966.

- [19] M. Petasecca, B. Alpat, G. Ambrosi, P. Azzarello, R. Battiston, M. Ionica, A. Papi, G.U. Pignatell, and S. Haino. Thermal and electrical characterization of silicon photomultiplier. *Nuclear Science, IEEE Transactions on*, 55(3):1686–1690, 2008.
- [20] Wavemetrics. <http://www.wavemetrics.com>.
- [21] Cherenkov telescope array (cta). <https://www.cta-observatory.org>.
- [22] Cosmic rays. <http://www.mpi-hd.mpg.de/hfm/CosmicRay/Showers.html>.
- [23] Carmen Baixeras. The magic telescope. *Nuclear Physics B-Proceedings Supplements*, 114:247–252, 2003.
- [24] JA Hinton. The status of the hess project. *New Astronomy Reviews*, 48(5):331–337, 2004.
- [25] Heinrich J Völk and Konrad Bernlöhr. Imaging very high energy gamma-ray telescopes. *Experimental Astronomy*, 25(1-3):173–191, 2009.
- [26] S Agostinelli, John Allison, K al Amako, J Apostolakis, H Araujo, P Arce, M Asai, D Axen, S Banerjee, G Barrand, et al. Geant4—a simulation toolkit. *Nuclear instruments and methods in physics research section A: Accelerators, Spectrometers, Detectors and Associated Equipment*, 506(3):250–303, 2003.
- [27] B Dolgoshein, V Balagura, P Buzhan, M Danilov, L Filatov, E Garutti, M Groll, A Ilyin, V Kantserov, V Kaplin, et al. Status report on silicon photomultiplier development and its applications. *Nuclear Instruments and Methods in Physics Research Section A: Accelerators, Spectrometers, Detectors and Associated Equipment*, 563(2):368–376, 2006.
- [28] Ali Yılmaz. Study of prototype detector for uhe $\nu\tau$ detection. Master’s thesis, Abant İzzet Baysal University, 2011.

- [29] D Fargion. Air-shower spectroscopy at horizons. *Progress in Particle and Nuclear Physics*, 57(1):384–393, 2006.
- [30] Stefan Ritt, Roberto Dinapoli, and Ueli Hartmann. Application of the drs chip for fast waveform digitizing. *Nuclear Instruments and Methods in Physics Research Section A: Accelerators, Spectrometers, Detectors and Associated Equipment*, 623(1):486–488, 2010.
- [31] Glenn F Knoll. *Radiation detection and measurement*. John Wiley & Sons, 2010.
- [32] William R Leo. *Techniques for nuclear and particle physics experiments: a how-to approach*. Springer, 1994.
- [33] Kuraray company. <http://www.kuraray.co.jp/en>.
- [34] H Dijkstra, R Horisberger, BD Hyams, G Maehlum, A Peisert, P Weilhammer, A Zalewska, W Krupinski, H Palka, M Turala, et al. Physics aspects of the delphi vertex detector. *Nuclear Instruments and Methods in Physics Research Section A: Accelerators, Spectrometers, Detectors and Associated Equipment*, 277(1):160–169, 1989.
- [35] Massimiliano Bitossi. Ultra-fast sampling and readout for the magic-ii telescope data acquisition system. URL <http://www.magic.mppmu.mpg.de/publications/theses/index.html>, 2009.
- [36] M Iori, IO Atakisi, G Chiodi, H Denizli, F Ferrarotto, M Kaya, A Yilmaz, L Recchia, and J Russ. Sipm application for a detector for uhe neutrinos tested at sphinx station. *Nuclear Instruments and Methods in Physics Research Section A: Accelerators, Spectrometers, Detectors and Associated Equipment*, 742:265–268, 2014.

- [37] Rene Brun and Fons Rademakers. Root—an object oriented data analysis framework. *Nuclear Instruments and Methods in Physics Research Section A: Accelerators, Spectrometers, Detectors and Associated Equipment*, 389(1):81–86, 1997.
- [38] Wolfram company. <http://mathworld.wolfram.com/LeastSquaresFitting.html>.
- [39] M. Iori, E. Arslan, H. Denizli, F. Ferrarotto, M. Kaya, A. Yilmaz, and J. Russ. Tests for a new concept of EAS detector for UHE neutrinos. *Journal of Physics Conference Series*, 409(1):012131, 2013.
- [40] John W Bieber, E Eroshenko, P Evenson, EO Flückiger, and R Kallenbach. *Cosmic rays and earth*, volume 10. Springer, 2000.
- [41] K Labitzke and H Van Loon. Some recent studies of probable connections between solar and atmospheric variability. In *Annales Geophysicae*, volume 11, pages 1084–1094, 1993.
- [42] Henrik Svensmark. Influence of cosmic rays on earth’s climate. *Physical Review Letters*, 81(22):5027, 1998.
- [43] Nigel D Marsh and Henrik Svensmark. Low cloud properties influenced by cosmic rays. *Physical Review Letters*, 85(23):5004, 2000.
- [44] Hilary V Cane. Coronal mass ejections and forrush decreases. *Space Science Reviews*, 93(1-2):55–77, 2000.
- [45] KA Firoz, DV Phani Kumar, and K-S Cho. On the relationship of cosmic ray intensity with solar, interplanetary, and geophysical parameters. *Astrophysics and Space Science*, 325(2):185–193, 2010.
- [46] P Adamson, C Andreopoulos, KE Arms, R Armstrong, DJ Auty, DS Ayres, C Backhouse, J Barnett, G Barr, WL Barrett, et al. Observation of muon

- intensity variations by season with the minos far detector. *Physical Review D*, 81(1):012001, 2010.
- [47] A Chilingarian and T Karapetyan. Calculation of the barometric coefficients at the start of the 24th solar activity cycle for particle detectors of aragats space environmental center. *Advances in Space Research*, 47(7):1140–1146, 2011.
- [48] Nasa. <http://www.nasa.gov/content/goddard/the-heart-of-space-weather-observed-in-action>.
- [49] Peter KF Grieder. *Cosmic rays at Earth*. Gulf Professional Publishing, 2001.
- [50] J. Beringer et al. Review of Particle Physics (RPP). *Phys.Rev.*, D86:010001, 2012.
- [51] Paul H Barrett, Lowell M Bollinger, Giuseppe Cocconi, Yehuda Eisenberg, and Kenneth Greisen. Interpretation of cosmic-ray measurements far underground. *Reviews of Modern Physics*, 24(3):133, 1952.
- [52] G Cini Castagnoli and MA Doderò. Temperature effect of the muon component underground and pion attenuation length. *Il Nuovo Cimento B Series 10*, 51(2):525–534, 1967.
- [53] ES Cotton and HO Curtis. Effects of the atmosphere on the penetrating component of the cosmic radiation. *Physical Review*, 84(4):840, 1951.
- [54] Meteoswiss. <http://www.meteoswiss.admin.ch>.
- [55] Leëib Isaakovich Dorman. Cosmic rays. variations and space explorations. *Amsterdam: North-Holland, and New York: Elsevier.*, 1, 1974.
- [56] Omniweb. <ftp://omniweb.gsfc.nasa.gov>.

- [57] Robert F Penna and Alice C Quillen. Decay of interplanetary coronal mass ejections and forbush decrease recovery times. *Journal of Geophysical Research: Space Physics (1978–2012)*, 110(A9), 2005.
- [58] Greg Bernero, Jacob Olitsky, and Reinhard A Schumacher. Atmospheric dependence of the stopping cosmic ray muon rate at ground level. *Journal of Physics G: Nuclear and Particle Physics*, 40(6):065203, 2013.
- [59] Solar physics. <http://solarscience.msfc.nasa.gov>.
- [60] Space weather. <http://www.ips.gov.au/Educational/1/2/3>.
- [61] IG Usoskin, I Braun, OG Gladysheva, JR Hörandel, T Jämsén, GA Kovaltsov, and SA Starodubtsev. Forbush decreases of cosmic rays: Energy dependence of the recovery phase. *Journal of Geophysical Research: Space Physics (1978–2012)*, 113(A7), 2008.
- [62] Yuri I Stozhkov. The role of cosmic rays in the atmospheric processes. *Journal of Physics G: Nuclear and Particle Physics*, 29(5):913, 2003.
- [63] Daniele Fargion. Discovering ultra-high-energy neutrinos through horizontal and upward τ air showers: evidence in terrestrial gamma flashes. *The Astrophysical Journal*, 570(2):909, 2002.
- [64] M Iori, E Arslan, H Denizli, M Kaya, A Yilmaz, and J Russ. Electron–muon identification by atmospheric shower in a new concept of an eas detector. *Nuclear Instruments and Methods in Physics Research Section A: Accelerators, Spectrometers, Detectors and Associated Equipment*, 692:285–287, 2012.

APPENDIX A

CURRICULUM VITAE

Name : Ali Yılmaz
Permanent Address : Abant Izzet Baysal University, Bolu, Turkey
Degree and date to be conferred : M.Sc, 2011
Place Date of Birth : Hatay, 1985

<u>Collegiate institutions attended</u>	<u>Dates</u>	<u>Degree</u>
Physics, Abant Izzet Baysal University	2008	B.S
Physics, Abant Izzet Baysal University	2011	M.S
Physics, University of Rome "La Sapienza" (ERASMUS)	2009 - 2010	M.S
Physics, Abant Izzet Baysal University	2015 - Present	Ph.D

<u>Professional Positions</u>	<u>Dates</u>
Research Assistant at Abant Izzet Baysal University	2009 - Present
Guest Researcher at INFN University of Rome "La Sapienza"	2009 - 2010
Guest Researcher at INFN University of Rome "La Sapienza"	2013 - 2015

<u>Awards and Grants</u>	<u>Dates</u>
Turkish Research Council Grant (TUBITAK-BIDEB) - 2214	2013 - 2014
Certificate of Achievement; Computer Applications Computer Applications at Accelerator and Particle Physics: Adana - TURKEY (TAEK)	2009

Collaborations:

- *TAU shoWER (TAUWER)* :
in ROMA, IT and Pittsburgh, USA
Full Member between May 2008 - ...
lead by Prof. Dr. Maurizio Iori (Univ. of ROMA "La Sapienza" -
IT) and Prof. Dr. James Russ (Carnegie Mellon Univ. - USA).

- *Cherenkov Telescope Array (CTA)* :
in INFN Sezione di Roma "La Sapienza", ROMA, IT
Researcher between November 2013 - November 2014.
lead by Prof. Dr. Maurizio Iori (Univ. of ROMA "La Sapienza" - IT).
- *Beam Diagnostics and Dynamics* :
in CLIC/CTF3-CERN
Researcher between January 2009 - ...
lead by Prof. Ömer Yavaş (Ankara Univ.)

Research Projects:

- BAP: 2009.03.02.324 Measurement of cosmic ray flux in 900m altitude 30000 TL 08.07.2009 - 08.07.2011.
- TAEK: Beam dynamics, beam diagnostics and control techniques and applications 300000 TL 2009 - 2012.
- TUBITAK:114F138: Building Look-up table to evaluate Tau-neutrino Energy from its shower observables and reconstructing the spherical wave-front of the shower development from timing information 15.11.2014 - 15.04.2017

Publications:

1. M. Iori, J. Russ, H. Denizli, F. Ferrarotto, M. Kaya and **A. Yilmaz**, "Test Results of a New Concept of an EAS Detector for UHE Neutrinos", ICRU2009, **OG 2.7** (2010) 08866.
2. **A. Yilmaz**, H. Denizli and M. Iori, "Preliminary Test Results of a Prototype at Sphinx Observatory Center", Balkan Physics Letters, **19** (2011) 191050 438-444.

3. M. Iori, E. Arslan, H. Denizli, M. Kaya, **A. Yilmaz** and J. Russ, "Electron-Muon Identification by Atmospheric Shower in a New Concept of an EAS Detector", NIM A, **692** (2012) 285-287.
4. M. Iori, E. Arslan, H. Denizli, F. Ferrarotto, M. Kaya, **A. Yilmaz** and J. Russ, "Tests for a new concept of EAS detector for UHE neutrinos", J. Phys.: Conf. Ser., **409** (2013) 01213.
5. M. Iori, I.O. Atakisi, G. Chiodi, H. Denizli, F. Ferrarotto, M. Kaya, **A. Yilmaz**, L. Recchia and J. Russ, "SiPM application for a detector for UHE neutrinos tested at Sphinx Station", NIM A **742** (2014) 265-268.
6. M. Iori, H. Denizli, **A. Yilmaz**, F. Ferrarotto and J. Russ, "Electron-muon identification by atmospheric shower and electron beam in a new concept of an EAS detector", Astrophysical Journal, (2015, Accepted).